Bifunctional single atom electrocatalysts: coordination–performance correlations and reaction pathways

Wan, Wenchao ; Triana, Carlos A ; Lan, Jinggang ; Li, Jingguo ; Allen, Christopher S ; Zhao, Yonggui ; Iannuzzi, Marcella ; Patzke, Greta R

Abstract: Single atom catalysts (SACs) are ideal model systems in catalysis research. Here we employ SACs to address the fundamental catalytic challenge of generating well-defined active metal centers to elucidate their interactions with coordinating atoms, which define their catalytic performance. We introduce a soft-landing molecular strategy for tailored SACs based on metal phthalocyanines (MPcs, M = Ni, Co, Fe) on graphene oxide (GO) layers to generate well-defined model targets for mechanistic studies. The formation of electronic channels through - conjugation with the graphene sheets enhances the MPc-GO performance in both oxygen evolution and reduction reactions (OER and ORR). Density functional theory (DFT) calculations unravel that the outstanding ORR activity of FePc-GO among the series is due to the high affinity of Fe atoms toward O2 species. Operando X-ray absorption spectroscopy and DFT studies demonstrate that the OER performance of the catalysts relates to thermodynamic or kinetic control at low- or high-potential ranges, respectively. We furthermore provide evidence that the participation of ligating N and C atoms around the metal centers provides a wider selection of active OER sites for both NiPc-GO and CoPc-GO. Our strategy promotes the understanding of coordination-activity relationships of high-performance SACs and their optimization for different processes through tailored combinations of metal centers and suitable ligand environments.

DOI: https://doi.org/10.1021/acsnano.0c05088

Bifunctional Single Atom Electrocatalysts: Coordination-Performance Correlations and Reaction Pathways

Wenchao Wan,[1] Carlos. A. Triana,[1] Jinggang Lan,[1] Jingguo Li,[1] Christopher S. Allen,[2] Yonggui Zhao,[1] Marcella Iannuzzi,[1] and Greta R. Patzke*[1]

[1] University of Zurich, Department of Chemistry, Winterthurerstrasse 190, CH-8057 Zürich, Switzerland.

[2] Electron Physical Science Imaging Center, Diamond Light Source Ltd, Didcot, Oxfordshire, UK. Department of Materials, University of Oxford, Oxford, UK.

Email: greta.patzke@chem.uzh.ch

ABSTRACT: Single atom catalysts (SACs) are excellent model systems in catalysis research, and we here employ them to address the fundamental catalytic challenges of generating well-defined active metal centers and elucidating their interactions with coordinating atoms define the performance. We introduce a soft-landing molecular strategy for tailored SACs based on metal phthalocyanines (MPc, M = Ni, Co, Fe) on graphene oxide (GO) layers to generate well-defined model targets for mechanistic studies. The formation of electronic channels through π-π conjugation with the graphene sheets enhances the MPc-GO performance in both oxygen evolution and reduction reactions (OER and ORR). Density-functional theory (DFT) calculations unravel that the outstanding ORR activity of FePc-GO among the series is due to the high affinity of Fe atoms towards O_2 species. Operando X-ray absorption spectroscopy (XAS) and DFT studies demonstrate that the OER performance of the catalysts relates to thermodynamic or kinetic control at low or high potential ranges, respectively. We furthermore provide evidence that the participation of ligating N and C atoms around the metal centers provides a wider selection of active OER sites for both NiPc-GO and CoPc-GO. Our strategy promotes the understanding of coordination-activity relationships of high performance SACs and their optimization for different processes through tailored combinations of metal centers and suitable ligand environments.

KEYWORDS: single atom catalyst, graphene, phthalocyanine, water oxidation, oxygen reduction, operando XAS

The green electrification of our industrial production and societies has raised an urgent need for the informed design of low-cost electrocatalysts. Both the electrocatalytic oxygen reduction reaction (ORR) and the oxygen evolution reaction (OER) are promising strategies for sustainable energy conversion and storage.[1,2] However, due to the involved proton-coupled four electron transfer reaction process involving two oxygen centers, these electrode reactions exhibit sluggish kinetics and higher energy demands compared to hydrogen electrode reactions.[1,3,4] Although great efforts have been made to improve their catalytic efficiency with manifold strategies,[5–9] the effective turnover frequencies (TOFs) of heterogeneous catalysts are still far behind those of homogeneous catalysts due to the majority of active sites that remain inaccessible inside their bulk phases. On top of this, identifying and understanding the relative influence of active centers and ligating atoms on the activity of heterogeneous catalysts is drastically restricted by the complex analytical setups that are required for monitoring their detailed structural changes under operational conditions.

In order to obtain the urgently required insight into reaction mechanisms at the atomic level, catalysts have thus been continuously downsized from nanoparticles[10] over clusters and molecules,[11] and most recently to single atom catalysts (SACs).[12–17] SACs with fully exposed active sites can permit a most direct exploration of structure-activity relationships on the atomic level,[18] but they still pose several issues. In the following, we address major mechanistic and design challenges of both current SAC and general heterogeneous catalysis research, such as: How exactly do the coordinating atoms influence the resulting activity? Whereas coordination-activity relationships are a strong focus of molecular catalysis, they are surprisingly far less explored for SACs. To the best of our knowledge, no experimental mechanistic studies have been conducted for the OER with SACs.

Regarding preparative progress, the dispersion of single atoms on N-doped carbon supports has been widely researched[19–23] due to their high specific surface area and electronegativity, which provide abundant anchoring sites for stabilizing single atoms.[23,24] However, the synthesis of N-doped carbon-based SACs involves high-temperature pyrolysis of C-N based precursors or defective graphene oxide (GO) under inert gas or NH_3 atmosphere for the stabilization and separation of metal atoms. Therefore, aggregation of the catalytic centers is still hard to prevent.[25] Even though subsequent acid pickling is usually employed to remove clusters or nanoparticle side products, the resulting catalysts then suffer from low metal contents, and the further influence of these acid treatments remains unclear.[26] As tailoring of the coordination environment in such SACs remains challenging due to the diverse valences of metal centers, defective substrates and limited control options over the pyrolysis process, we present a facile and clean strategy here to generate well-defined model SACs for mechanistic studies.

Concerning the coordination environment of the metal centers in SACs and the electronegativity of the neighboring species, recent works have demonstrated that both play a crucial role in the catalytic activity.[27–30] Huang *et al.*[31] suggested that the C atoms next to N atoms in Ni-N_4-C_4 SACs also act as active sites, providing a dual reaction pathway for OER. Feng *et al.*[32] proved that the replacement of N by S atoms in the Ni-N_4-C moiety can significantly promote the water oxidation activity. More recently, the Ni-O-G SACs with oxygen coordination has notably improved the activity of Ni SAC for OER.[33] These studies revealed that synthetic design of SACs with well-defined coordination environments is of vital importance for enhanced catalytic activity for OER. Given that general investigations of this crucial issue are still in their start-up stage,[34] we here provide substantial evidence for the important participation of the coordinating atoms.

To this end, we introduce a molecular strategy for soft-landing well-coordinated heterogeneous SACs (in the following referred to as HSACs) based on metal-phthalocyanine (MPc, M=Ni, Co, Fe) molecular catalysts. We here conjugate the reportedly most promising base metal centers[35] to graphene oxide (GO) layers to generate highly defined catalysts for our innovative mechanistic investigations. While similar systems consisting of MPc and carbon materials were applied for catalysis,[36,37] their reported OER performances leave room for further improvement.[38] The molecular based SACs here provide us with accurate coordination models for exploring structure/coordination-performance relationships, which have rarely been investigated in SACs. DFT calculations on these tailored model systems combined with experimental XPS and XAS studies substantiate chemical interaction between the two components, which provides channels for electron transfer, leading to improvement of the electrochemical performance. The electrochemical OER and ORR activities of NiPc-GO and FePc-GO are higher than those of commercial RuO_2 and Pt/C reference catalysts, and most of the recent SACs (cf. **Tables S9-10**). XAS and high-angle annular dark-field scanning TEM (ADF-STEM) results demonstrate that the metal centers in the hybrid MPc-GO catalysts are uniformly coordinated by the N_4-C_8 plane of the MPc molecules. The operando XAS studies combined with DFT calculations demonstrate the presence of opposite OER/ORR activity trends, which are strongly linked to the coordinating atoms around the metal centers. Therefore, we propose a ligating atom-assisted OER mechanism, which provides an explanation as to why the most current single site SACs are more suitable for ORR than for OER.

Our combination of operando XAS spectroscopy and DFT analyses with electrochemical measurements provides comprehensive evidence of distinctive, ligand-dependent OER *vs.* ORR pathways in HSACs. In the following, we also demonstrate how the respective coordinating atoms display different behavior towards the OER reaction intermediates.

RESULTS AND DISCUSSION

NiPc, CoPc, and FePc molecules were selected as the precursors in our study since they form very well-defined coordination environments with C/N atoms and are widely used as reference compounds to identify SACs. We first calculated the charge distributions of NiPc, CoPc and FePc coupled with graphene (**Figs. 1a, b, c**). The isosurface plots clearly show charge redistribution between graphene and

MPc molecules due to π-π stacking. Charge difference analyses further demonstrate the charge transfers between graphene and MPc molecules (**Figs. 1d**). Especially, the charge transfer in FePc-Graphene is more intense as the density of electron clouds is higher compared to those of NiPc-and CoPc-Graphene. In general, graphene-like structures can modify polarized electron-rich and electron-depleted sites by adding or removing electrons, which results in delocalization of π electrons and further tuning of the electronic structure. In this configuration, both the graphene and MPc contain π electrons and sp^2 hybridized carbon, so that their interaction can physically increase the delocalization of π electrons on both surfaces, forming transition channels for electrons. Furthermore, electron redistribution, in turn, changes the local electron environment of the adjacent N, C and metal atoms on MPc, which is assumed to enhance their catalytic performance.[39]

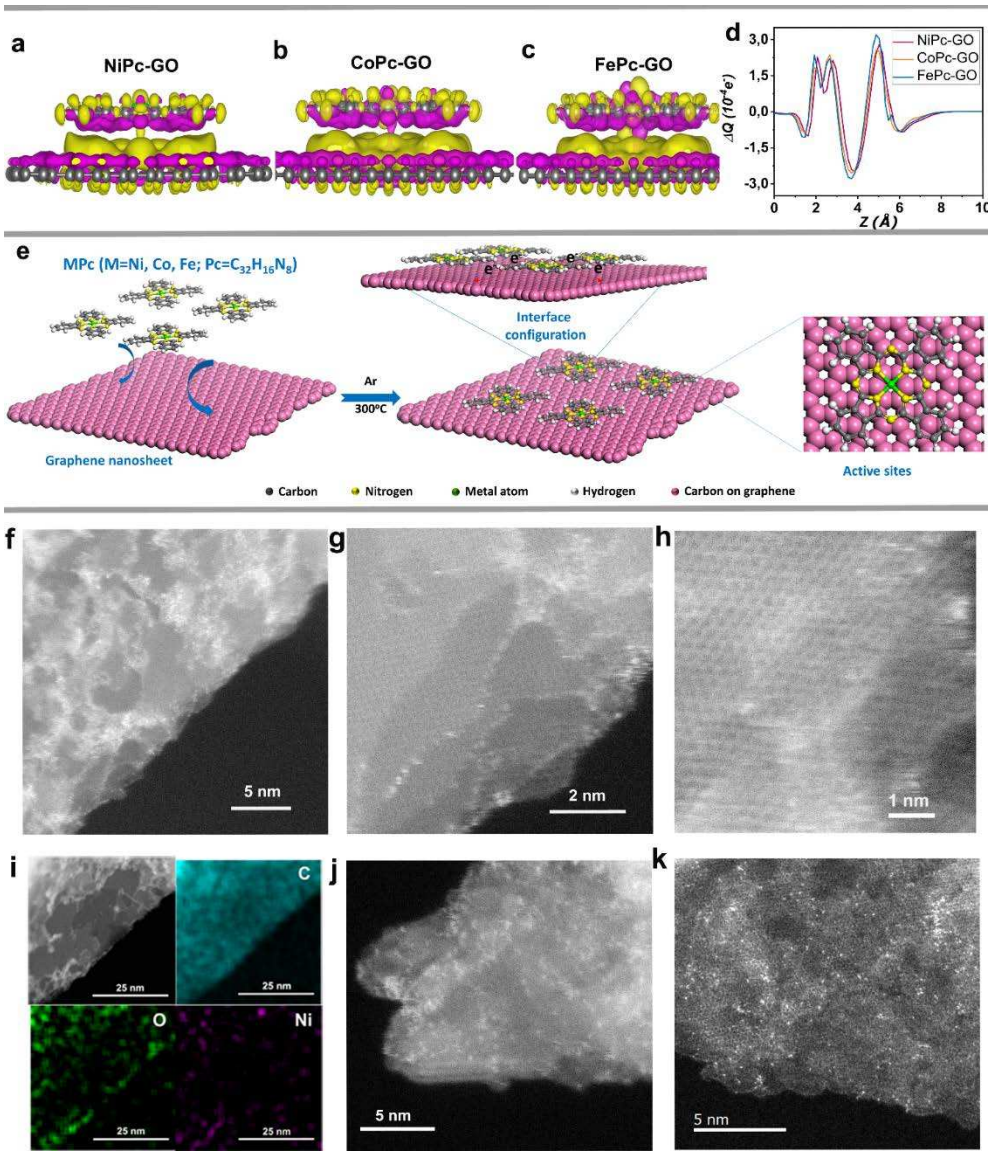

Figure 1. DFT simulations of the synergistic effect between MPcs (M=Ni, Co, Fe) and GO. Isosurface plots of charge redistribution for (a) NiPc-GO, (b) CoPc-GO and (c) FePc-GO and (d) integrated charge transfer curves; yellow or violet color represents the accumulation or depletion of electrons, respectively. (e) Schematic illustration of the synthetic route to HSACs. (f-h) ADF-STEM images of NiPc-GO at different magnifications. (i) EDX mapping of NiPc-GO. (j-k) ADF-STEM images of CoPc-GO and FePc-GO.

Based on the above configurations predicted by DFT, we designed a molecular strategy for soft-landing well-coordinated metal phthalocyanine molecules on graphene oxide layers (NiPc-GO, CoPc-GO, and FePc-GO) as shown in **Fig. 1e**. The strategy is different from previous synthesis methods that directly use inorganic metal ion precursors to be captured by the defects on carbon supports or to react with N ions into M-N bonds.[40,41] In this approach, metal centers are strongly coordinated by the C/N atoms to maintain a neat and controllable local environment and subsequently landing on the GO sheets. This is crucial because the catalytic activity of single site catalysts has been theoretically proven to be sensitive to the local coordination environment.[27] In addition, the strong coordination by the phthalocyanine ligands can also suppress the aggregation of metal atoms under pyrolysis conditions, thus providing a high content of single metal atoms. As determined from inductive coupled plasma mass spectrometry (ICP-MS, **Table S1**), the contents of metal atoms in our catalysts are as high as 1.65, 1.70 and 1.60 wt % for NiPc-GO, CoPc-GO and FePc-GO, respectively, which is higher than many current SACs.[12,13,42]

To directly identify the atomic dispersion of NiPc, CoPc and FePc on GO layers, ADF-STEM imaging was used for all samples. The uniform distribution of heavy metal atoms (bright spots) throughout the GO substrate is evident from the STEM images (**Fig. 1f**). Higher magnification furthermore provides atomic resolution of the metal atoms and structural information for the GO (**Figs. 1g-h**). The typical uniform honeycomb lattice of the graphene layers is evident from **Fig. 1h**, indicating a well-maintained structure and good conductivity. It is likely that the MPc molecules intertwine with each other contaminating the pristine graphitic surface and limiting the STEM resolution. Despite this, the relatively heavy Ni atoms can be identified as bright dots compared to the surrounding C atoms. Energy dispersive X-ray spectroscopy (EDX) confirms the composition of NiPc-GO samples containing heavy Ni elements (**Fig. 1i**). CoPc-GO and FePc-GO samples display a similar atomic dispersion on GO sheets as shown in **Figs. 1j-k**. The EDX measurements at lower magnifications (**Fig. S1**) and STEM images at different magnifications (**Fig. S2-S3**) furthermore show the uniform dispersion of the molecules on the GO sheets. Further comparison of HRTEM images (**Figs. S4-S8**) including NiPc-GO, CoPc-GO, FePc-GO, GO (pyrolysis at 300 °C) and pure NiPc also shows the dispersion of molecules on GO sheets. No reflections of metal nanoparticles were found in powder X-ray diffraction patterns (PXRD), and Raman spectra indicated that the pyrolysis process does not form any nanoparticles in the samples (**Figs. S9-10**). The similar Raman spectra and PXRD patterns of the MPcs before and after pyrolysis (300 °C) show that the local structure around the metal centers in MPcs is still well preserved (**Figs. S11-12**). The PXRD patterns (**Figs. S13-14**) of GO before and after 300 °C pyrolysis confirm that there is almost no damage on the GO lattice after pyrolysis, which is backed up by elemental analysis (**Table S2**) and HRTEM results (**Fig. S8**).

Chemical composition and states were further examined by X-ray photoelectron spectroscopy (XPS). The results reveal that the samples contain C, N and O as non-metallic elements, and Ni, Co and Fe as metallic components, respectively (**Fig. S15**). High-resolution spectra are shown in **Fig. S16**. Two main peaks in NiPc-GO assigned to Ni^{2+} are present at binding energies of around 855.8 and 873.2 eV with two negligible satellite peaks at 863.2 and 879.4 eV. In the CoPc-GO sample two peaks at 780.3 and 795.8 eV belong to Co^{2+} with two satellite peaks at 786.0 and 804.0 eV, and a slight Co^{3+} peak is also observed at 782.0 and 796.3 eV. The oxidation state for FePc-GO is quite different and almost all the signals arise from Fe^{3+}. The noise most likely arises from the low content of Fe atoms.[43,44] The high-resolution spectra of C1s and N1s for all three samples are very similar. In spectra of C1s, the main peaks at around 284.5 and 286.1 eV can be attributed to the phenyl rings and pyrrole carbon atoms, representing C-C and C-N bonds, respectively. The peaks in N1s at around 399.1 and 400.1 eV correspond to N-C and N-M bonds (M = Ni, Co, Fe). The comparison with pure NiPc, CoPc and FePc furthermore shows that the binding energies of all metal are slightly shifted to higher energies, especially in FePc-GO, which indicates the presence of chemical bonding between the molecules and GO (**Figs. S16a-f**). The presence of Co^{3+} and Fe^{3+} in the pure MPcs may be associated with the strong adsorption of O_2 (**Figure S53**), leading to oxidation. Similar results have been reported in a previous study.[45]

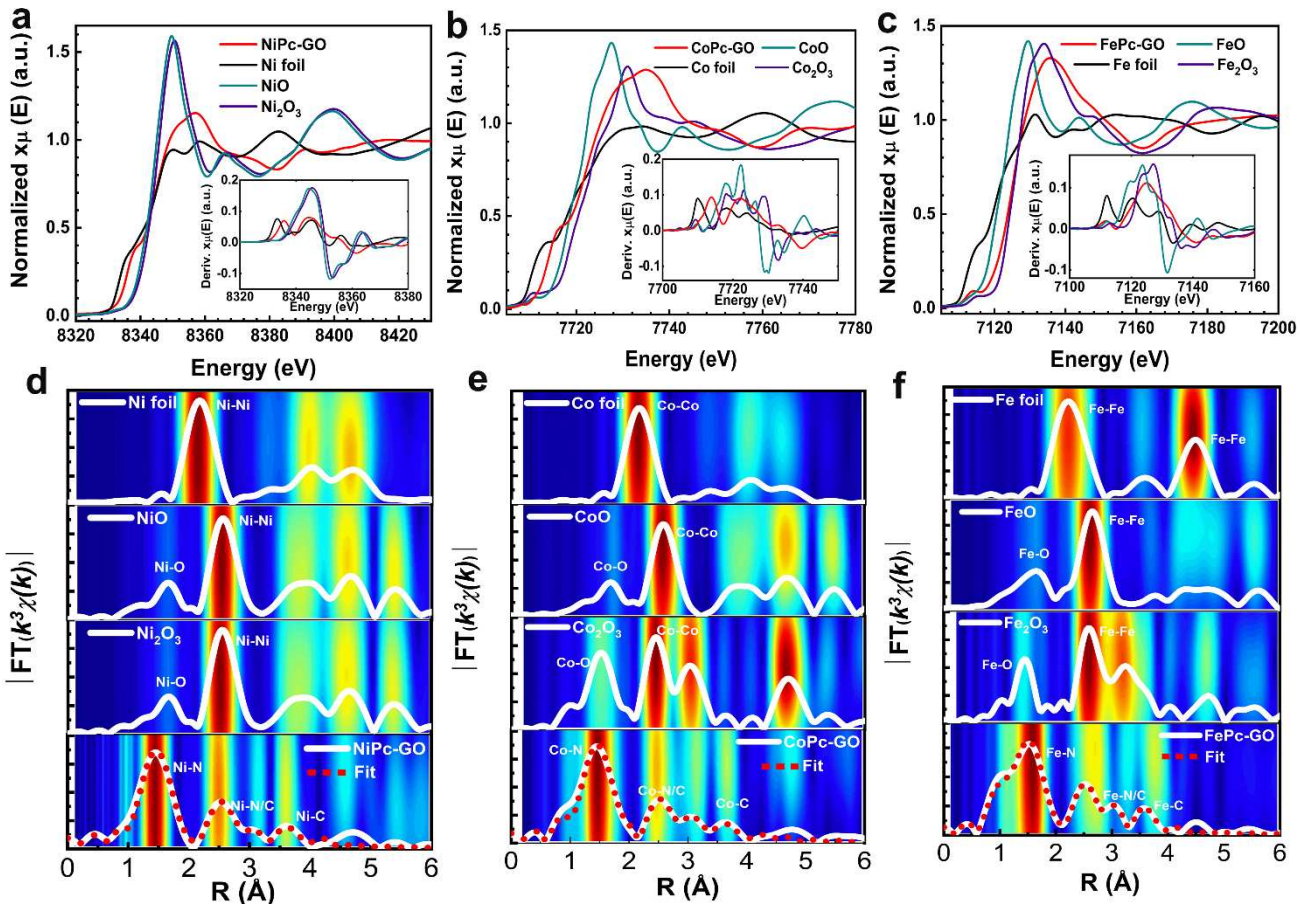

Figure 2. Structural characterization from XANES and EXAFS spectroscopy. (a-c) Ni, Co and Fe K-edge XANES spectra and their first derivative (insets) for NiPc-GO, CoPc-GO, FePc-GO and corresponding reference oxides. (d-f) Fourier-|FT(k³χ(k))| and Wavelet-Transform (WT, 2D contour plots) spectra of the EXAFS signal for NiPc-GO, CoPc-GO, FePc-GO and their reference oxides (phase uncorrected). The spectra at the bottom show the fittings (dashed) of the experimental |FT(k³χ(k))| spectra (red) of NiPc-GO, CoPc-GO and FePc-GO (phase uncorrected).

In earlier works on transition-metal-based catalysts the metal centers were established as the initial and unique active sites. However, with the advent of SACs it became clear that the local coordination environment of the metal centers also plays an important role in the performance.[46] To assess the electronic structure and local environment of the catalysts, the Ni, Co and Fe K-edge X-ray absorption near edge structure (XANES) spectra were investigated (**Figs. 2a-c**). The pre-edge peak in the XANES spectra of NiPc-GO (~8334 eV) and CoPc-GO (~7708 eV), arising from dipole-forbidden but metal Ni or Co hybridized orbital 1*s*→3*d*(metal)4*p*(ligand) quadrupole-allowed transitions are very low in intensity due to the high D_{4h} centrosymmetry of those samples (**Figs. 2a-b**). The 3d orbitals of Ni^{2+} and Co^{2+} are almost fully occupied. The intensity of the pre-edge peak due to 1*s*→4p_z transitions at ~8339 eV for NiPc-GO and ~7717 eV for CoPc-GO exhibits comparable intensity to that of NiPc and CoPc (**Figs. 3g,h**). In FePc-GO, due to the dominant Fe^{3+} states with empty 3d-orbitals, the pre-edge peak arising from 1*s*→3*d* transitions at ~7114 eV is more notable (**Figs. 2c, 3i**). While the Ni, Co and Fe K-edges exhibit a similar near edge structure to those of NiPc, CoPc and FePc, their absorption edges are slightly shifted to higher energy (**Figs. 3g-i**). This is due to the spontaneous charge transfer from delocalized unpaired electrons from the 3*d*-orbital of the active metal centers Fe, Co, and Ni to the N/C 2*p* orbitals of the GO layer as is evident from the DFT calculations above. Evaluation of the

XANES spectra in **Figs. 2a-c** shows that pristine NiPc-GO, CoPc-GO and FePc-GO unveil distinct local coordination and oxidation states when compared to those found in reference Ni/Co/Fe-oxides. Comparisons of the rising absorption edge and first derivative of the XANES spectra for pristine NiPc-GO, CoPc-GO, FePc-GO and reference Ni/Co/Fe-oxides are shown in the insets of **Figs. 2a-c**, and with higher magnifications in the insets of **Figs. 5a-c**. The XAS spectra of NiO and Ni_2O_3 oxide references are quite similar to each other, as has been previously reported.[47–50] While the rising absorption edge of NiPc-GO is located between those of reference NiO and Ni_2O_3 oxides, the former one is far closer to that of divalent NiO (**Figs. 2a, 5a**), which indicates the prevailing presence of Ni^{2+} oxidation states in NiPc-GO. Moreover, the XANES spectrum of NiPc-GO is similar to that of the Ni(II) phthalocyanine (NiPc) reference (**Fig. 3g**). This verifies further the prevailing Ni^{2+} oxidation states in NiPc-GO, which also agrees with earlier XAS studies on NiPc-based compounds.[51] For CoPc-GO, the spectrum is located between those of CoO and Co_2O_3 indicating a mixed Co^{2+}/Co^{3+} oxidation state. The rising absorption edge and the highest peak in the 1st-derivative of the XANES spectrum of FePc-GO overlap with those of Fe_2O_3, indicating the presence of Fe^{3+}. These valence states agree with previous reports,[46,52] and are also in agreement with the results from XPS (**Fig. S16**).

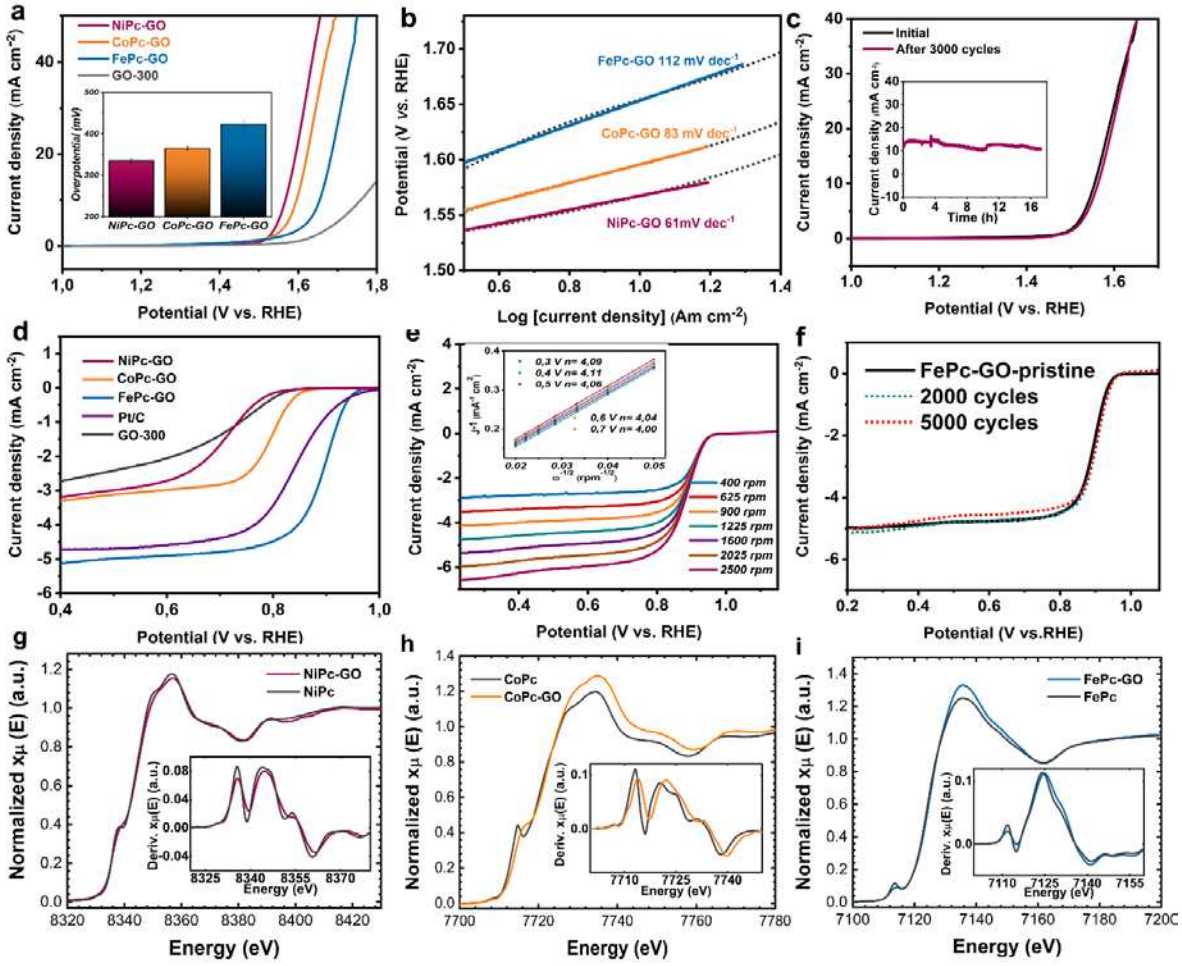

Figure 3. Electrochemical OER/ORR characterizations. (a) OER LSV curves of NiPc-GO, CoPc-GO and FePc-GO, with mean overpotentials from 5 measurements (inset), and the corresponding Tafel plots (b). (c) LSV curves before and after 3000 CV cycles and long-term chronoamperometric OER test (inset) of NiPc-GO. (d) ORR LSV curves in 0.1 M oxygen-saturated KOH solution at a scan rate of 5 mV s^{-1}. (e) LSV curves of FePc-GO with a scan rate of 5 mV s^{-1} at different rotation rates and the Koutecky–Levich (K–L) plots (inset). (f) LSV curves after 2000 and 5000 CVs in the potential range of 0.2–1.2 V *vs.* RHE in 0.1 M oxygen-saturated KOH solution at a scan rate of 5 mV s^{-1}. (g-i) Ni, Co and Fe K-edge XANES spectra and first derivatives (insets) of NiPc-GO, CoPc-GO and FePc-GO before and after coupling with graphene oxide (GO) layer.

The local structures of the metal centers in NiPc-GO, CoPc-GO, FePc-GO were further derived from the Fourier |FT($k^3\chi(k)$)| and wavelet-transform (WT) of the EXAFS spectra (**Figs. 2d-f**). While the |FT($k^3\chi(k)$)| and WT spectra of NiPc-GO, CoPc-GO and FePc-GO show similar local structural features, none of their peaks match with those of their reference Ni/Co/Fe oxides, indicating the totally different atomic local-coordination of the single metal centers. The main peak intensity in the real-space |FT($k^3\chi(k)$)| and WT spectra at ~1.5 Å relates to backscattering from neighboring N atoms in the first coordination shell with interatomic distances of 1.90 Å (NiPc-GO), 1.91 Å (CoPc-GO) and 1.92 Å (FePc-GO), and a main coordination number N (Ni/Co/Fe-N)=4. The peak at ~2.5 Å relates to backscattering from neighboring C (Ni/Co/Fe-C = 8) and N (Ni/Co/Fe-N = 4) atoms in the second coordination shell, with interatomic distances into the range of ~2.94-3.39 Å. Other relevant structural parameters, namely interatomic distances, atomic coordination numbers (N) and Debye-Waller factors (σ^2), as calculated from non-linear least-squares fitting of the |FT($k^3\chi(k)$)| spectra (bottom of **Figs. 2d-f**), are given in **Tables S4a-S4c**. The contributions of each fitted single scattering path to the total fitted EXAFS spectra |FT($k^3\chi(k)$)| are shown in **Figs. S46-S48**. As shown in **Figs. S46-S48** and **Tables S4a-S4c**, the 1st, 2nd, 3rd and 5th scattering paths Ni/Co/Fe-N, Ni/Co/Fe-C, Ni/Co/Fe-N and Ni/Co/Fe-C from the NiPc, CoPc and FePc molecules contribute more notably to the experimental |FT($k^3\chi(k)$)| spectra, with ranks of 100, 66.4, 27.3 and 28.6 %, respectively. The 4th scattering path Ni/Co/Fe-C, with a rank of 14.3%, corresponds to backscattering from the six C atoms from the GO layer at interatomic distances of ~3.7-3.8 Å, as shown in **Figs. S49-S50**. Although the intensity of this scattering path seems to be lower, its inclusion improves notably the fitting into the range ~2.97-3.56 Å of the |FT($k^3\chi(k)$)| spectra and significantly reduces the R-factors as shown in **Figs. S46-S48** and **Tables S4a-S4c**. Based on these results it is clear that all these five scattering paths can be well-fitted to the measured |FT($k^3\chi(k)$)| spectra, thereby corroborating that our optimized model structures from DFT calculations agree very well with the experimental EXAFS data. From these results, it is also clearly established that the square-planar Ni-N_4, Co-N_4, and Fe-N_4 moieties with D_{4h} symmetry, as well as the overall local structure and the coordination environment of the precursor molecules NiPc, CoPc and FePc are largely retained in pristine NiPc-GO, CoPc-GO and FePc-GO after conjugation with the GO layer as shown in **Figs. S17** and **S49-S51**.

For the OER performance, the linear sweep voltammetry (LSV) curves (**Fig. 3a**) show that NiPc-GO exhibits the best activity with an overpotential of 320 mV at the current density of 10 mA cm^{-2} without iR compensation. The overpotentials for CoPc-GO and FePc-GO are 370 mV and 420 mV at 10 mA cm^{-2}, respectively. The normalized activities to the mass of the catalysts are 300 mV, 330 mV and 370 mV at 10 A g^{-1}, respectively, as shown in **Fig. S18**. The activities with iR correction do not differ significantly from those without iR compensation (**Fig. S18**). The overpotential of NiPc-GO is 50 mV lower compared to a commercial RuO_2 reference at 10 mA cm^{-2} (**Fig. S19**) and superior to most of previous reported SACs (**Table S9**).[31,53] The GO-300 (pyrolysis under 300 °C) shows inferior OER activity with an overpotential of 530 mV at the current density of 10 mA cm^{-2}, probably due to the O atoms and defects as reported in previous studies.[54,55] The OER activities of bare Ni-Pc, Co-Pc and Fe-Pc molecules without GO were also tested as shown in **Figs. S20-22**. Almost no activities were observed for all the bare molecular compounds, suggesting that their synergistic effects with GO contribute to the observed enhanced performance. Other than the activity, an interesting phenomenon observed in the OER LSV curves is that the raise of current density for FePc-GO sets in much earlier than that of CoPc-GO and NiPc-GO, which does not correspond with the recorded overpotentials at 10 mA cm^{-2}. The reasons for this anomaly are discussed in detail below. The Tafel slope of NiPc-GO is 61 mV dec^{-1}, much lower than those of CoPc-GO (83 mV dec^{-1}) and FePc-GO (112 mV dec^{-1}, **Fig. 3b**), suggesting superior OER kinetics. NiPc-GO shows the lowest electrochemical impedance spectroscopy (EIS) values at 1.5 V *vs.* RHE compared to those of CoPc-GO and FePc-GO (**Fig. S23**), indicating a notably lower charge transfer resistance at this potential. This can be also

observed from the corresponding LSV curves. The stability of NiPc-GO was investigated by measuring its polarization curve after 3000 CV cycles, which showed only negligible changes (**Fig. 3c**). Chronoamperometry measurements on Ni foam further showed that the catalyst retains its catalytic activity for more than 17 h above 10 mA cm^{-2} (inset **Fig. 3c**). The bare Ni foam shows a very small current density of 3.5 mA/cm^2 in comparison under the same measurement conditions (**Fig. S24**).

The electronic structure of NiPc-GO, CoPc-GO and FePc-GO after OER was derived from XAS spectra. The respective Ni, Co, and Fe adsorption K-edges in the XANES spectra were slightly shifted to higher energy, which is ascribed to an increase in the oxidation state of the metal atoms after OER (**Figs. S25, S27, S29**). The overall features of the post-catalytic EXAFS spectra $|FT(k^3\chi(k))|$ of NiPc-GO, CoPc-GO and FePc-GO after OER (**Figs. S26, S28, S30**), were similar to those of the pristine samples. This suggests that the square-planar symmetry D_{4h} of the metal center in NiPc-GO, CoPc-GO and FePc-GO only underwent minor changes in the coordination structure after OER, due to a small disorder induced by adsorbed $OH^-/O_2/H_2O$ species perpendicular to the D_{4h} molecular plane. Furthermore, ICP-MS analysis after OER showed that no metal ions were leached into the electrolyte (see **Table S3**). These results in their entirety demonstrate that the phthalocyanine coordination environment on top of the GO layer indeed stabilized the metal centers.

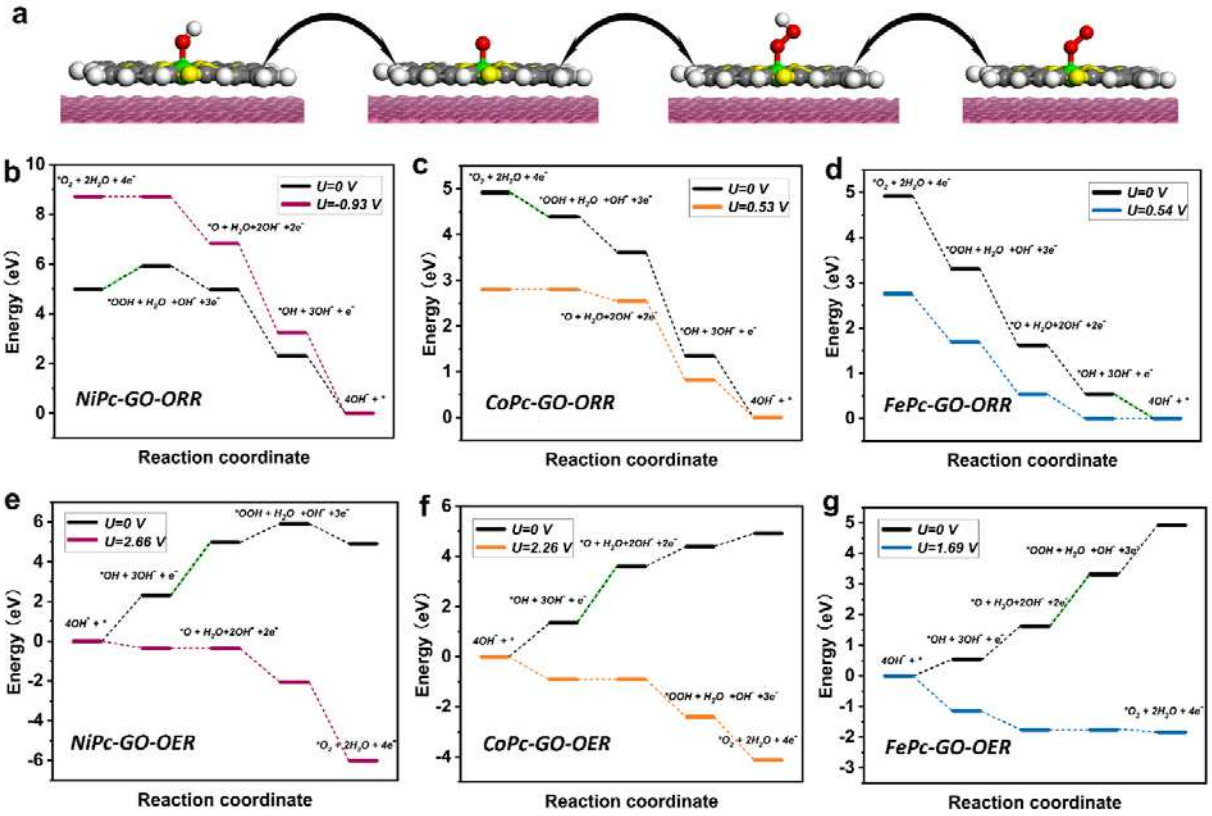

Figure 4. DFT calculation of ORR and OER. (a) Atomic configurations of the catalysts for OER/ORR with different adsorption states towards intermediates. Free energy diagram of (b-d) ORR and (e-g) OER for NiPc-GO, CoPc-GO and FePc-GO on metal centers: black lines represent the initial states and colored lines indicate the needed potentials for initiating the reactions.

The catalysts also exhibit outstanding ORR performances (**Figs. 3d-f**). The LSV curve of FePc-GO exhibits an extremely high half-wave potential of 0.89 V, which is 60 mV more positive compared to commercial Pt/C and other

reference materials (**Fig. 3d**) and better than most of ORR electrocatalysts based on non-precious-metal elements (**Table S10**). The limiting current density (≈5.33 mA cm^{-2}) outperforms that of Pt/C (≈4.63 mA cm^{-2}) (**Fig. 3d**). The enhanced performance of the MPcs after coupling with carbon materials was also reported in previous studies.[45,56] The ORR reaction mechanism was further investigated by applying the Koutecky–Levich (K-L) equation and the rotating ring disk electrode (RRDE) technique. The number of transferred electrons for FePc-GO is about 4.06 (Fig. 3e), which is quite close to the measured value of Pt/C (4.0**, Fig. S32**), revealing that the oxygen reduction proceeds *via* a near-four-electron pathway. The evolution of peroxide (HO_2^-) during the ORR process is strikingly suppressed to less than 2.4 % yield (**Fig. S31**), proving excellent selectivity of direct O_2 reduction to OH^-. The ORR kinetics of FePc-GO were evaluated by RRDE tests at different rotation speeds ranging from 400 to 2500 rpm (**Fig. 3e**). The diffusion saturated current density increases with respect to the rotation rate, because at higher speed the diffusion distance of oxygen saturated solution is shortened, which improves the mass transport notably. The Koutecky–Levich (K–L) plots obtained from RDE tests show good linear and parallel characteristics (inset **Fig. 3e**), demonstrating the first-order reaction kinetics with respect to the dissolved oxygen concentration in the solution and the similar number of electrons transferred during ORR at different potentials. The number of transferred electrons is about 4.06, which matches well with the RRDE results and the results of Pt/C (**Figs. S32-33**). The stability of FePc-GO was further examined by measuring the RDE polarization curves before and after 5000 CV cycles, and the result shows almost no increase of the half-wave afterwards (**Fig. 3f**). Further high-resolution TEM images (**Figs. S34-42**) and ICP-MS measurements show that no metal particles were generated and no metal ion leaching was detected after ORR catalysis (**Table S2**). The ORR performances of GO after 300 ^oC pyrolysis and MPcs were also examined (**Figs. S43-45**), and all of the samples show analogous trends as seen for OER, namely that the conjugation with graphene significantly improves the ORR performance.

This improvement in the performance for the OER and ORR after conjugation with the graphene nanosheets can be ascribed to the interaction between the MPc molecules and the GO layers as unraveled from the DFT calculations in **Figs. 1a-d**. To further confirm this favorable effect, XANES spectra were recorded for the three MPc precursor molecules before and after conjugation with GO (**Figs. 3g-i**). The edge absorption energies of NiPc-GO, CoPc-GO and FePc-GO are slightly shifted to higher energy, especially on the rising-edge, which corresponds to the second peak in the 1st-derivative of the XANES spectra (insets **Figs. 3g-i**). These energy shifts of the rising absorption K-edge imply some hybridized charge transfer between delocalized unpaired electrons from the 3*d*-orbital of the metal centers Fe, Co, Ni and the C 2*p* orbitals of the GO layer, which confirms the creation of electronic channels at the interface.[57,58] Results from the non-linear least-square fitting of the EXAFS spectra $|FT(k^3\chi(k))|$ of NiPc-GO, CoPc-GO and FePc-GO (**Figs. 2d-f, Figs. S46-S48**, and **Tables S4a-S4c**), reveal that the metal centers Ni, Co and Fe are coordinated with six C atoms from the GO lattice, with interatomic distances Ni/Co/Fe-C = 3.76-3.79 Å, as shown in the inset of **Figs. S49-S51**. Fitted structural parameters are given in **Tables S4a-S4c**. This interaction of GO and MPc molecules is also in line with the XPS spectra shown **in Fig. S16**. The external π ligand has been proven to increase the activity of the metal centers.[39,59] Therefore, we propose that the enhanced OER and ORR performances are due to the optimized electronic structure and the local coordination environment between the MPc molecules and the GO nanosheets.

Since the performance order for ORR (FePc-GO > CoPc-GO > NiPc-GO) is inverted with respect to OER (NiPc-GO > CoPc-GO > FePc-GO), we conclude that the metal centers behave differently in OER and ORR even though they display the same local coordination environment. To confirm this hypothesis, OER and ORR performances of the HSACs with well-defined coordination environments were theoretically evaluated by computing their free energy diagrams as shown in **Fig. 4** and **Tables S5-S6** (see SI for details). All calculations were conducted at the metal centers based on previous works using the so-called computational

hydrogen electrode approach.[27,60] For ORR (**Figs. 4b-d**), all elementary steps proceed spontaneously at U=0 V (but not for NiPc-GO in our case) because all electron transfer steps are exergonic (ΔG < 0). When the output potential increases above the determining potential (-0.93 V, 0.53 V and 0.54 V for NiPc-GO, CoPc-GO and FePc-GO in our case), where the energy gap (ΔG) between any two steps is zero, the ORR cannot proceed spontaneously between those two steps because the reactions are endergonic (ΔG > 0). The results for ORR show that FePc-GO is the best catalyst with a theoretical overpotential of 0.54 V, which correlates well with the experimental result. The best ORR activity of Fe centers among the series can be explained in terms of the number of d electrons N_d, and the oxidation state of the metal in the catalyst.[31] As shown in **Fig. S52**, the adsorption energies for all the intermediates obey a linear increasing relationship with N_d, suggesting that for the low N_d of 5 (due to the presence of Fe^{3+}) for Fe binding of the intermediates is more favorable compared to Co (N_d=6-7, because of small amounts of Co^{3+}) and Ni (N_d=8).[31] We further compared the free energies of O_2 and H_2O adsorbed on these three metal centers in **Table S6** and **Fig. S53**. The results show that Fe displays an extremely high adsorption affinity towards O_2, but moderate adsorption of H_2O. In other words, FePc-GO can easily capture O_2 from the electrolyte and also release H_2O easily again, which can be explained by Sabatier's principle and Nørskov's studies.[61] Recent works on Fe SACs also showed that the higher chemical valence of Fe^{3+} is favorable for CO_2 adsorption.[52] This could provide an explanation for the better ORR performance of FePc-GO compared to divalent Ni and Co. Calculations on other active sites, e. g. C and N atoms (**Table S5**) show that all energy changes in NiPc-GO at the first step are positive, indicating their thermodynamic inactivity for ORR, which is consistent with the experimental results shown in **Fig. 3d**. For both CoPc-GO and FePc-GO, the best theoretical overpotentials for ORR are found on the metal centers and the coordinated atoms are thermodynamically inactive for ORR (positive energies), *i.e.* the C and N atoms do not contribute to ORR.

For OER, the largest energy shift in the free energy diagram is considered as the primary energy barrier, which is defined as the theoretical overpotential for OER (green lines in **Figs. 4e-g**). This is because all proton-electron coupled transfer steps are exergonic (ΔG < 0), and the OER could proceed spontaneously as the applied potential increases above that overpotential. These results also show that FePc-GO is expected to be the best OER catalyst with a calculated overpotential of 1.69 V. These calculated results, however, contradict the experimental results at high potential ranges, but they are consistent with those at potential lower than around 1.45 V *vs*. RHE, in which the activity order is FePc-GO > CoPc-GO > NiPc-GO (**Fig. S52**). The same trends also emerged from five additional measurements using different electrodes (**Figs. S55-59**), and on a different electrochemical station (**Fig. S60**). Rotation ring disk measurements were further conducted to verify that O_2 was already produced at that potential range (**Fig. S61**). The results show that O_2 production starts at around 1.4 V *vs*. RHE. This implies that the FePc-GO catalyst is much more capable of initiating water oxidation reaction at a low potential, followed by CoPc-GO, and NiPc-GO, while at the higher potential the reaction activities follow the order NiPc-GO > CoPc-GO > FePc-GO. It appears that the reaction is more likely kinetically controlled at the higher potential. Since DFT calculations are a thermodynamic approach, we further conducted kinetic analyses for these three samples by electrochemical measurements (see SI for details). The results show that all of them display zero reaction order at lower pH (<10.5), followed by first-order kinetics at higher pH of 10.5-14 (**Fig. S62**). Interestingly, all of the samples show zero order under 0.5 V, proceeding to first order when crossing this turning point. Therefore, we believe that the OER is thermodynamically controlled at lower potentials, and turns to kinetic control beyond a critical voltage.

In recent works on graphene-based SACs, it has been demonstrated that the local coordination of metal centers and electronegativity of nearest neighbor species exert a crucial influence on the activity.[27,28] Non-metallic ligating atoms including C, N and S have also been proven to act as active sites or to influence the water oxidation.[31,32,62] Therefore, we propose that the local coordination of metallic atoms could contribute to the kinetic factors in our systems.

Determination of the influence of local environment on the OER from operando XAS and DFT calculations. To probe the structural changes around the active metal site under OER conditions, we performed operando XAS measurements for NiPc-GO, CoPc-GO and FePc-GO near the onset potential (see Supplementary Information for details). **Figs. 5a-c** show the normalized operando Ni, Co and Fe K-edge XANES spectra of NiPc-GO, CoPc-GO and FePc-GO catalysts at open-circuit condition (in 1 M KOH electrolyte), at applied potentials of 1.3, 1.4, 1.5 V *vs.* RHE, and after removal of the applied potential. As shown in the inset of **Figs. 5a-c**, under open-circuit voltage bias the metal Ni, Co and Fe absorption edges were slightly shifted to higher energy by approximately 0.08, 0.25 and 0.06 eV for NiPc-GO, CoPc-GO and FePc-GO, respectively. This indicates an increase in the oxidation state of the metal centers due to chemical adsorption of $OH^-/O_2/H_2O$ radicals from the electrolyte under the open-circuit condition. Moreover, during electrochemical OER at applied potentials of 1.3, 1.4 and 1.5 V *vs.* RHE, the absorption edges were further shifted to higher energy up to a maximum of ~0.41, ~0.95, and ~0.19 eV for NiPc-GO, CoPc-GO and FePc-GO, respectively. This indicates further increases in the oxidation state of the Ni, Co, and Fe metal centers upon catalytic activation. Due to the strong electronegativity of the –OH groups, they could balance the reduction trend of the applied voltage bias, and therefore the oxidation state is further increased,[63] as observed from the shifts in the raising absorption edge of the XANES spectra (**Figs. 5a-c**). This leads to a redistribution of the electrons in the Ni, Co and Fe 3d-orbitals between the four N ligands and the metal-O/-OH/-OOH bonding from the adsorbed oxo-species. This finding is consistent with previous operando XAS studies under OER conditions.[64,65] The intensity of the $1s \rightarrow 4p_z$ pre-edge peak of NiPc-GO (~8339 eV), CoPc-GO (~7717 eV) and the $1s \rightarrow 3d$ pre-edge peak of FePc-GO (~7114 eV), is consistently reduced under open-circuit voltage bias and under the operando applied potentials of 1.3, 1.4 and 1.5 V *vs.* RHE compared with their pristine counterparts. These results indicate that the square-planar D_{4h} symmetry of the Ni-N_4, Co-N_4 and Fe-N_4 moieties suffers only from small local structure distortions under operando conditions. This distorted structure is expected to considerably facilitate the adsorption of the reactants and intermediates on the catalysts' surface. Interestingly, the Ni, Co, and Fe absorption edges of NiPc-GO, CoPc-GO and FePc-GO were shifted back to lower energies when the applied potential was removed (**Figs. 5a-c**). This suggests that the changes in the oxidation states of the catalysts are reversible to some extent. The variations observed in the XANES spectra were more pronounced in CoPc-GO and NiPc-GO than in FePc-GO. Furthermore, the changes in the white line intensity and its slight shift in energy further suggest the existence of structural disorder. This also corroborates that the densities of unoccupied *d*-states and oxidation states of Ni, Co and Fe atoms change as a function of the applied potential.

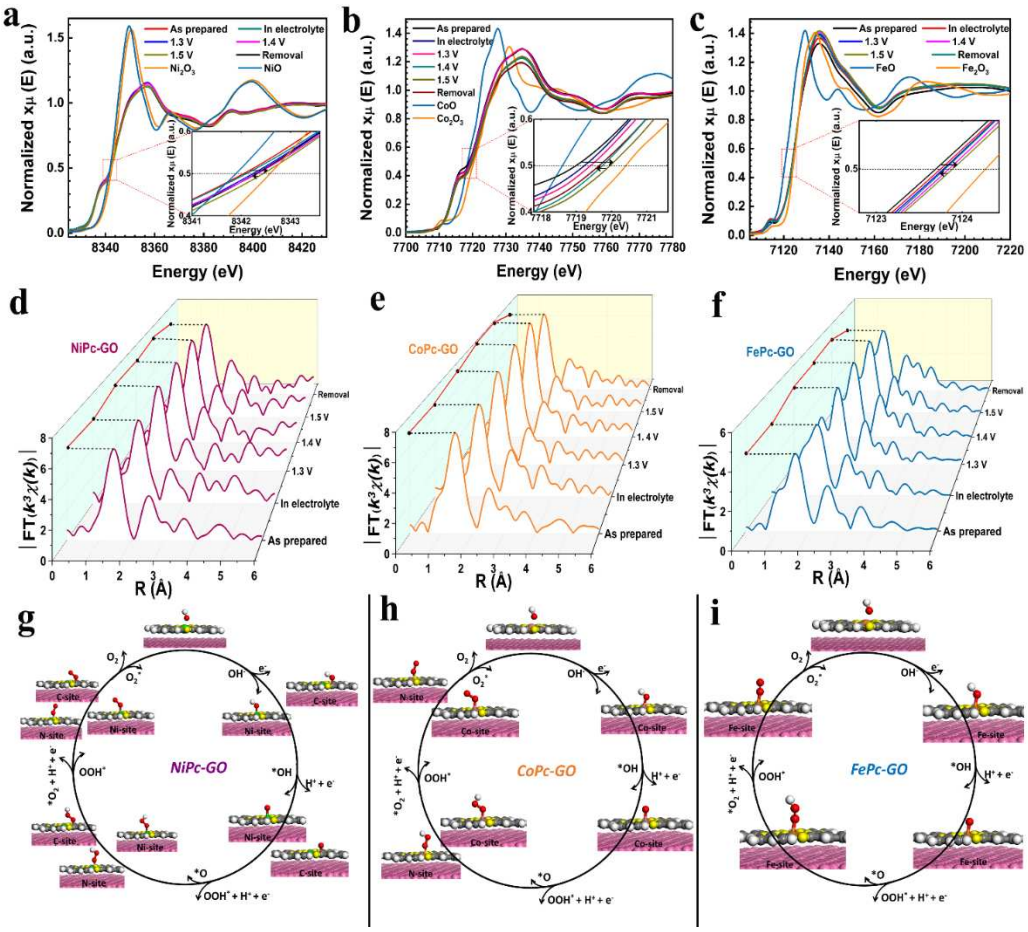

Figure 5. Operando XAS and calculated reaction pathways. (a-c) Ni, Co and Fe K-edges XANES and (d-f) Fourier-transform EXAFS spectra |FT(k³χ(k))| for pristine NiPc-GO, CoPc-GO and FePc-GO, at open circuit condition in 1 M KOH, at applied potentials of 1.3, 1.4 and 1.5 V *vs.* RHE, and after removal of the applied potential. (g-i) DFT simulations for analyses of the reaction pathways and reaction active sites: coordinating C, N atoms in NiPc-GO and N atoms in CoPc-GO contribute to the OER, providing multiple reaction pathways, while the Fe atom is the only active center in FePc-GO during OER.

The evolution of the local structure environment of the single active metal sites under operando conditions was further examined by operando EXAFS spectroscopy**. Figs. 5d-f** show the operando Ni, Co and Fe K-edge EXAFS spectra |FT(k³χ(k))| of NiPc-GO, CoPc-GO, FePc-GO under open-circuit conditions, at the applied potentials of 1.3, 1.4, and 1.5 V *vs.* RHE, and after removal of the applied potential. The relative intensities of the main peak in the |FT(k³χ(k))| spectra of NiPc-GO, CoPc-GO and FePc-GO consistently increase during electrochemical OER at the applied potential of 1.3, 1.4 and 1.5 V *vs.* RHE (red lines in **Figs. 5d-f**). This is due to the contribution from M-O/-OH/-OOH (M=Ni, Co, Fe) coordinations arising from the electrolyte during OER that overlap with the main bonding coordination of the Co-N_4 moieties, as shown in **Tables S4a-S4c.**[64] Interestingly, the intensities of the main peak in the |FT(k³χ(k))| spectra of all samples were reduced when the applied potential was removed. This agrees with the shift to low energy observed in the XANES spectra after removal of the applied potential (**Figs. 5a-c**), and indicates stability and reversible local structure variations under catalytic activation. To obtain quantitative values of interatomic distances, coordination numbers (N), and track the evolution of the local-structure of NiPc-GO, CoPc-GO and FePc-GO during operando OER, non-linear least-square fitting of their operando EXAFS spectra |FT(k³χ(k))| was carried out as shown in **Figs. S63-65** and **Tables S4a-S4c**. The optimized model-structures from DFT simulations

shown in **Figs. 5g-i** were used as model-structure. The results reveal that in the 1st-coordination shell, the metal Ni, Co and Fe centers are coordinated with four N atoms from the Pc-molecule and an oxygen atom, with bond distances Ni-N=1.91 Å; Ni-O=1.97 Å (NiPc-GO), Co-N=1.90 Å; Co-O=1.97 Å (CoPc-GO), and Fe-N=1.92 Å; Fe-O=2.04 Å (FePc-GO). The coordination numbers N-Ni/Co/Fe-O consistently decrease from a value as high as 0.7-0.8 at the applied potentials of 1.4-1.5 V *vs.* RHE, to 0.5-0.6 at 1.3 V, and 0.2-0.4 after removal the applied potential (**Tables S4a-S4c**). Other relevant structural parameters, and the contributions of each fitted single scattering path to the operando $|FT(k^3\chi(k))|$ spectra for NiPc-GO, CoPc-GO and FePc-GO at the applied potential of 1.5 V *vs.* RHE are shown in **Tables S4a-S4c** and **Figs. S66-S68**. The change in the intensities and position of the 2nd/3th coordination peaks at about ~2.2-3.3 Å and ~3.3-3.9 Å, respectively, which relates to backscattering from furthest neighboring C and N atoms are mainly due to changes in the disorder Debye-Waller factor (σ^2). This suggests that the C/N atoms in the 2nd/3th coordination shells also undergo some structural disorder under the applied operando conditions, and could also play specific roles in the catalytic activity. All in all, our operando XANES and EXAFS experiments clearly demonstrated that the electronic and local structure environment of HSACs is noticeably changed under realistic operando electrochemical OER conditions. The single active metal Ni, Co, Fe sites attain high-valence states due to the formation of HOO-/O-/HO-(Ni/Co/Fe)-N_4 moieties during the catalytic activation. Therefore, the formation of high-valence HOO-/O-/HO-(Ni/Co/Fe)-N_4 moieties under working condition are probably responsible for the high reactivity toward OER.

To further investigate the influence of the local ligating atoms on the activity, we selected NiPc-GO as a model-system and synthesized a series of samples under pyrolysis temperatures from 300 to 800 °C. Raman spectra show that the intensity of the peaks related to the local coordination near the metal centers, at around 1300 and 1700 cm^{-1}, gradually decrease as the synthesis temperature increases, and finally become similar to the spectrum of GO (**Fig. S69**). These results indicate that the local coordination environment around the Ni metal center is destroyed upon increasing the temperature. The XANES and EXAFS spectra were further analyzed to investigate structural transformations (**Fig. S70**). The square-planar D_{4h} symmetry of NiPc-GO entirely disappears at 800 °C and the edge is slightly shifted to lower energies. The $|FT(k^3\chi(k))|$ spectrum shows that the local structure retains the Ni-N_4 moiety in the first coordination shell, while the 2nd and 3rd M-N/C coordination shells vanished completely. These results further demonstrate that increasing temperatures promote structural disorder, up to destruction the local coordination. As expected, the performance for electrochemical water oxidation is significantly reduced upon the destruction of the local coordination as shown in **Fig. S71**. Moreover, LSV data of NiPc-GO-800 °C (**Fig. S73**) even show very apparent Ni oxidation peaks, further demonstrating the different behavior of Ni centers after drastic changes in the coordination environment. Analogous changes in the OER performance of CoPc-GO and FePc-GO were also observed after destruction of their local coordination environments at 800 °C (**Fig. S72**). The above results provide strong additional evidence that the coordination environment significantly influences the OER performance.

To confirm the above hypotheses, we further conducted DFT calculations on the coordinated C, N_1 and N_2 atoms (**Fig. S74**). The calculated free energies of *OH, *O and *OOH on the selected sites are listed in **Table S5**. The elementary reaction steps for all sites are presented in **Figs. S75-77**. Analyses for all sites in FePc-GO show that Fe site is probably the only active site for OER. The free energies for intermediates *OH, *O, and *OOH adsorbed on Fe sites are far lower than for adsorption on the C, N1 and N2 sites (**Table S5**), which indicates that they are bound much easier on the Fe atoms rather than on other sites (**Fig. 5i**). This high binding affinity of FePc-GO also occurs for O_2 (**Table S7**), however, the strong binding of O_2 also implies a difficult desorption of O_2 in the last step. This single-center pathway and excessive binding towards O_2 may account for the low OER performance. CoPc-GO shows the same trend at the first step as *OH can only be adsorbed on Co atoms.

In the third step, however, *O produced from the second step also moves to N1 sites for the following reaction steps (**Fig. 5h**), because the adsorption energy on N1 is equal to that of Co (**Table S5**). For NiPc-GO, impressively, all the intermediates can be equally adsorbed on Ni and C sites, and at the third step, from *O to *OOH, N1 atoms can also participate in the reaction as the respective free energy is even slightly smaller than for Ni and C sites (**Table S5**). The different adsorption behavior toward O_2, *OH, *O and *OOH leading to diversity of reaction pathways is a plausible reason for the higher activity of NiPc-GO at the higher potential. Once the reactions cross their energy barriers, NiPc-GO and CoPc-GO catalysts could provide more active sites and pathways for OER (**Fig. 5h**). As the active sites and pathways are related to the reaction kinetics, we conclude that the catalysts follow two different processes: a thermodynamically controlled process at a low potential range, followed by kinetic control at high potential range. This multi-site mechanism has also been observed in other metal-graphene based catalysts.[31]

CONCLUSIONS

In this work, graphene based HSACs from clear-cut MPc (M = Ni, Co, Fe; Pc = phthalocyanine) precursors were constructed as highly performing model systems for the comparative investigations into their OER/ORR pathways. The well-defined coordination of these HSACs provided experimental insight into key relationships between metal centers, their coordination environments and the resulting OER/ORR activity. First, the near-perfect coordination of the active sites within the MN_4C_8/N_4 moiety after integration into the graphene substrate was corroborated with XAS and ADF-STEM analyses. Furthermore, specific members of the HSAC series outperformed most previously reported single metal center catalysts in OER and ORR activity. This notably enhanced performance is associated with the formation of electronic channels *via* π-π conjugation of graphene and MPc molecules, as is evident from both our theoretical and experimental studies. The specific role of the metal centers was furthermore analyzed with a combination of DFT simulations and a large set of (electro)analytical data. Interestingly, the ORR activity trend (FePc-GO > CoPc-GO > NiPc-GO) is opposite to the OER performance (NiPc-GO > CoPc-GO > FePc-GO). Operando XAS spectra combined with DFT results show that the high valence of Fe(III) centers with a lower N_d value exhibit the strongest bonding affinity to O_2, therefore giving rise to the highest ORR performance among the series. In contrast, the coordination environment of NiPc-GO and CoPc-GO provides a wider selection of alternative N/C-site OER pathways, resulting in their higher activity.

In summary, we provide the experimental insight into SACs for OER to comprehensively promote the understanding of their challenging coordination-performance relationships. Our results explain the limited OER performance of current SACs with $M\text{-}N_4$ moieties and open up strategies *via* tuned coordination environments for improving their OER performance.

EXPERIMENTAL SECTION

Materials: Graphene oxide (GO), 15-20 sheets, 4-10% edge-oxidized was purchased from Sigma-Aldrich. Nickel ($C_{32}H_{16}N_8Ni$), cobalt ($C_{32}H_{16}N_8Co$) and iron ($C_{32}H_{16}N_8Fe$) phthalocyanine were bought from Alfa Aesar. Ar gas used in the synthesis was purchased from PanGas AG, Switzerland, ≥ 99.999 %.

Materials synthesis: First, 40 mg GO was pretreated in 20 mL ethanol using an ultrasonic bath for 1 h. 10 mg $C_{32}H_{16}N_8Ni$ dispersed in 10 mL ethanol was gradually added into the GO dispersed solution. The mixture was then treated by ultrasonic dispersion for 1 h and subsequently subjected to magnetic stirring for 24 h. After the dispersion procedure, the mixture was further exposed to 60 °C under air condition for slow evaporation. The above powder was finally treated with a pyrolysis step in a tube furnace at temperatures from 300 - 800 °C under protective Ar atmosphere. The same processes were applied to synthesize $C_{32}H_{16}N_8Co$ and $C_{32}H_{16}N_8Fe$ coupled with GO.

Electrochemical measurements: Electrochemical water oxidation measurements were carried out on an Autolab PGSTAT204 electrochemistry workstation with the standard three-electrode system in 1 M KOH electrolyte. Glassy carbon (GC) electrode loaded with catalyst was used as working electrode. 2.5 mg of catalyst was dispersed in 0.5

mL water and 0.5 mL ethanol. After 30 min ultrasonic treatment, 50 µL of 5 wt % Nafion solution was further added into the above solution with another 60 min of sonication to form a homogeneous ink. Then 5 µL of the catalyst ink (containing 12.5 µg of catalyst) was loaded onto a glassy-carbon electrode (2 mm in diameter). Ag/AgCl with saturated KCl filling solution and platinum rod were used as reference electrode and counter electrode, respectively. The control experiments using Pt rod and blank FTO as working electrodes were conducted in **Fig. S78** to further eliminate the possible interference of trace Pt in the OER activity, which has been reported before.[66,67] All the catalyst electrodes were continuously scanned for 10 times CV before measuring polarization curves **Fig. S79**. The scan rates for all of the LSV and CV measurements were set to 10 mV/s to minimize the capacitive current. Electrochemical impedance spectroscopy (EIS) studies were performed when the working electrode was biased at certain potentials while sweeping the frequency from 10 kHz to 10 mHz with a 5 mV ac amplitude. E(iR-corrected) = E - iR, where i is the current and R (20 Ω in this work) is the uncompensated electrolyte Ohmic resistance measured by EIS.

The electrochemical oxygen reduction studies were carried out at room temperature in 0.1 M KOH. The working electrodes in this study were the RDE and a RRDE (GC disc with r = 2.5 mm and 375 µm gap, Pt ring with width = 375 µm, rinner = 2.875 mm, and router = 3.250 mm. A standard three-electrode system equipped with a graphite rod as the counter electrode and a Ag/AgCl electrode (3 M KCl) was employed as the reference electrode, respectively (Metrohm Autolab PGSTAT302N potentiostat). To prepare the working electrode, 3.0 mg of catalysts were dispersed in 600 µL ethanol and 20 µL of 5 wt % Nafion solution and sonicated for 30 mins to form a homogeneous ink. Next, 3.00 µL of homogeneous ink was carefully loaded onto RDE or RRDE to achieve a 0.200 mg cm^{-2} loading amount. Before each ORR measurement, the electrolyte was bubbled with high purity of O_2 for 30 min and maintained over the electrolyte surface during the ORR testing to sustain the O_2 saturation. Prior to measurements the working electrode was subjected to at least 10 CV cycles in the potential range of 0.2 V-1.2 V *vs.* RHE at 100 mV s^{-1} to reach a stable state. LSV was carried out at a rotation speed of 1600 rpm at a scan rate of 5.0 mV s^{-1} for the acquisition of polarization curves. The RRDE measurement was performed at a constant ring potential of 1.3 V *vs.* RHE.

The number of electrons transferred and H_2O_2 yield were evaluated from RRDE measurements using the following equations:

Number of electron transfer (n) during ORR:

$$n=4\times I_d/(I_d+I_r/N) \quad (1)$$

where Id and Ir are disk and ring current densities, respectively, N is the current collection efficiency of the Pt ring which is 0.25.

Percentage of peroxide (% HO^{2-}) during the ORR testing:

$$\%\ HO^{2-} = 200\times I_r/(I_d\times N+I_r)$$

The electron transfer number and kinetics of ORR from RDE measurements were evaluated using the following Koutecky–Levich equation:

$$\frac{1}{j}=\frac{1}{j_l}+\frac{1}{j_k}=\frac{1}{B\omega^{0.5}}+\frac{1}{j_k} \quad (2)$$

$$B = 0.64nFAC_oD_o^{2/3}V^{-1/6} \quad (3)$$

$$j_k = nFkC_o \quad (4)$$

where J is the measured current density, J_l and J_k are the limiting and kinetic current densities, B is the slope of K-L plots, ω is the rotation rate of the disk electrode, n is the number of transferred electrons in ORR, F is the Faraday constant (96 485 C mol^{-1}), A is the geometric area of the electrode (A = 0.07065 cm^2), C_o is the concentration of O_2 which is 1.2×10^{-6} mol cm^{-3} in 0.1 M KOH, D_o is the O_2 diffusion coefficient (1.9×10^{-5} cm^2 s^{-1}), V is the kinematic viscosity of the solution (0.01 cm^2 s^{-1}), and k is the electron transfer rate constant.[68,69]

Materials characterization: Powder X-ray diffraction (PXRD) patterns were recorded on a STOE STADI P diffractometer (transmission mode, Ge monochromator) with M_oK_α radiation. Raman spectra were measured with a Renishaw Ramascope as pristine powder samples on quartz glass slides. X-ray photoelectron spectroscopy (XPS) measurements were conducted on a Thermo ESCALAB 250Xi. Elemental analysis was performed at Mikroanalytisches Labor Pascher (Remagen/Germany). Inductively coupled plasma mass spectrometry (ICP-MS)

measurements were carried out on an Agilent 8800 instrument. All samples were first annealed under air atmosphere and then dissolved in aqua regia. Annular dark-field scanning transmission electron microscopy (ADF-STEM) was performed on aberration-corrected JEOL ARM300CF STEM equipped with a JEOL ETA corrector operated at an accelerating voltage of 80 kV located in the electron Physical Sciences Imaging Centre (ePSIC) at Diamond Light Source.

X-ray absorption spectroscopy (XAS): The *ex Situ* and operando XANES and EXAFS experiments were carried out at the European synchrotron radiation facility (ESRF), Swiss-Norwegian beamline BM31, Grenoble, France, and at the beamline KMC-2, Helmholtz-Zentrum Berlin HZB-BESSY II, respectively. The X-ray beam was collimated with a Si coated mirror and the energy was scanned with a channel-cut SiGe[111] monochromator. Measurements were done in a three-ionization chamber configuration in transmission mode. For energy calibration, the spectra of metal Ni, Co and Fe foils were simultaneously measured at the second ionization camber. *Ex Situ* measurements were carried out on solid powder samples dispersed in cellulose. Operando experiments were done using an in-house designed electrochemical cell filled with 1 M KOH electrolyte with thinness < 200 μm as described before.[70] Ag/AgCl in saturated KCl and a Pt rod were used as reference/counter electrode, respectively. The working electrode was fabricated by loading the catalyst ink on carbon paper using the same routine described in Ref 55. The post-catalytic XAS spectra after OER catalysis were measured after 3000 CV cycles scanned at the potential range of 0-1.8 V *vs.* RHE. The measured EXAFS spectra $k^3\chi(k)$, were obtained by standard data reduction, absorption edge energy calibration and background subtraction as implemented in ATHENA.[71] The spectra were then reduced into the range $\Delta k \approx 3\text{-}10$ Å^{-1} and Fourier-Transform to $|FT(k^3\chi(k))|$ into the real-space interval $\Delta R \approx 0\text{-}6$ Å. To calculate the main values for interatomic distances, coordination numbers (N), and Debye-Waller factors (σ^2), nonlinear least-squares fitting of the $FT|(k^3\chi(k))|$ spectra was carried out with ARTEMIS[71] using the optimized atomic clusters obtained from DFT simulations (**Figs. S49-S51 and Figs. 5g-h**), as input for ATOMS calculations as it is implemented in IFEFFIT.[71] Amplitude and phase shift for single and multiple scattering paths were computed using FEFF6 code.[72] The amplitude reduction factor So^2 was calculated from fitting the $|FT(k^3\chi(k))|$ spectra of the respective standard Ni, Co or Fe metal foils and kept constant for fitting the $|FT(k^3\chi(k))|$ spectra of NiPc-GO, CoPc-GO and FePc-GO. The coordination numbers (N), of N and C atoms as defined from structural optimization from the DFT calculations (**Figs. S49-S51 and Figs. 5g-i**), were kept constant for fitting the operando $|FT(k^3\chi(k))|$ spectra of NiPc-GO, CoPc-GO and FePc-GO. However, the N-values of O atoms were varied manually until a good match between the simulated spectra and the expected interatomic distances was reached. The energy shift ΔE_o was first treated as a free parameter for fitting the first M-N coordination shells, then it was adjusted manually for fitting the other scattering paths until a good match between the simulated spectra and likely interatomic distances was achieved. In this way, only two parameters, named Debye-Waller factors (σ^2), and the change in the interatomic distances ΔR were treated as free fitting parameters. All $|FT(k^3\chi(k))|$ spectra were fitted without phase corrections using the Hanning-window function into the range kmin-kmax=3-10 Å^{-1}; Rmin-Rmax=1.0-4.5 Å, with 15 independent points and 10 or 12 variables for *ex Situ* and operando EXAFS spectra, respectively. This fitting approach yield the lowest R-factors (see **Table S4**), and the best fitting of the operando $|FT(k^3\chi(k))|$ spectra from the input DFT model-structures.

Density functional theory (DFT) calculations: Density function theory calculation were performed by using the CP2K package.[73] PBE functional[74] with Grimme D_3 correction[75] was used to describe the system. Unrestricted Kohn-Sham DFT has been used as the electronic structure method in the framework of the Gaussian and plane waves method.[76,77] The Goedecker-Teter-Hutter (GTH) pseudopotentials,[78,79] DZVPMOLOPT-GTH basis sets[76] were utilized to describe the molecules. A plane-wave energy cutoff of 500 Ry has been employed. The geometries are optimized using the BFGS algorithm and the convergence criterion for the forces was set to 10^{-4} bohr/hartree. We employed a graphene supercell with surface periodicity of 8 ×

10 including 160 atoms as a basis to construct the model. A vacuum region of 15 Å was created to eliminate the interaction between mirror images. To determine the adsorption site of the molecules on the graphene support, we have examined metal centers located at hollow (in the center of the benzene ring), bridge (between two carbon atoms) and top (on the top of the carbon atom) sites. We also examined the orientation of the molecules on graphene with different angles (**Fig. S8o** and **Table S8**). After optimization, only the hollow site as shown in the manuscript was found to be stable. All the structures are in the attached files.

The Gibbs free energy is calculated using

$$\Delta G = EDFT + \Delta ZPE - T\Delta S \quad (5)$$

where G is the Gibbs free energy, EDFT is the electronic energy from DFT calculations, ZPE is zero-point-energy, T is temperature of 298 K. ΔS is the change in entropy. They were calculated from DFT modeling of vibrational frequencies and using standard tables for gas-phase molecules.[8o] The potential-dependence of reaction free energies in elementary steps involving proton-electron transfers was evaluated using the computational hydrogen electrode (CHE) approach.[6o] In this approach, a reversible hydrogen electrode (RHE) is used as a reference. The OER proceeds through four consecutive proton/electron transfer steps:

Overall Reaction: $2H_2O = 4H^+ + 4e^- + 2O_2$ (6)

First deprotonation: $H_2O = {}^*OH + (H^+ + e^-)$ (7)

Second deprotonation: ${}^*OH + (H^+ + e^-) = {}^*O + 2(H^+ + e^-)$ (8)

Third deprotonation: ${}^*O + H_2O + 2(H^+ + e^-) = {}^*OOH + 3(H^+ + e^-)$ (9)

Fourth deprotonation: ${}^*OOH + 3(H^+ + e^-) = O_2 + 4(H^+ + e^-)$ (10)

via the intermediates OH^*, O^*, and OOH^* adsorbed species, where * stands for the adsorbed intermediates.

The charge density difference is defined as

$$\Delta\rho = \rho M/GR - \rho M - \rho GR \quad (11)$$

Where Δρ is the charge density difference, ρM/GR is the total electron density of the molecule on the graphene and ρM, ρGR are the total electron densities of isolated molecule and graphene, respectively.

ASSOCIATED CONTENT

Supporting Information. Supporting information is provided including XRD, Raman, HRTEM, XPS, XAS, and ICP-MS data, electrochemical characterizations and related DFT details. This material is available free of charge *via* the Internet at http://pubs.acs.org.

AUTHOR INFORMATION

Corresponding Author

greta.patzke@chem.uzh.ch

Author Contributions

All authors have given approval to the final version of the manuscript.

The authors declare no competing financial interests.

ACKNOWLEDGMENT

This work has been supported by the University of Zurich Research Priority Program (URPP) for Solar Light to Chemical Energy Conversion (LightChEC) and by the Swiss National Science Foundation (Sinergia Grant No. CRSII2_160801/1). W. Wan thanks the China Scholarship Council (CSC) for his PhD fellowship. We thank Diamond Light Source for access and support in use of the electron Physical Science Imaging Centre (EM16967). We thank Viviane Grange (University of Zurich) for elemental analysis measurements, Hermann Emerich (ESRF Grenoble) for beamline support, and Dr. Rolf Erni (Electron Microscopy Center, Empa Dübendorf) for TEM measurements.

REFERENCES

(1) Roger, I.; Shipman, M. A.; Symes, M. D. Earth-Abundant Catalysts for Electrochemical and Photoelectrochemical Water Splitting. *Nat. Rev. Chem.* **2017**, *1*, 928.

(2) Wang, J.; Cui, W.; Liu, Q.; Xing, Z.; Asiri, A. M.; Sun, X. Recent Progress in Cobalt-Based Heterogeneous Catalysts for Electrochemical Water Splitting. *Adv. Mater.* **2016**, *28*, 215–230.

(3) Han, L.; Dong, S.; Wang, E. Transition-Metal (Co, Ni, and Fe)-Based Electrocatalysts for the Water Oxidation Reaction. *Adv. Mater.* **2016**, *28*, 9266–9291.

(4) Hunter, B. M.; Gray, H. B.; Müller, A. M. Earth-Abundant Heterogeneous Water Oxidation Catalysts. *Chem. Rev.* **2016**, *116*, 14120–14136.

(5) Hu, C.; Zhang, L.; Zhao, Z.-J.; Li, A.; Chang, X.; Gong, J. Synergism of Geometric Construction and Electronic Regulation: 3D Se-(NiCo)Sx /(OH)x Nanosheets for Highly Efficient Overall Water Splitting. *Adv. Mater.* **2018**, *30*, 1705538.

(6) Tang, T.; Jiang, W.-J.; Niu, S.; Liu, N.; Luo, H.; Chen, Y.-Y.; Jin, S.-F.; Gao, F.; Wan, L.-J.; Hu, J.-S. Electronic and Morphological Dual Modulation of Cobalt Carbonate Hydroxides by Mn Doping toward Highly Efficient and Stable

Bifunctional Electrocatalysts for Overall Water Splitting. *J. Am. Chem. Soc.* **2017**, *139*, 8320–8328.
(7) Wan, S.; Qi, J.; Zhang, W.; Wang, W.; Zhang, S.; Liu, K.; Zheng, H.; Sun, J.; Wang, S.; Cao, R. Hierarchical Co(OH)F Superstructure Built by Low-Dimensional Substructures for Electrocatalytic Water Oxidation. *Adv. Mater.* **2017**, *29*, 1700286.
(8) Tian, T.; Gao, H.; Zhou, X.; Zheng, L.; Wu, J.; Li, K.; Ding, Y. Study of the Active Sites in Porous Nickel Oxide Nanosheets by Manganese Modulation for Enhanced Oxygen Evolution Catalysis. *ACS Energy Lett.* **2018**, *3*, 2150–2158.
(9) Huang, Z.-F.; Song, J.; Dou, S.; Li, X.; Wang, J.; Wang, X. Strategies to Break the Scaling Relation toward Enhanced Oxygen Electrocatalysis. *Matter* **2019**, *1*, 1494–1518.
(10) Huang, Z.-F.; Song, J.; Du, Y.; Xi, S.; Dou, S.; Nsanzimana, J. M. V.; Wang, C.; Xu, Z. J.; Wang, X. Chemical and Structural Origin of Lattice Oxygen Oxidation in Co–Zn Oxyhydroxide Oxygen Evolution Electrocatalysts. *Nat. Energy* **2019**, *4*, 329–338.
(11) Xu, C.; Sun, W.; Dong, Y.; Dong, C.; Hu, Q.; Ma, B.; Ding, Y. A Graphene Oxide–Molecular Cu Porphyrin-Integrated BiVO4 Photoanode for Improved Photoelectrochemical Water Oxidation Performance. *J. Mater. Chem. A* **2020**, *8*, 4062–4072.
(12) Wang, A.; Li, J.; Zhang, T. Heterogeneous Single-Atom Catalysis. *Nat. Rev. Chem.* **2018**, *2*, 65–81.
(13) Chen, Z.; Vorobyeva, E.; Mitchell, S.; Fako, E.; Ortuño, M. A.; López, N.; Collins, S. M.; Midgley, P. A.; Richard, S.; Vilé, G.; Pérez-Ramírez, J. A Heterogeneous Single-Atom Palladium Catalyst Surpassing Homogeneous Systems for Suzuki Coupling. *Nat. Nanotechnol.* **2018**, *13*, 702–707.
(14) Peng, Y.; Lu, B.; Chen, S. Carbon-Supported Single Atom Catalysts for Electrochemical Energy Conversion and Storage. *Adv. Mater.* **2018**, *30*, 1801995.
(15) Zhang, J.; Liu, J.; Xi, L.; Yu, Y.; Chen, N.; Sun, S.; Wang, W.; Lange, K. M.; Zhang, B. Single-Atom Au/NiFe Layered Double Hydroxide Electrocatalyst: Probing the Origin of Activity for Oxygen Evolution Reaction. *J. Am. Chem. Soc.* **2018**, *140*, 3876–3879.
(16) Zhang, J.; Zhao, Y.; Guo, X.; Chen, C.; Dong, C.-L.; Liu, R.-S.; Han, C.-P.; Li, Y.; Gogotsi, Y.; Wang, G. Single Platinum Atoms Immobilized on an MXene as an Efficient Catalyst for the Hydrogen Evolution Reaction. *Nat. Catal.* **2018**, *1*, 985–992.
(17) Chen, Y.; Ji, S.; Chen, C.; Peng, Q.; Wang, D.; Li, Y. Single-Atom Catalysts: Synthetic Strategies and Electrochemical Applications. *Joule* **2018**, *2*, 1242–1264.
(18) Zhu, C.; Fu, S.; Shi, Q.; Du, D.; Lin, Y. Single-Atom Electrocatalysts. *Angew. Chem. Int. Ed.* **2017**, *56*, 13944–13960.
(19) Bi, W.; Li, X.; You, R.; Chen, M.; Yuan, R.; Huang, W.; Wu, X.; Chu, W.; Wu, C.; Xie, Y. Surface Immobilization of Transition Metal Ions on Nitrogen-Doped Graphene Realizing High-Efficient and Selective CO_2 Reduction. *Adv. Mater.* **2018**, *30*, 1706617.
(20) Han, A.; Chen, W.; Zhang, S.; Zhang, M.; Han, Y.; Zhang, J.; Ji, S.; Zheng, L.; Wang, Y.; Gu, L.; Chen, C.;Peng, Q.; Wang, D.; Li, Y. A Polymer Encapsulation Strategy to Synthesize Porous Nitrogen-Doped Carbon-Nanosphere-Supported Metal Isolated-Single-Atomic-Site Catalysts. *Adv. Mater.* **2018**, *30*, 1706508.
(21) Li, X.; Bi, W.; Chen, M.; Sun, Y.; Ju, H.; Yan, W.; Zhu, J.; Wu, X.; Chu, W.; Wu, C.; Xie, Y. Exclusive Ni-N_4 Sites Realize Near-Unity CO Selectivity for Electrochemical CO_2 Reduction. *J. Am. Chem. Soc.* **2017**, *139*, 14889–14892.
(22) Pan, Y.; Liu, S.; Sun, K.; Chen, X.; Wang, B.; Wu, K.; Cao, X.; Cheong, W.-C.; Shen, R.; Han, A.; Chen, Z.; Zheng, L.; Luo, J.; Lin, Y.; Liu, Y.; Wang, D.; Peng, Q.; Zhang, Q.; Chen, C.; Li, Y. A Bimetallic Zn/Fe Polyphthalocyanine-Derived Single-Atom Fe-N_4 Catalytic Site: A Superior Trifunctional Catalyst for Overall Water Splitting and Zn-Air Batteries. *Angew. Chem. Int. Ed.* **2018**, *57*, 8614–8618.
(23) Wang, X. X.; Cullen, D. A.; Pan, Y.-T.; Hwang, S.; Wang, M.; Feng, Z.; Wang, J.; Engelhard, M. H.; Zhang, H.; He, Y.; Shao, Y.; Su, D.; More, K. L.; Spendelow, J. S.; Wu, G. Nitrogen-Coordinated Single Cobalt Atom Catalysts for Oxygen Reduction in Proton Exchange Membrane Fuel Cells. *Adv. Mater.* **2018**, *30*, 1706758.
(24) Yang, H. B.; Hung, S.-F.; Liu, S.; Yuan, K.; Miao, S.; Zhang, L.; Huang, X.; Wang, H.-Y.; Cai, W.; Chen, R.; Gao, J.; Yang, X.; Chen, W.; Huang, Y.; Chen, H. M.; Li, C. M.; Zhang, T.; Liu, B. Atomically Dispersed Ni(i) as the Active Site for Electrochemical CO2 Reduction. *Nat. Energy* **2018**, *3*, 140–147.
(25) Zhang, L.; Jia, Y.; Gao, G.; Yan, X.; Chen, N.; Chen, J.; Soo, M. T.; Wood, B.; Yang, D.; Du, A.; Yao, X. Graphene Defects Trap Atomic Ni Species for Hydrogen and Oxygen Evolution Reactions. *Chem* **2018**, *4*, 285–297.
(26) Li, X.; Huang, X.; Xi, S.; Miao, S.; Ding, J.; Cai, W.; Liu, S.; Yang, X.; Yang, H.; Gao, J.; Wang, J.; Huang, Y.; Zhang, T.; Liu, B. Single Cobalt Atoms Anchored on Porous N-Doped Graphene with Dual Reaction Sites for Efficient Fenton-like Catalysis. *J. Am. Chem. Soc.* **2018**, *140*, 12469–12475.
(27) Xu, H.; Cheng, D.; Cao, D.; Zeng, X. C. A Universal Principle for a Rational Design of Single-Atom Electrocatalysts. *Nat. Catal.* **2018**, *1*, 339–348.
(28) Fillol, J. L.; Codolà, Z.; Garcia-Bosch, I.; Gómez, L.; Pla, J. J.; Costas, M. Efficient Water Oxidation Catalysts Based on Readily Available Iron Coordination Complexes. *Nat. Chem.* **2011**, *3*, 807–813.
(29) Wu, Q.; Xiao, M.; Wang, W.; Cui, C. *in Situ* Coordination Environment Tuning of Cobalt Sites for Efficient Water Oxidation. *ACS Catal.* **2019**, *9*, 11734–11742.
(30) Christopher, P. Single-Atom Catalysts Are All Sites Created Equal? *ACS Energy Lett.* **2019**, *4*, 2249–2250.

(31) Fei, H.; Dong, J.; Feng, Y.; Allen, C. S.; Wan, C.; Volosskiy, B.; Li, M.; Zhao, Z.; Wang, Y.; Sun, H.; An, P.; Chen, W.; Guo, Z.; Lee, C.; Chen, D.; Shakir, I.; Liu, M.; Hu, T.; Li, Y.; Kirkland, A.; Duan, X.; Huang, Y. General Synthesis and Definitive Structural Identification of MN4C4 Single-Atom Catalysts with Tunable Electrocatalytic Activities. *Nat. Catal.* **2018**, *1*, 63–72.

(32) Hou, Y.; Qiu, M.; Kim, M. G.; Liu, P.; Nam, G.; Zhang, T.; Zhuang, X.; Yang, B.; Cho, J.; Chen, M.; Yuan, C.; Lei, L.; Feng, X. Atomically Dispersed Nickel-Nitrogen-Sulfur Species Anchored on Porous Carbon Nanosheets for Efficient Water Oxidation. *Nat. Commun.* **2019**, *10*, 1392.

(33) Li, Y.; Wu, Z.-S.; Lu, P.; Wang, X.; Liu, W.; Liu, Z.; Ma, J.; Ren, W.; Jiang, Z.; Bao, X. High-Valence Nickel Single-Atom Catalysts Coordinated to Oxygen Sites for Extraordinarily Activating Oxygen Evolution Reaction. *Adv. Sci.* **2020**, *7*, 1903089.

(34) Cao, Y.; Chen, S.; Luo, Q.; Yan, H.; Lin, Y.; Liu, W.; Cao, L.; Lu, J.; Yang, J.; Yao, T.; Wei, S. Atomic-Level Insight into Optimizing the Hydrogen Evolution Pathway over a Co_1-N_4 Single-Site Photocatalyst. *Angew. Chem. Int. Ed.* **2017**, *56*, 12191–12196.

(35) Wan, W.; Wei, S.; Li, J.; Triana, C. A.; Zhou, Y.; Patzke, G. R. Transition Metal Electrocatalysts Encapsulated into N-Doped Carbon Nanotubes on Reduced Graphene Oxide Nanosheets: Efficient Water Splitting through Synergistic Effects. *J. Mater. Chem. A* **2019**, *46*, 337.

(36) Li, X.; Chai, G.; Xu, X.; Liu, J.; Zhong, Z.; Cao, A.; Tao, Z.; You, W.; Kang, L. Electrocatalytic Reduction of CO_2 to CO over Iron Phthalocyanine-Modified Graphene Nanocomposites. *Carbon* **2020**, *167*, 658–667.

(37) Yan, X.; Xu, X.; Zhong, Z.; Liu, J.; Tian, X.; Kang, L.; Yao, J. The Effect of Oxygen Content of Carbon Nanotubes on the Catalytic Activity of Carbon-Based Iron Phthalocyanine for Oxygen Reduction Reaction. *Electrochim. Acta* **2018**, *281*, 562–570.

(38) Arul, A.; Pak, H.; Moon, K. U.; Christy, M.; Oh, M. Y.; Nahm, K. S. Metallomacrocyclic–Carbon Complex: A Study of Bifunctional Electrocatalytic Activity for Oxygen Reduction and Oxygen Evolution Reactions and Their Lithium-Oxygen Battery Applications. *Appl. Catal. B: Environ* **2018**, *220*, 488–496.

(39) Pan, Y.; Lin, R.; Chen, Y.; Liu, S.; Zhu, W.; Cao, X.; Chen, W.; Wu, K.; Cheong, W.-C.; Wang, Y.; Zheng, L.; Luo, J.; Lin, Y.; Liu, Y.; Liu, C.; Li, J.; Lu, Q.; Chen, X.; Wang, D.; Peng, Q. *et al.* Design of Single-Atom Co-N_5 Catalytic Site: A Robust Electrocatalyst for CO_2 Reduction with Nearly 100% CO Selectivity and Remarkable Stability. *J. Am. Chem. Soc.* **2018**, *140*, 4218–4221.

(40) Fei, H.; Dong, J.; Arellano-Jiménez, M. J.; Ye, G.; Dong Kim, N.; Samuel, E. L. G.; Peng, Z.; Zhu, Z.; Qin, F.; Bao, J.; Yacaman, M. J.; Ajayan, P. M.; Chen, D.; Tour, J. M. Atomic Cobalt on Nitrogen-Doped Graphene for Hydrogen Generation. *Nat. Commun.* **2015**, *6*, 8668.

(41) Jiang, K.; Siahrostami, S.; Zheng, T.; Hu, Y.; Hwang, S.; Stavitski, E.; Peng, Y.; Dynes, J.; Gangisetty, M.; Su, D.; Attenkofer, K.; Wang, H. Isolated Ni Single Atoms in Graphene Nanosheets for High-Performance CO2 Reduction. *Energy Environ. Sci.* **2018**, *11*, 893–903.

(42) Liu, P.; Zhao, Y.; Qin, R.; Mo, S.; Chen, G.; Gu, L.; Chevrier, D. M.; Zhang, P.; Guo, Q.; Zang, D.; Wu, B.; Fu, G.; Zheng, N. Photochemical Route for Synthesizing Atomically Dispersed Palladium Catalysts. *Science* **2016**, *352*, 797–801.

(43) Yang, L.; Cheng, D.; Xu, H.; Zeng, X.; Wan, X.; Shui, J.; Xiang, Z.; Cao, D. Unveiling the High-Activity Origin of Single-Atom Iron Catalysts for Oxygen Reduction Reaction. *P. Natl. Acad. Sci. USA* **2018**, *115*, 6626–6631.

(44) Zhang, C.; Yang, S.; Wu, J.; Liu, M.; Yazdi, S.; Ren, M.; Sha, J.; Zhong, J.; Nie, K.; Jalilov, A. S.; Li, Z.; Li, H.; Yakobson, B. I.; Wu, Q.; Ringe, E.; Xu, H.; Ajayan, P. M.; Tour, J. M. Electrochemical CO_2 Reduction with Atomic Iron-Dispersed on Nitrogen-Doped Graphene. *Adv. Energy Mater.* **2018**, *8*, 1703487.

(45) Guo, J.; Yan, X.; Liu, Q.; Li, Q.; Xu, X.; Kang, L.; Cao, Z.; Chai, G.; Chen, J.; Wang, Y.; Yao, J. The Synthesis and Synergistic Catalysis of Iron Phthalocyanine and Its Graphene-Based Axial Complex for Enhanced Oxygen Reduction. *Nano Energy* **2018**, *46*, 347–355.

(46) Liu, W.; Zhang, L.; Liu, X.; Liu, X.; Yang, X.; Miao, S.; Wang, W.; Wang, A.; Zhang, T. Discriminating Catalytically Active FeNx Species of Atomically Dispersed Fe-N-C Catalyst for Selective Oxidation of the C-H Bond. *J. Am. Chem. Soc.* **2017**, *139*, 10790–10798.

(47) Karen Chen-Wiegart, Y.-C.; Harris, W. M.; Lombardo, J. J.; Chiu, W. K. S.; Wang, J. Oxidation States Study of Nickel in Solid Oxide Fuel Cell Anode Using X-Ray Full-Field Spectroscopic Nano-Tomography. *Appl. Phys. Lett.* **2012**, *101*, 253901.

(48) Liang, X.; Zhong, Y.; Zhu, S.; He, H.; Yuan, P.; Zhu, J.; Jiang, Z. The Valence and Site Occupancy of Substituting Metals in Magnetite Spinel Structure Fe3–xMxO4 (M = Cr, Mn, Co and Ni) and Their Influence on Thermal Stability: An XANES and TG-DSC Investigation. *Solid State Sci.* **2013**, *15*, 115–122.

(49) Pan, D.; Jian, J. K.; Ablat, A.; Li, J.; Sun, Y. F.; Wu, R. Structure and Magnetic Properties of Ni-Doped AlN Films. *J. Appl. Phys.* **2012**, *112*, 53911.

(50) Wang, L.; Wen, Y.; Ji, Y.; Cao, H.; Li, S.; He, S.; Bai, H.; Liu, G.; Zhang, L.; Bao, H.; Wang, J.; Li, Y.; Zhang, B.; Peng, H. The 3d–5d Orbital Repulsion of Transition Metals in Oxyhydroxide Catalysts Facilitates Water Oxidation. *J. Mater. Chem. A* **2019**, *7*, 14455–14461.

(51) Chen, H.; Zhang, Y.; He, Q.; Zhang, H.; Xu, S.; He, X.; Ji, H. A Facile Route to Fabricate Double Atom Catalysts with Controllable Atomic Spacing for the r-WGS Reaction. *J. Mater. Chem. A* **2020**, *8*, 2364–2368.

(52) Gu, J.; Hsu, C.-S.; Bai, L.; Chen, H. M.; Hu, X. Atomically Dispersed Fe^{3+} Sites Catalyze Efficient CO_2 Electroreduction to CO. *Science* **2019**, *364*, 1091–1094.
(53) Wang, J.; Ge, X.; Liu, Z.; Thia, L.; Yan, Y.; Xiao, W.; Wang, X. Heterogeneous Electrocatalyst with Molecular Cobalt Ions Serving as the Center of Active Sites. *J. Am. Chem. Soc.* **2017**, *139*, 1878–1884.
(54) Wang, X.; Vasileff, A.; Jiao, Y.; Zheng, Y.; Qiao, S.-Z. Electronic and Structural Engineering of Carbon-Based Metal-Free Electrocatalysts for Water Splitting. *Adv. Mater.* **2019**, *31*, 1803625.
(55) Zhao, Y.; Nakamura, R.; Kamiya, K.; Nakanishi, S.; Hashimoto, K. Nitrogen-Doped Carbon Nanomaterials as Non-Metal Electrocatalysts for Water Oxidation. *Nat. Commun.* **2013**, *4*, 2390.
(56) Yan, X.; Xu, X.; Liu, Q.; Guo, J.; Kang, L.; Yao, J. Functionalization of Multi-Walled Carbon Nanotubes with Iron Phthalocyanine *via* a Liquid Chemical Reaction for Oxygen Reduction in Alkaline Media. *J. Power Sources* **2018**, *389*, 260–266.
(57) Wu, Y.; Jiang, Z.; Lu, X.; Liang, Y.; Wang, H. Domino Electroreduction of CO_2 to Methanol on a Molecular Catalyst. *Nature* **2019**, *575*, 639–642.
(58) Zhang, X.; Wu, Z.; Zhang, X.; Li, L.; Li, Y.; Xu, H.; Li, X.; Yu, X.; Zhang, Z.; Liang, Y.; Wang, H. Highly Selective and Active CO_2 Reduction Electrocatalysts Based on Cobalt Phthalocyanine/Carbon Nanotube Hybrid Structures. *Nat. Commun.* **2017**, *8*, 14675.
(59) Duan, L.; Bozoglian, F.; Mandal, S.; Stewart, B.; Privalov, T.; Llobet, A.; Sun, L. A Molecular Ruthenium Catalyst with Water-Oxidation Activity Comparable to That of Photosystem II. *Nat. Chem.* **2012**, *4*, 418–423.
(60) Nørskov, J. K.; Rossmeisl, J.; Logadottir, A.; Lindqvist, L.; Kitchin, J. R.; Bligaard, T.; Jónsson, H. Origin of the Overpotential for Oxygen Reduction at a Fuel-Cell Cathode. *J. Phys. Chem. B* **2004**, *108*, 17886–17892.
(61) Medford, A. J.; Vojvodic, A.; Hummelshøj, J. S.; Voss, J.; Abild-Pedersen, F.; Studt, F.; Bligaard, T.; Nilsson, A.; Nørskov, J. K. From the Sabatier Principle to a Predictive Theory of Transition-Metal Heterogeneous Catalysis. *J. Catal.* **2015**, *328*, 36–42.
(62) Zhang, J.; Zhao, Y.; Chen, C.; Huang, Y.-C.; Dong, C.-L.; Chen, C.-J.; Liu, R.-S.; Wang, C.; Yan, K.; Li, Y.; Wang, G. Tuning the Coordination Environment in Single-Atom Catalysts to Achieve Highly Efficient Oxygen Reduction Reactions. *J. Am. Chem. Soc.* **2019**, *141*, 20118–20126.
(63) Cao, L.; Luo, Q.; Liu, W.; Lin, Y.; Liu, X.; Cao, Y.; Zhang, W.; Wu, Y.; Yang, J.; Yao, T.; Wei, S. Identification of Single-Atom Active Sites in Carbon-Based Cobalt Catalysts During Electrocatalytic Hydrogen Evolution. *Nat. Catal.* **2019**, *2*, 134–141.
(64) Bai, L.; Hsu, C.-S.; Alexander, D. T. L.; Chen, H. M.; Hu, X. A Cobalt-Iron Double-Atom Catalyst for the Oxygen Evolution Reaction. *J. Am. Chem. Soc.* **2019**, *141*, 14190–14199.
(65) Görlin, M.; Chernev, P.; Ferreira de Araújo, J.; Reier, T.; Dresp, S.; Paul, B.; Krähnert, R.; Dau, H.; Strasser, P. Oxygen Evolution Reaction Dynamics, Faradaic Charge Efficiency, and the Active Metal Redox States of Ni-Fe Oxide Water Splitting Electrocatalysts. *J. Am. Chem. Soc.* **2016**, *138*, 5603–5614.
(66) Chen, R.; Yang, C.; Cai, W.; Wang, H.-Y.; Miao, J.; Zhang, L.; Chen, S.; Liu, B. Use of Platinum as the Counter Electrode to Study the Activity of Nonprecious Metal Catalysts for the Hydrogen Evolution Reaction. *ACS Energy Lett.* **2017**, *2*, 1070–1075.
(67) Lopes, P. P.; Strmcnik, D.; Tripkovic, D.; Connell, J. G.; Stamenkovic, V.; Markovic, N. M. Relationships between Atomic Level Surface Structure and Stability/Activity of Platinum Surface Atoms in Aqueous Environments. *ACS Catal.* **2016**, *6*, 2536–2544.
(68) Liang, Y.; Li, Y.; Wang, H.; Zhou, J.; Wang, J.; Regier, T.; Dai, H. Co_3O_4 Nanocrystals on Graphene as a Synergistic Catalyst for Oxygen Reduction Reaction. *Nat. Mater.* **2011**, *10*, 780–786.
(69) Sultan, S.; Tiwari, J. N.; Jang, J.-H.; Harzandi, A. M.; Salehnia, F.; Yoo, S. J.; Kim, K. S. Highly Efficient Oxygen Reduction Reaction Activity of Graphitic Tube Encapsulating Nitrided Co_xFe_y Alloy. *Adv. Energy Mater.* **2018**, *8*, 1801002.
(70) Yang, Y.; Wang, Y.; Xiong, Y.; Huang, X.; Shen, L.; Huang, R.; Wang, H.; Pastore, J. P.; Yu, S.-H.; Xiao, L.; Brock, J. D.; Zhuang, L.; Abrun˜a, H. D. *In Situ* X-ray Absorption Spectroscopy of a Synergistic Co-Mn Oxide Catalyst for the Oxygen Reduction Reaction. *J. Am. Chem. Soc.* **2019**, *141*, 1463–1466.
(71) Ravel, B.; Newville, M. ATHENA, ARTEMIS, HEPHAESTUS: Data Analysis for X-Ray Absorption Spectroscopy Using IFEFFIT. *J. Synchrotron Radiat.* **2005**, *12*, 537–541.
(72) Ankudinov, A. L.; Ravel, B.; Rehr, J. J.; Conradson, S. D. Real-Space Multiple-Scattering Calculation and Interpretation of X-Ray-Absorption Near-Edge Structure. *Phys. Rev. B* **1998**, *58*, 7565–7576.
(73) Hutter, J.; Iannuzzi, M.; Schiffmann, F.; VandeVondele, J. Cp2k: Atomistic Simulations of Condensed Matter Systems. *Comput. Mol. Sci.* **2014**, *4*, 15–25.
(74) Perdew; Burke; Ernzerhof. Generalized Gradient Approximation Made Simple. *Phys. Rev. Lett.* **1996**, *77*, 3865–3868.
(75) Grimme, S. Semiempirical GGA-Type Density Functional Constructed with a Long-Range Dispersion Correction. *J. Comput. Chem.* **2006**, *27*, 1787–1799.
(76) VandeVondele, J.; Hutter, J. Gaussian Basis Sets for Accurate Calculations on Molecular Systems in Gas and Condensed Phases. *J. Chem. Phys.* **2007**, *127*, 114105.

(77) VandeVondele, J.; Krack, M.; Mohamed, F.; Parrinello, M.; Chassaing, T.; Hutter, J. Quickstep: Fast and Accurate Density Functional Calculations Using a Mixed Gaussian and Plane Waves Approach. *Comput. Phys. Commun.* **2005**, *167*, 103–128.

(78) Goedecker; Teter; Hutter. Separable Dual-Space Gaussian Pseudopotentials. *Phys. Rev. B* **1996**, *54*, 1703–1710.

(79) Hartwigsen, C.; Goedecker, S.; Hutter, J. Relativistic Separable Dual-Space Gaussian Pseudopotentials from H to Rn. *Phys. Rev. B* **1998**, *58*, 3641–3662.

(80) Valdés, Á.; Qu, Z.-W.; Kroes, G.-J.; Rossmeisl, J.; Nørskov, J. K. Oxidation and Photo-Oxidation of Water on TiO2 Surface. *J. Phys. Chem. C* **2008**, *112*, 9872–9879.

Table of Contents

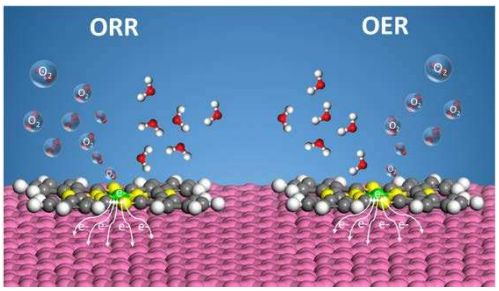

Supporting Information

Bifunctional Single Atom Electrocatalysts: Coordination-Performance Correlations and Reaction Pathways

Wenchao Wan,[1] Carlos A. Triana,[1] Jinggang Lan,[1] Jingguo Li,[1] Christopher S. Allen,[2] Yonggui Zhao,[1] Marcella Iannuzzi[1] and Greta R. Patzke*[1]

[1] University of Zurich, Department of Chemistry, Winterthurerstrasse 190, CH-8057 Zürich, Switzerland.

[2] Electron Physical Science Imaging Center, Diamond Light Source Ltd, Didcot, Oxfordshire, UK. Department of Materials, University of Oxford, Oxford, UK.

Table of Contents

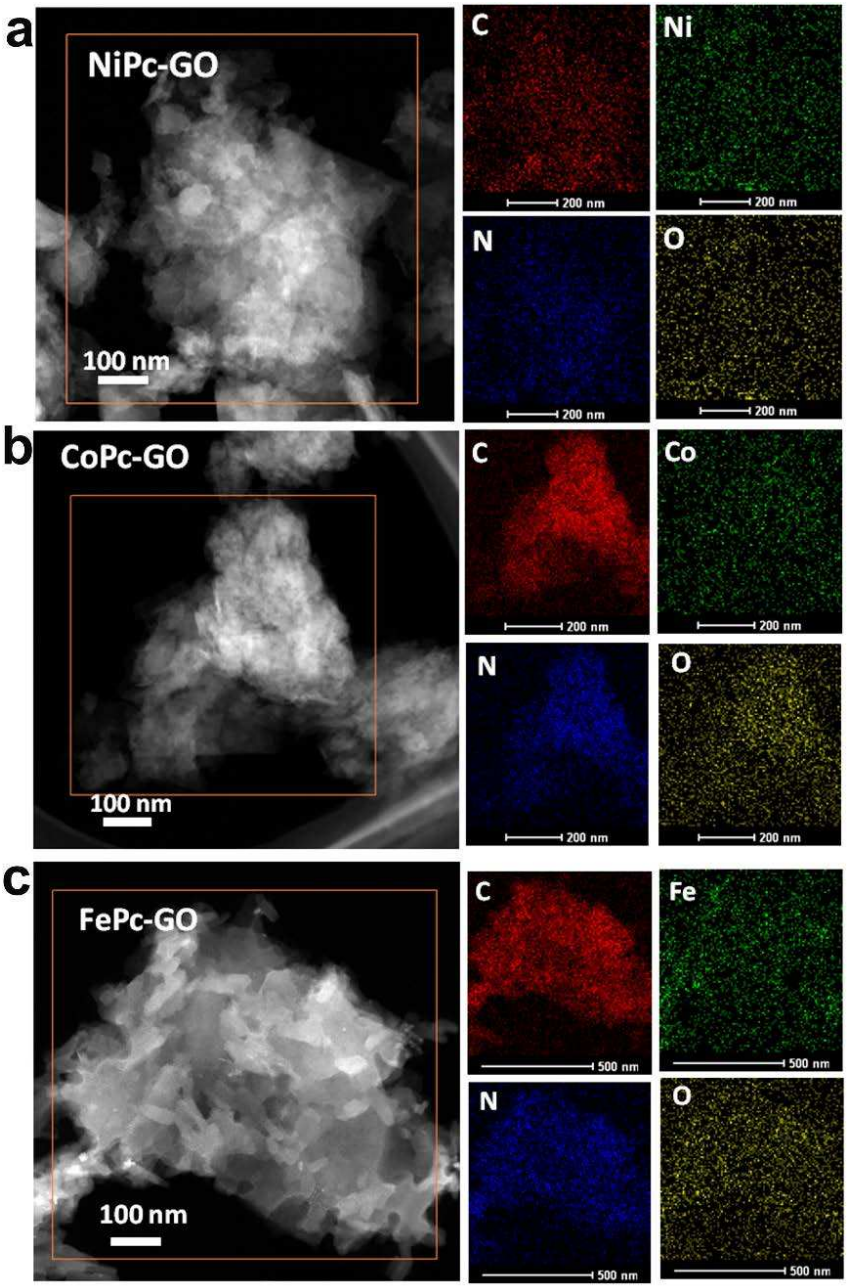

Figure S1. EDX mapping of NiPc-GO, CoPc-GO and FePc-GO.

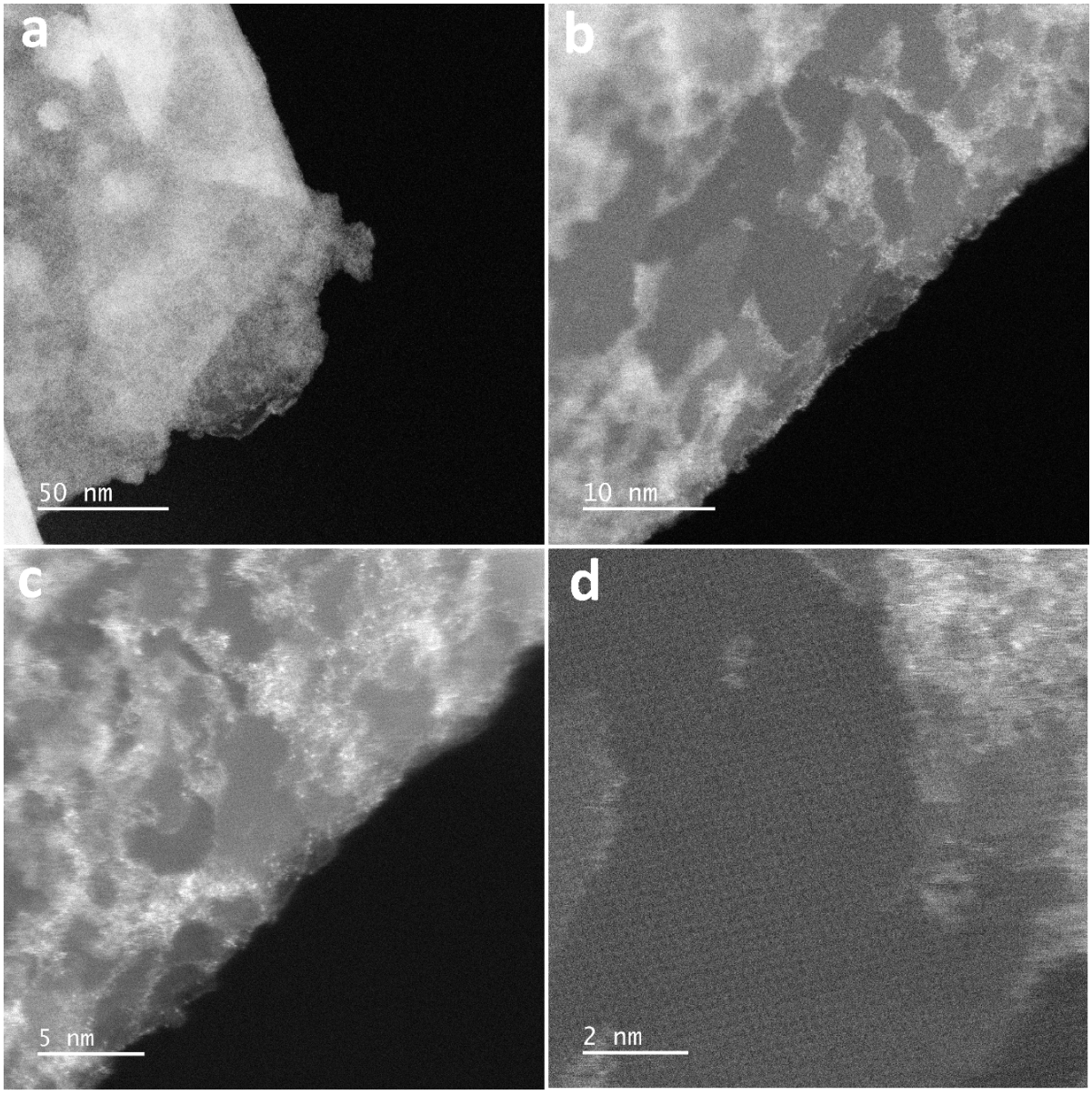

Figure S2. Annular Dark Field (ADF)-STEM images of NiPc-GO at different magnifications. The bright areas in the images represent the NiPc molecules covering the surface of GO.

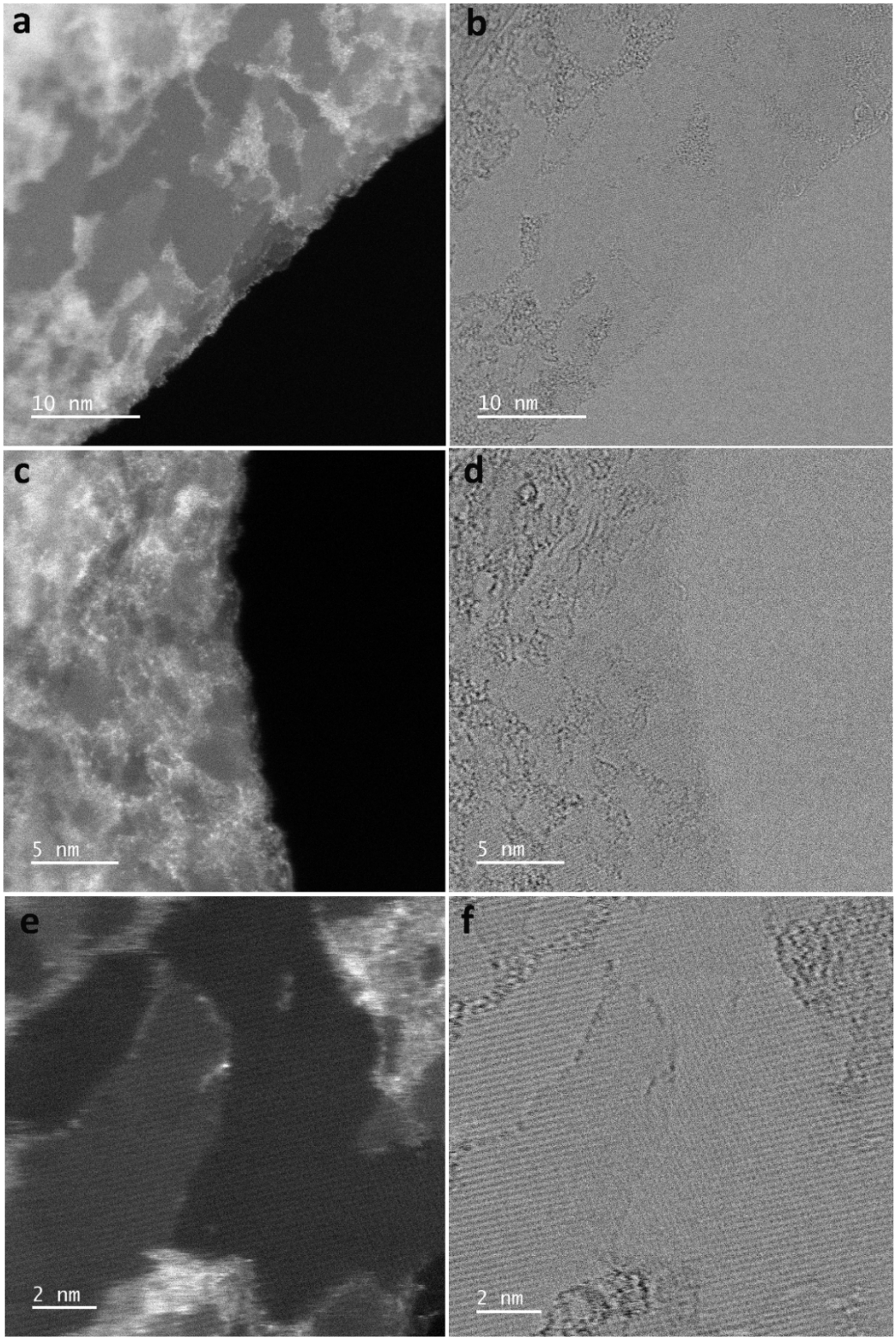

Figure S3. STEM images of NiPc-GO at different magnifications: Annular Dark Field (ADF)-STEM images (a, c, e), and their corresponding Bright Field (ABF)-STEM images (b, d, f). The dark areas in the ABF-STEM images (b, d, f) are the NiPc molecules.

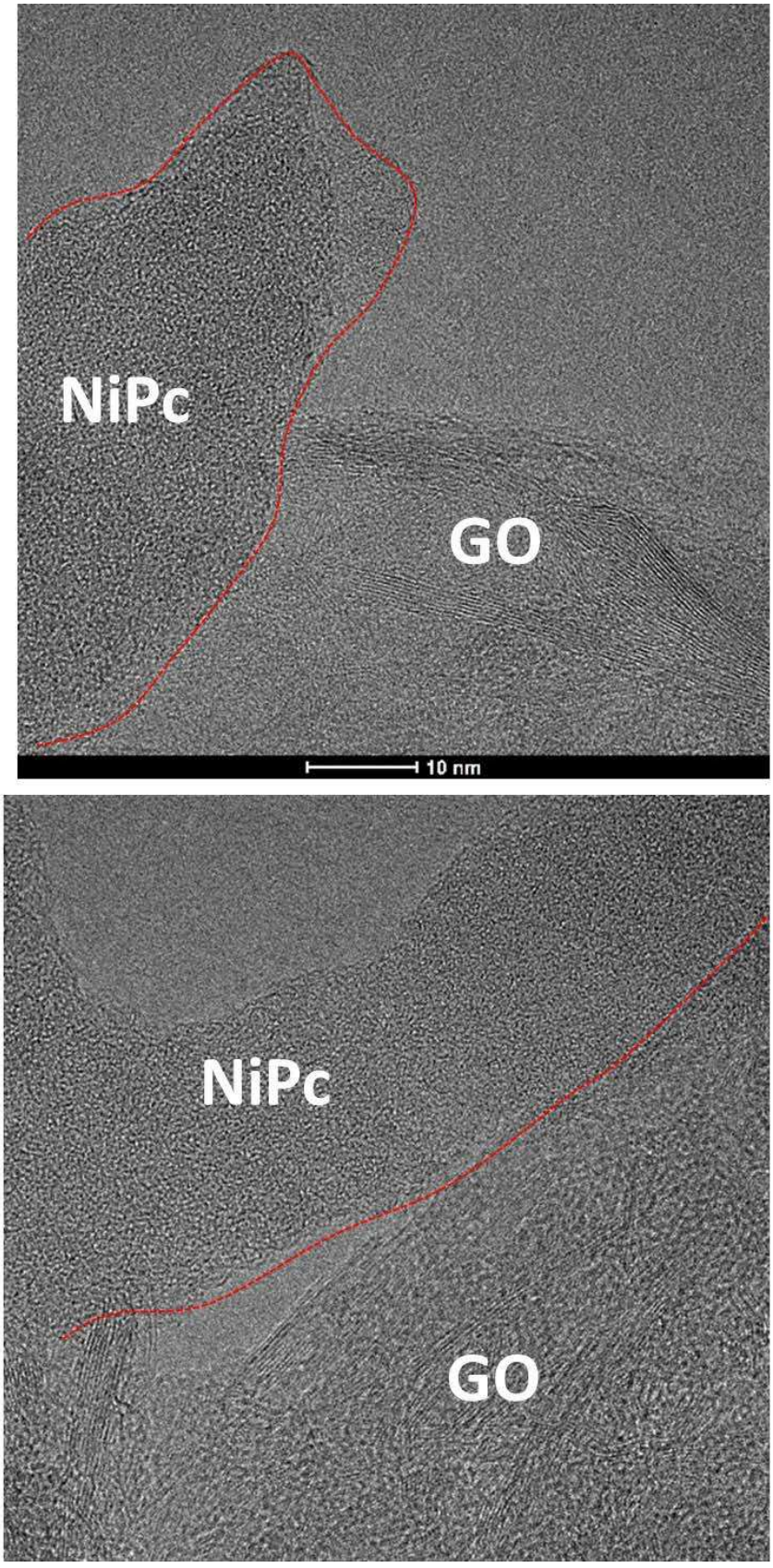

Figure S4. HRTEM images of NiPc-GO.

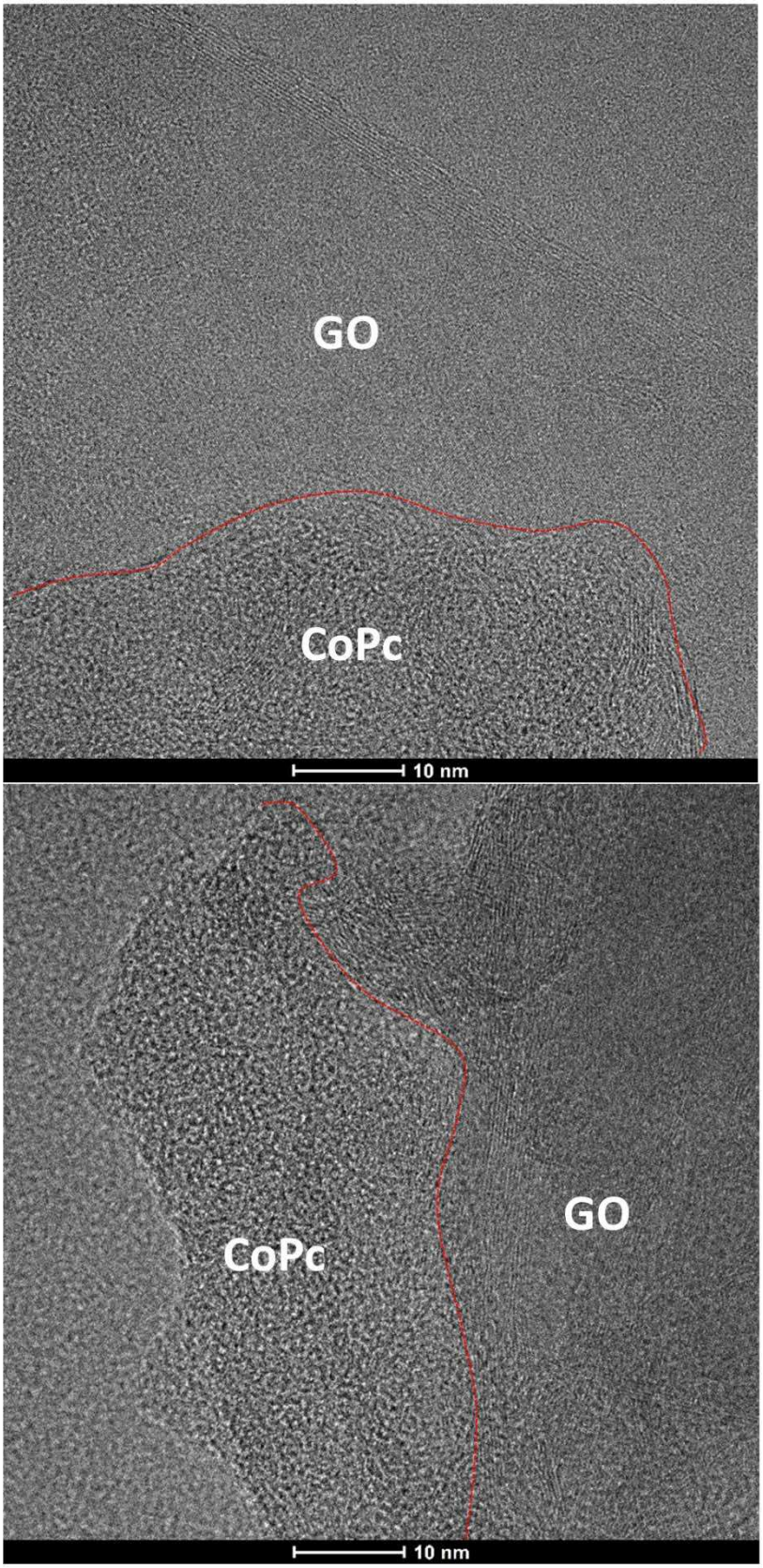

Figure S5. HRTEM images of CoPc-GO.

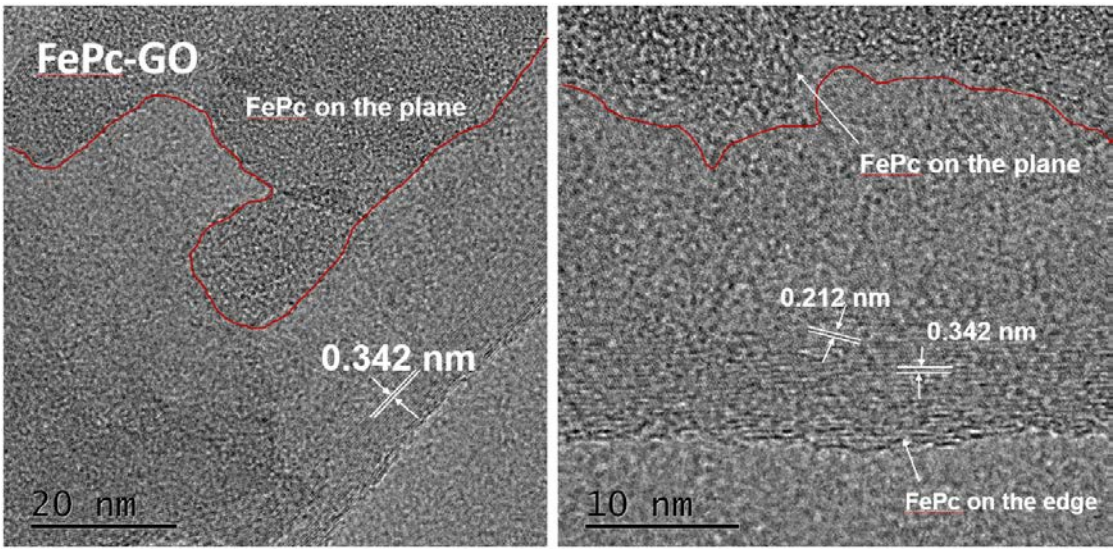

Figure S6. HRTEM images of FePc-GO.

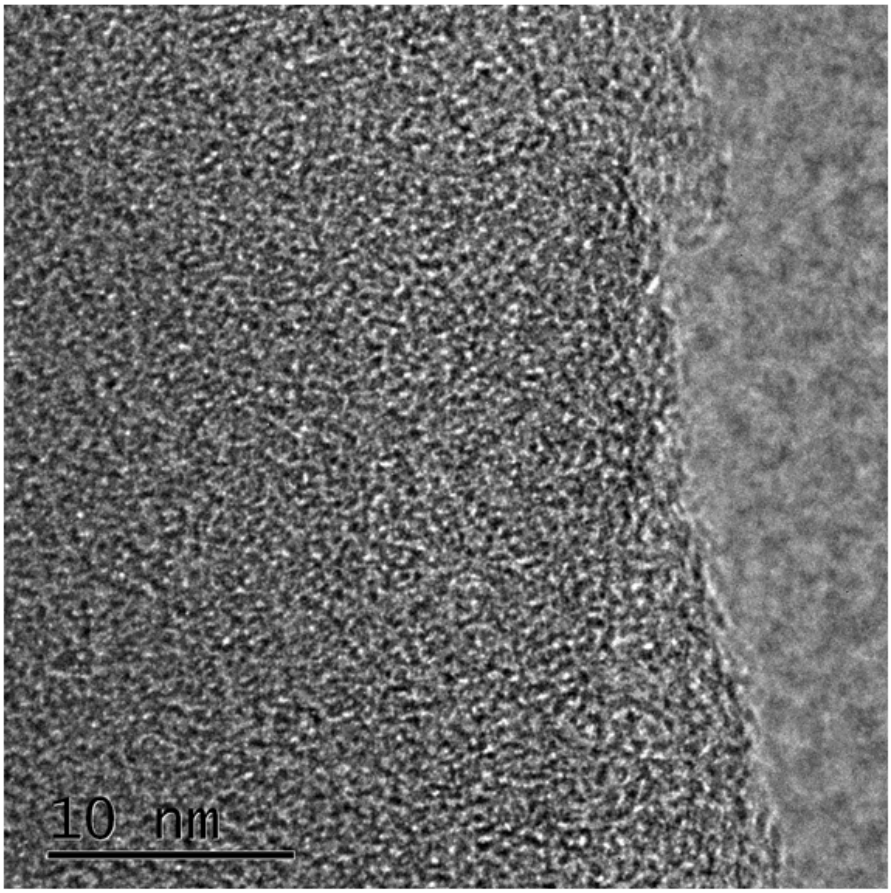

Figure S7. HRTEM images of pure NiPc reference.

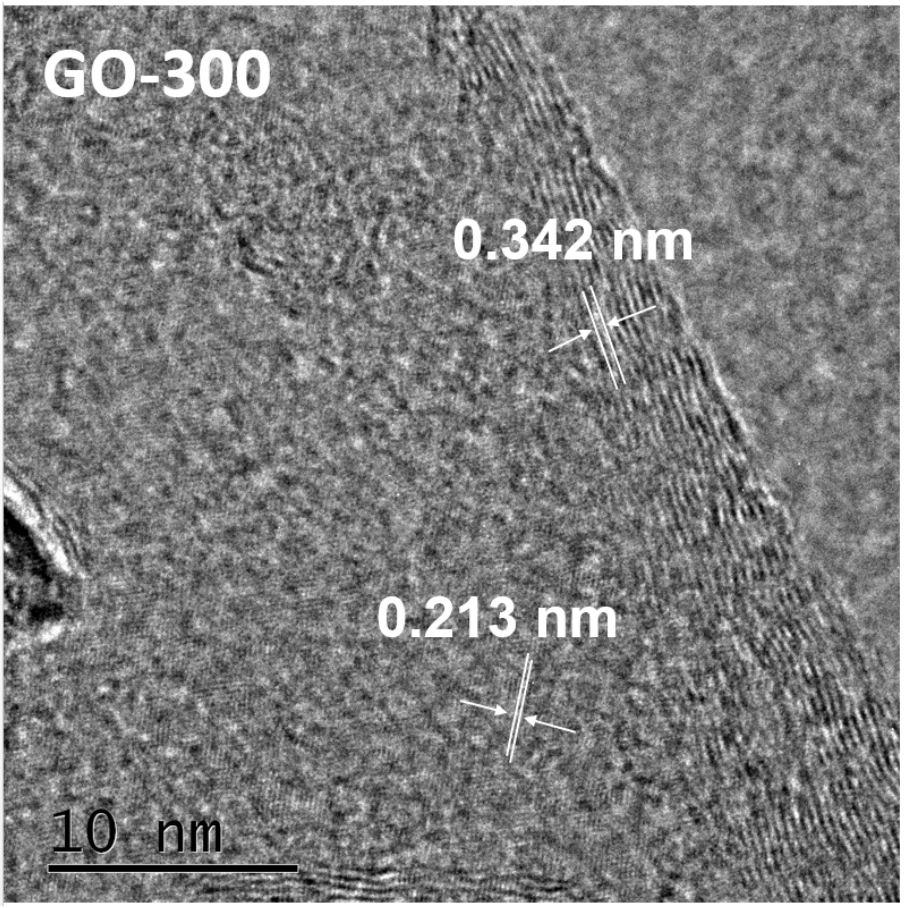

Figure S8. HRTEM image of GO after pyrolysis at 300 °C under N_2 atmosphere.

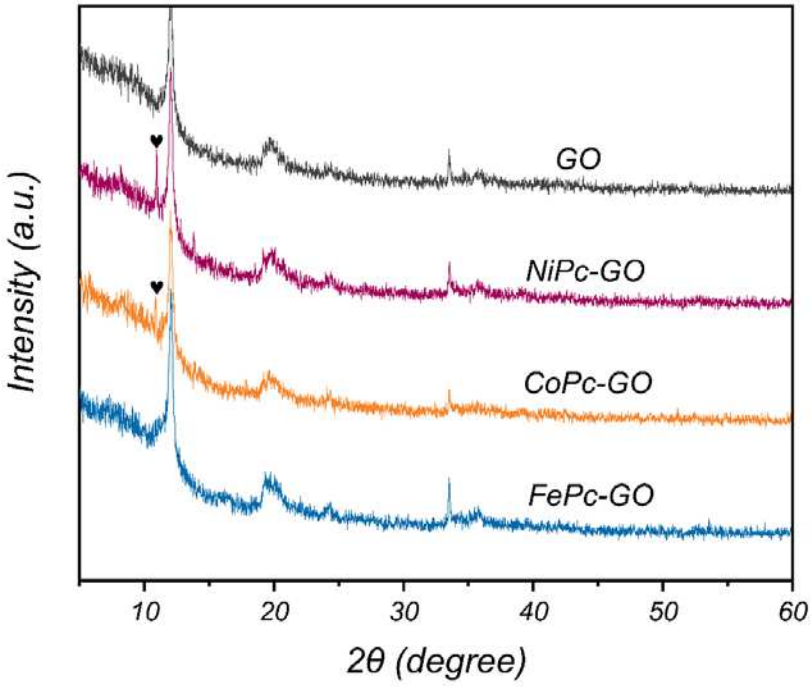

Figure S9. PXRD patterns of raw GO, NiPc-GO, CoPc-GO and FePc-GO, the marked signals are from MPcs.

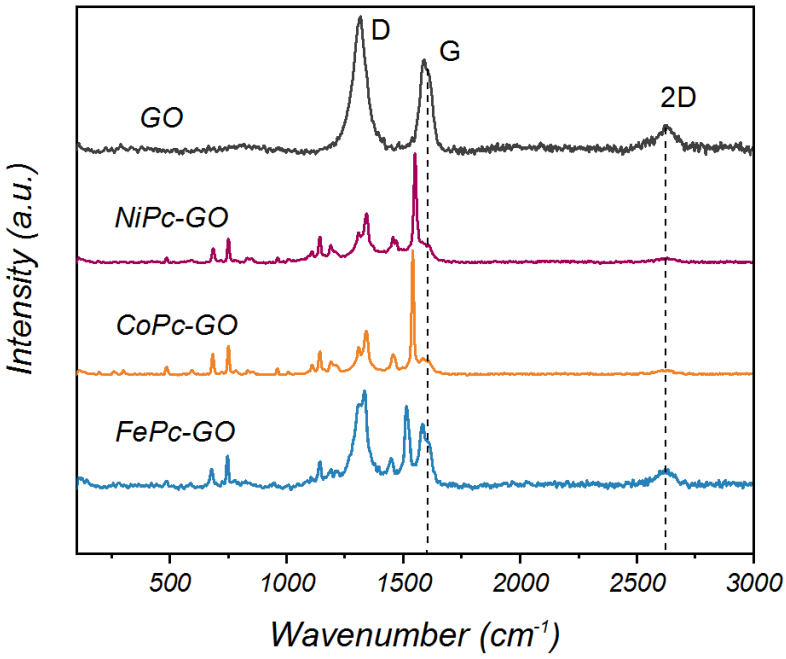

Figure S10. Raman spectra of raw GO, NiPc-GO, CoPc-GO and FePc-GO.

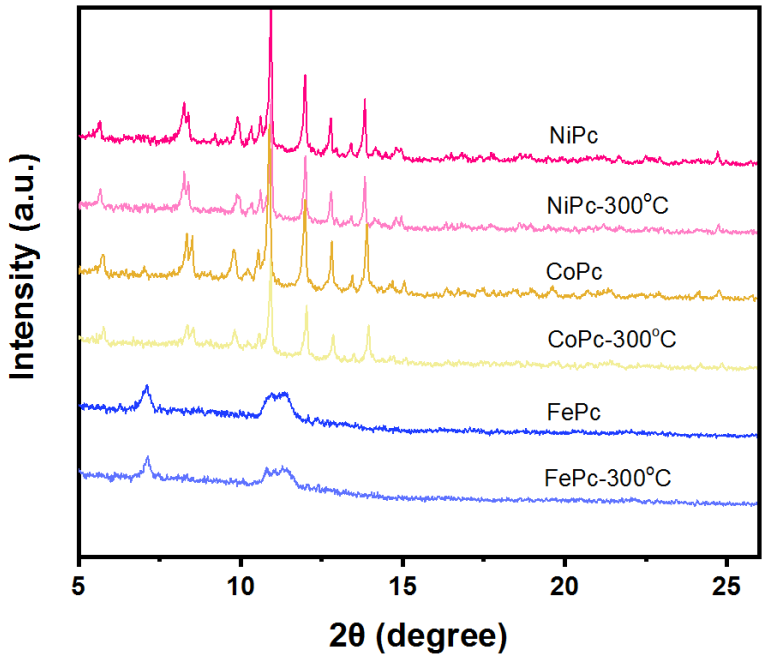

Figure S11. PXRD patterns of bare NiPc, CoPc and FePc before and after pyrolysis at 300 °C.

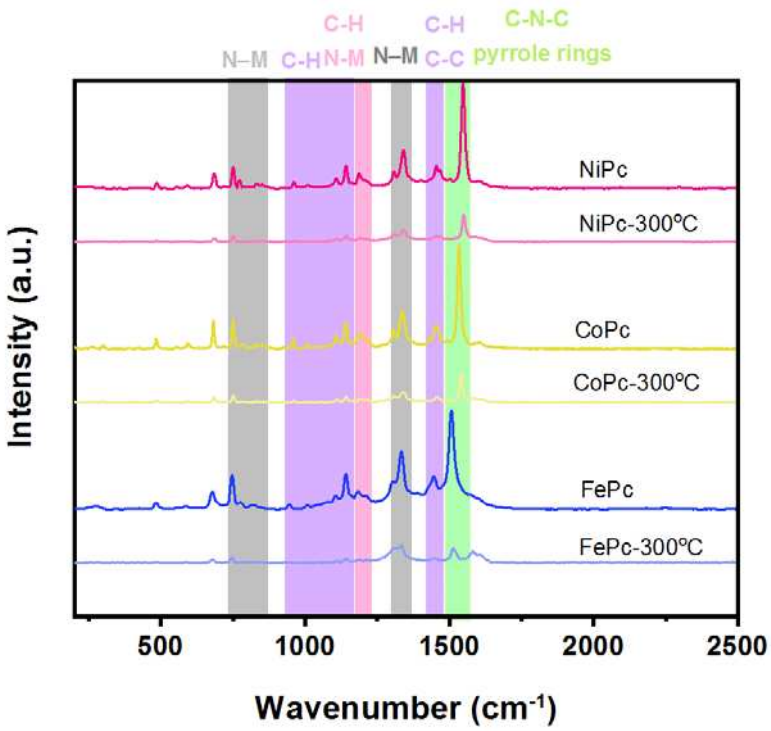

Figure S12. Raman spectra of bare NiPc, CoPc and FePc before and after pyrolysis at 300 °C.

The bands in the range of 1500-1560 cm^{-1} involve stretching of the C–N–C bonds as well as expansion of the pyrrole rings coupled with C–H vibrations. The bands in the range of 1420-1470 cm^{-1} are ascribed to C–H bond vibrations coupled with the stretching of C–C bonds. The bands in the range of 1300-1350 cm^{-1} arise from the stretching vibrations of isoindoles and N–M bonds. The peaks among 1170-1220 cm^{-1} are contributed from C–H and N–M bonds. The peaks around 930-1160 cm^{-1} are from C–H bonds. The signals around 730-870 cm^{-1} arise from the N-M bonds. The signal around 680 cm^{-1} can be associated with IPB of C–N–C bonds and expansion of isoindole moieties.

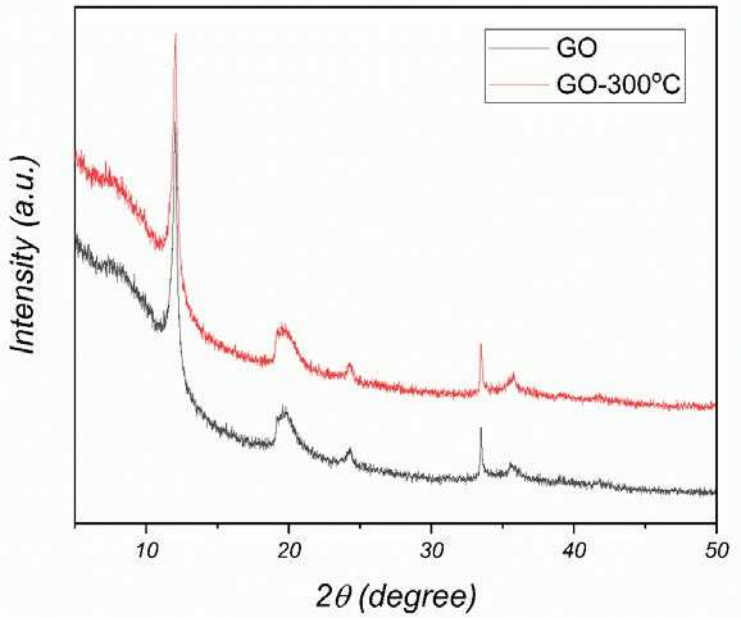

Figure S13. PXRD patterns of GO before and after pyrolysis at 300 °C.

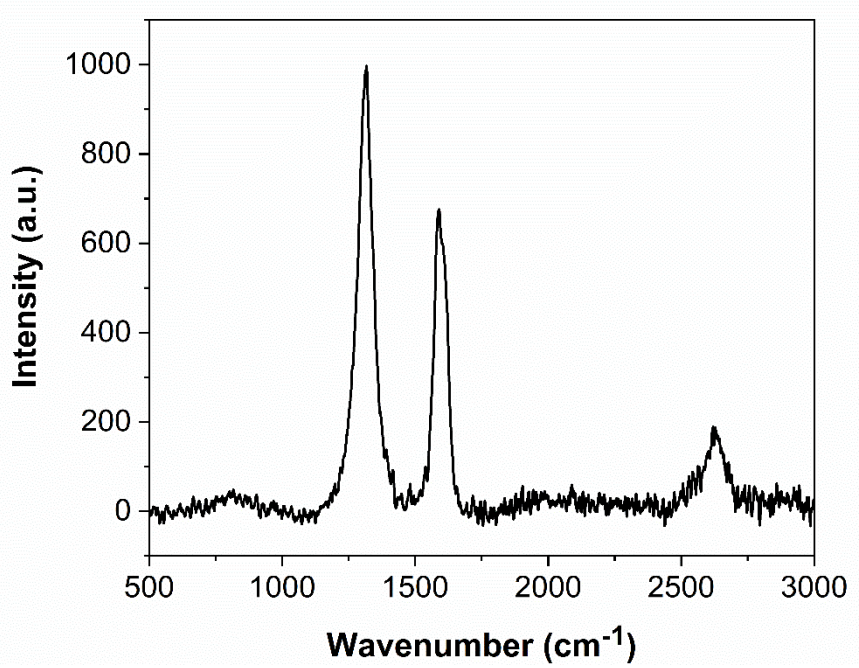

Figure S14. Raman spectrum of GO after pyrolysis at 300 °C in Ar atmosphere.

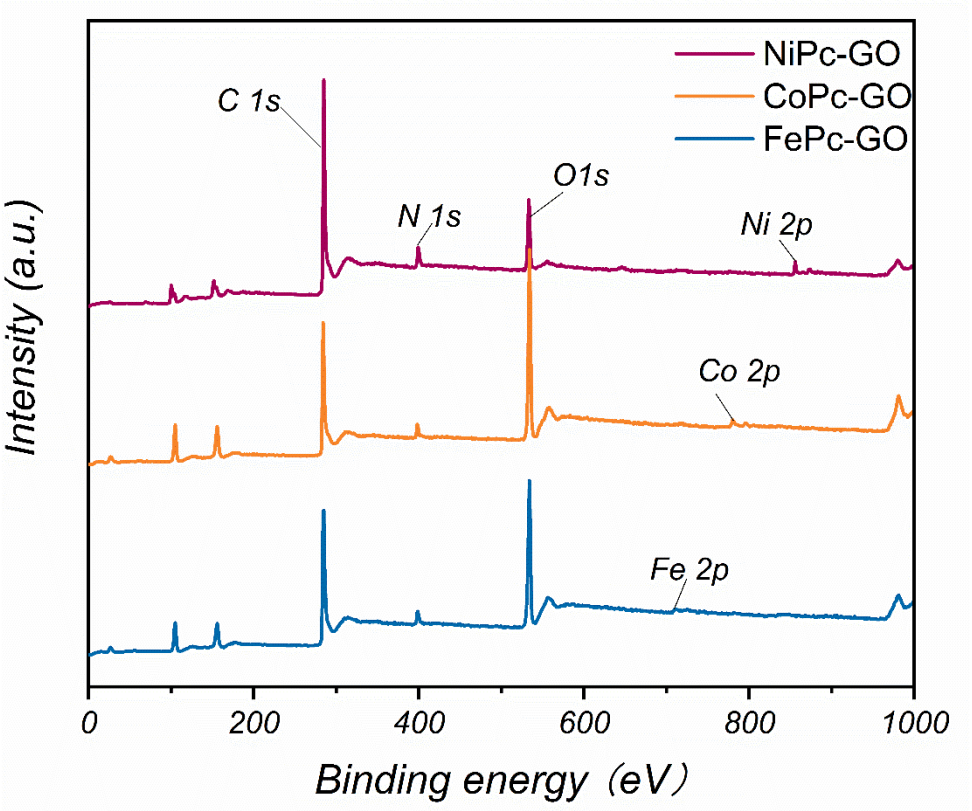

Figure S15. Complete XPS spectra of NiPc-GO, CoPc-GO and FePc-GO.

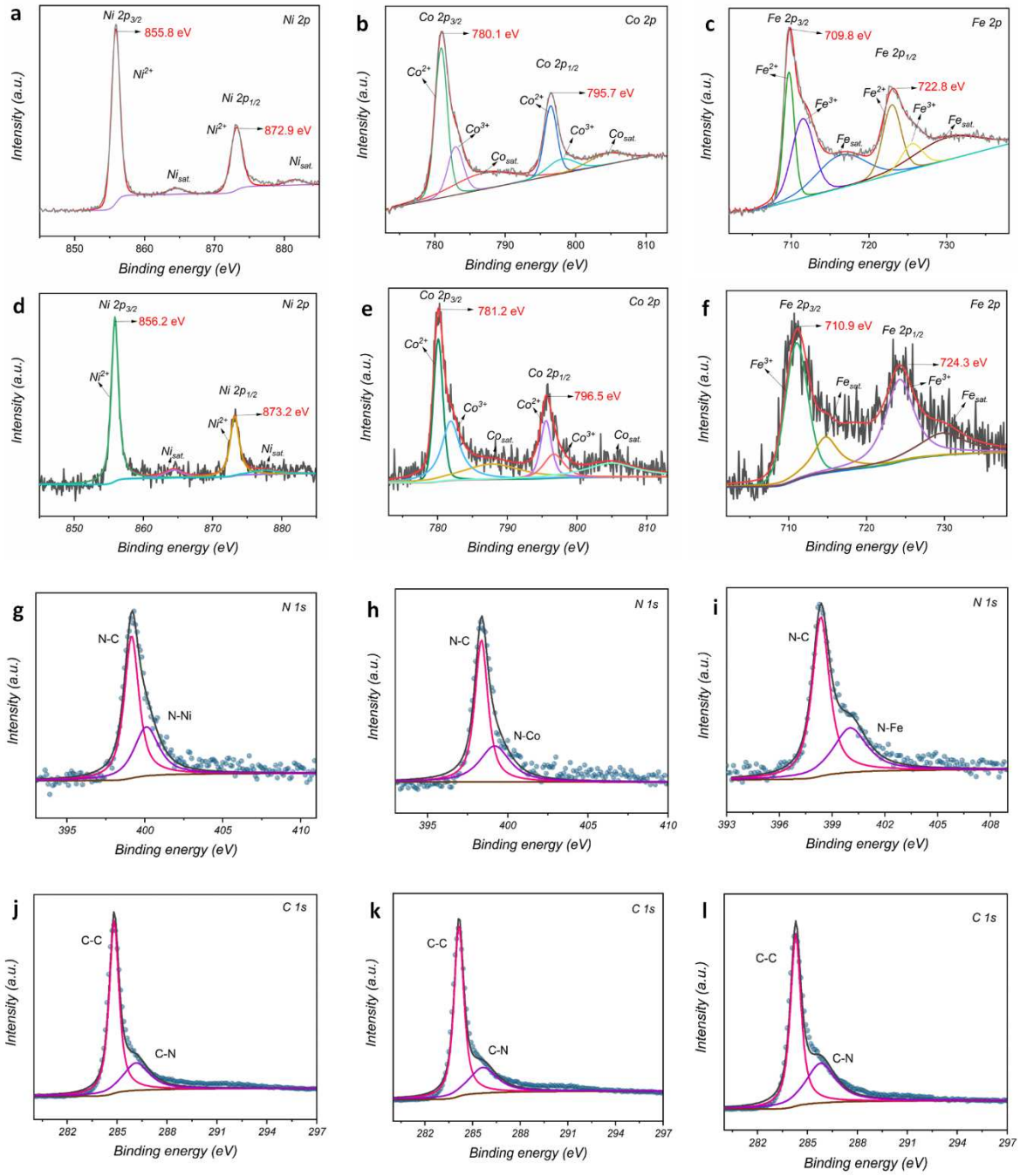

Figure S16. High resolution XPS spectra of (a) NiPc, (b) CoPc, (c) FePc, (d, g, j) NiPc-GO, (e, h, k) CoPc-GO and (f, i, l) FePc-GO.

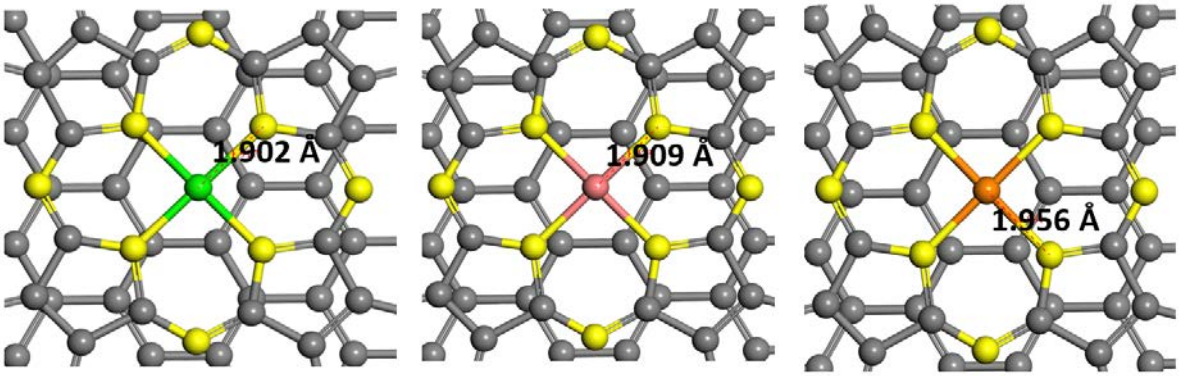

Figure S17. Structure of NiPc-GO (left), CoPc-GO (middle) and FePc-GO (right).

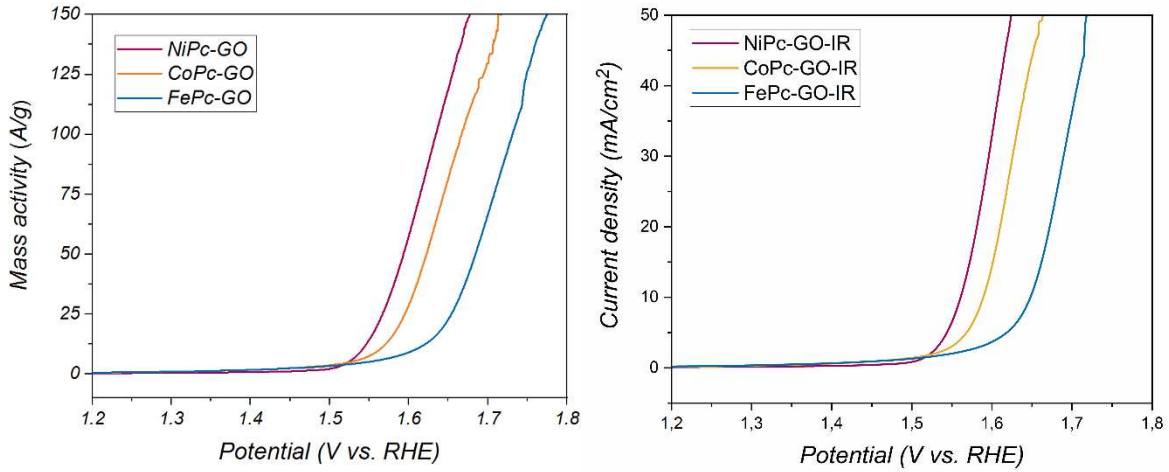

Figure S18. OER performances of NiPc-GO, CoPc-GO and FePc-GO normalized to mass activity (left) and iR-correction (right).

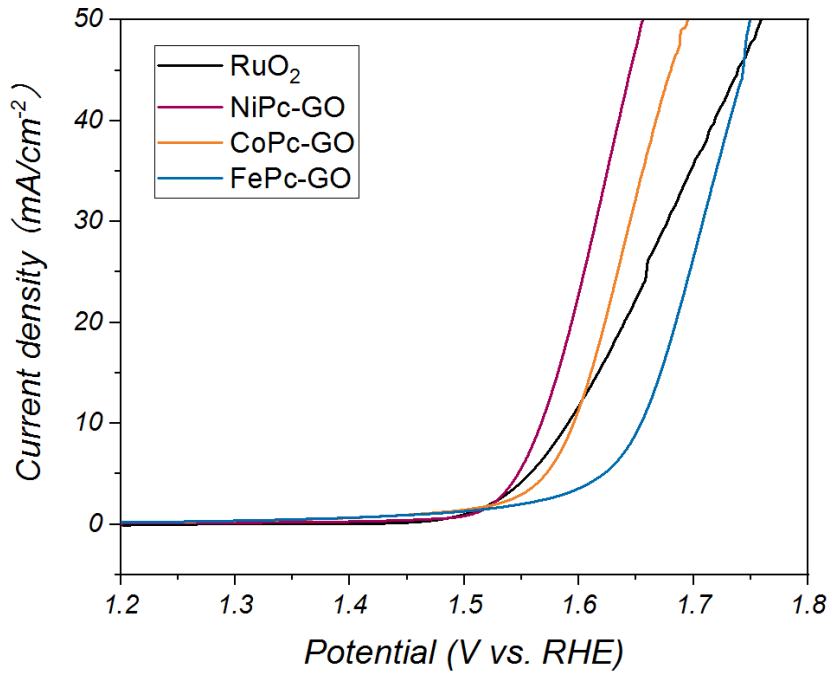

Figure S19. Electrocatalytic OER performance of RuO_2, NiPc-GO, CoPc-GO and FePc-GO.

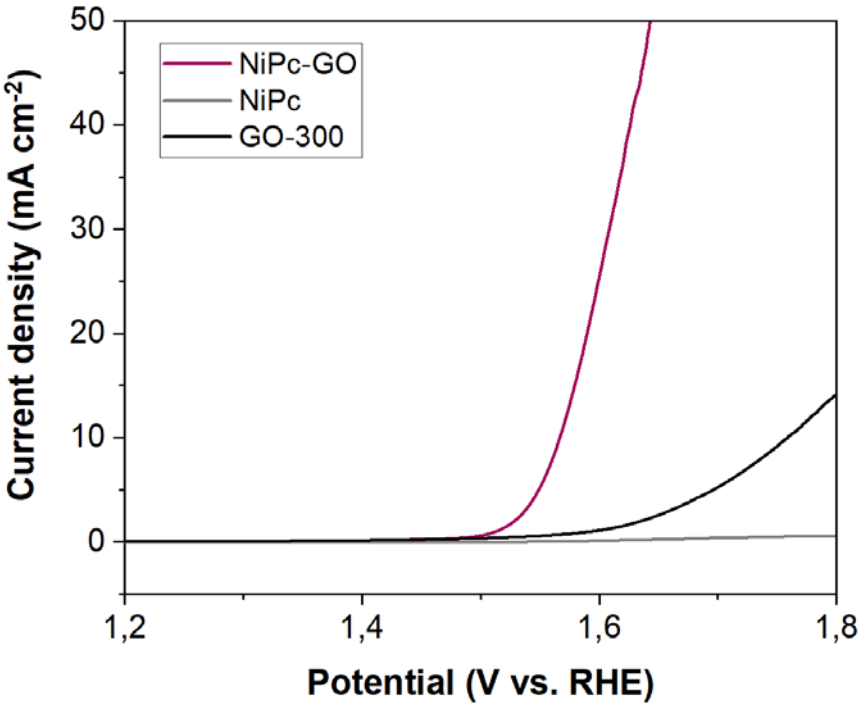

Figure S20. Electrocatalytic OER performance of NiPc-GO, GO-300 and NiPc.

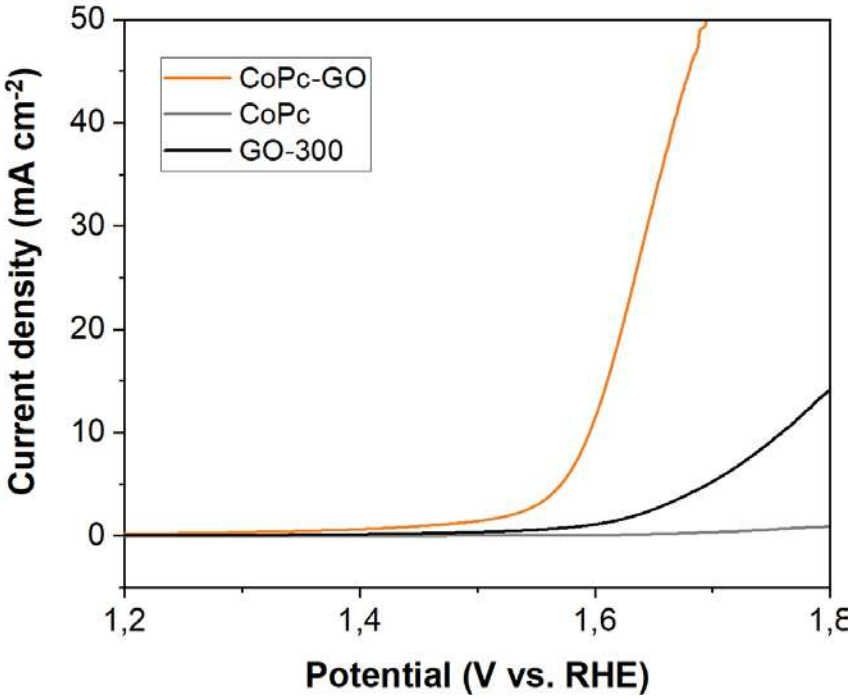

Figure S21. Electrocatalytic OER performance of CoPc-GO, GO-300 and CoPc.

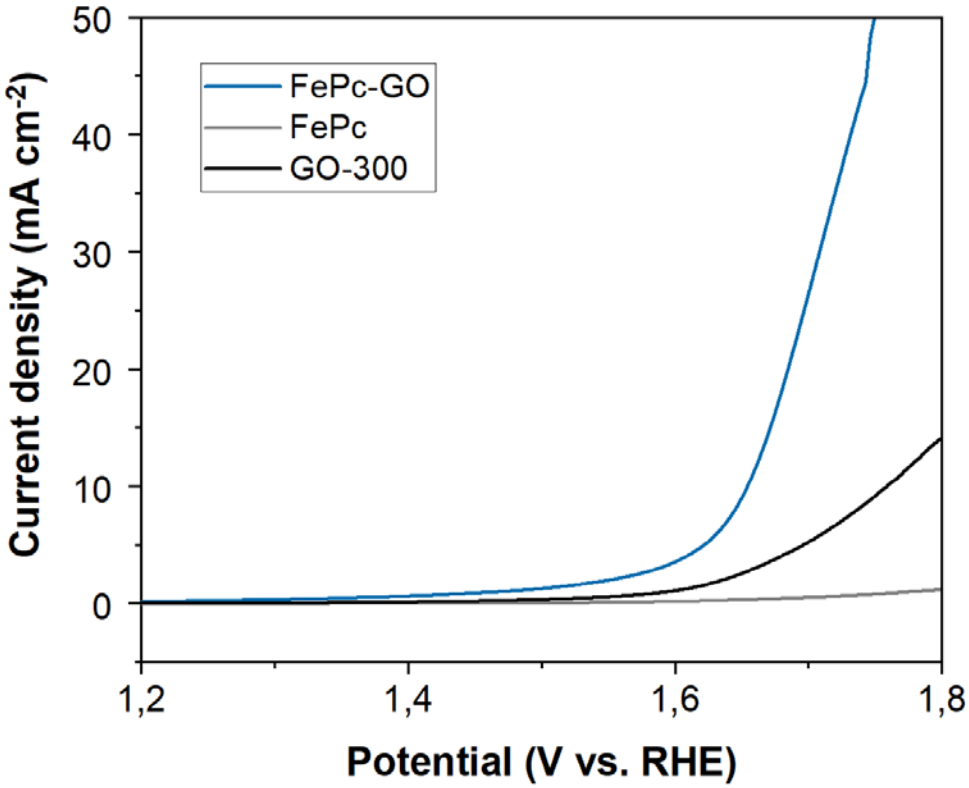

Figure S22. Electrocatalytic OER performance of FePc-GO, GO-300 and FePc.

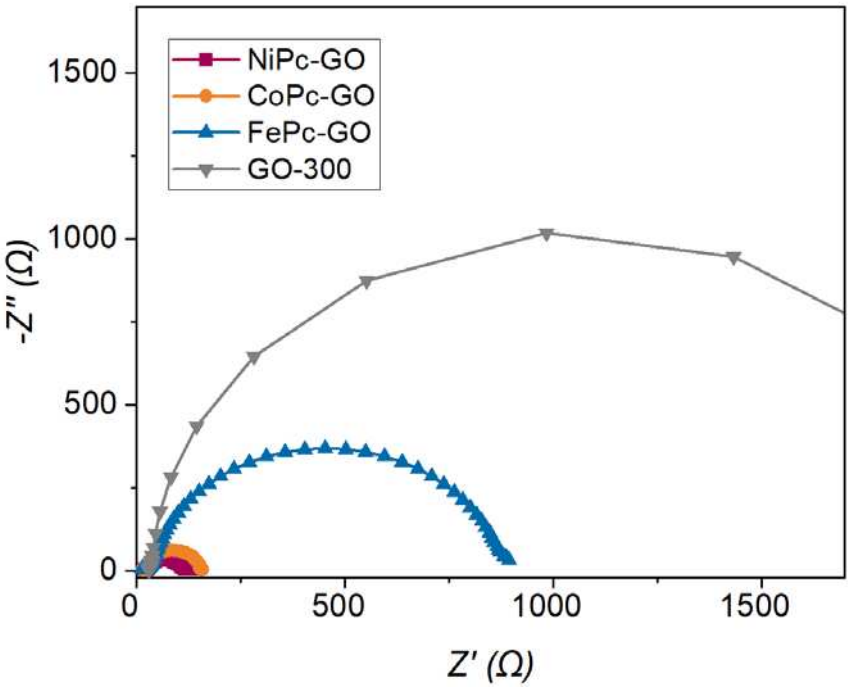

Figure S23. EIS measurements of NiPc-GO, CoPc-GO and FePc-GO and G-300 at 1.5 V *vs.* RHE.

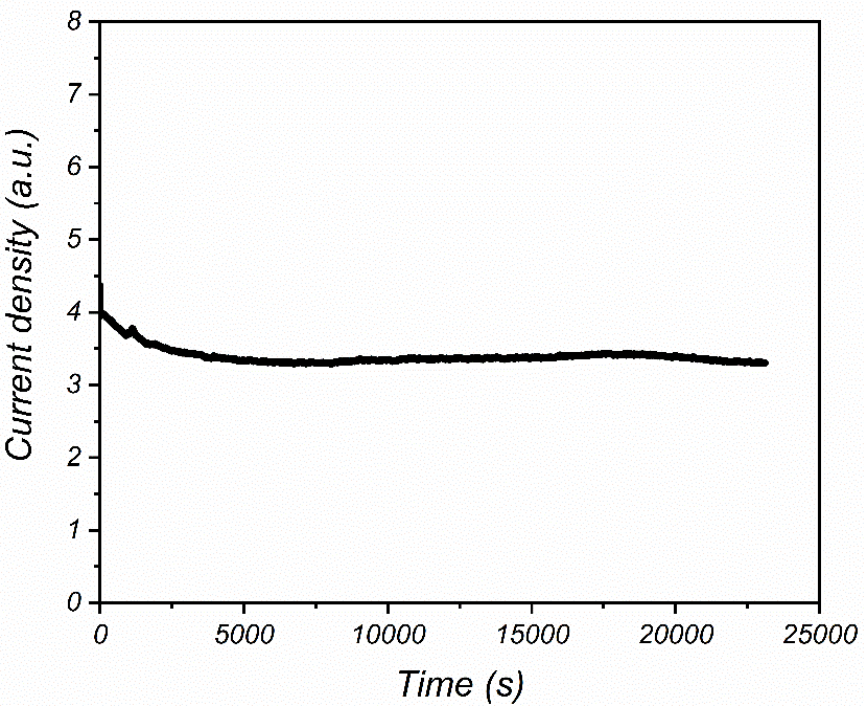

Figure S24. Long-term chronoamperometric OER test of bare Ni foam.

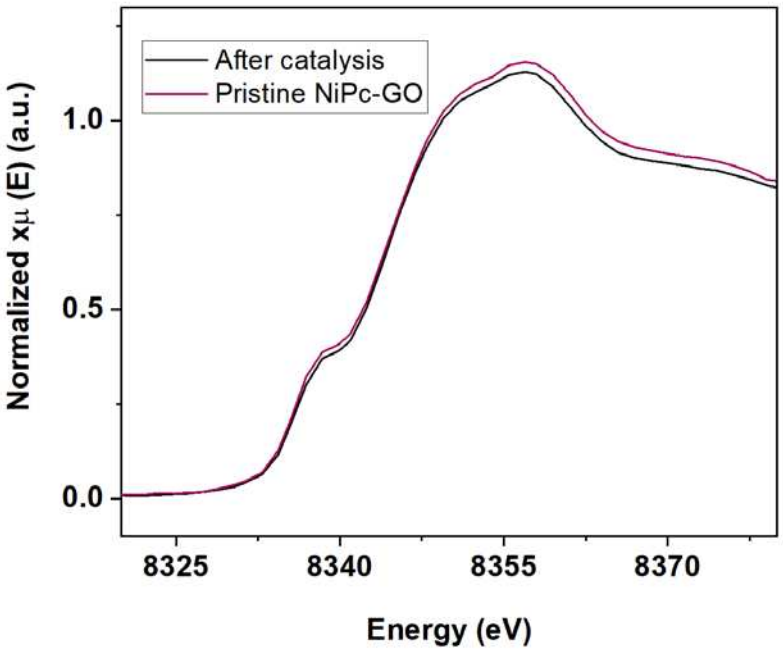

Figure S25. Ni *K*-edge XANES spectra of NiPc-GO before and after OER.

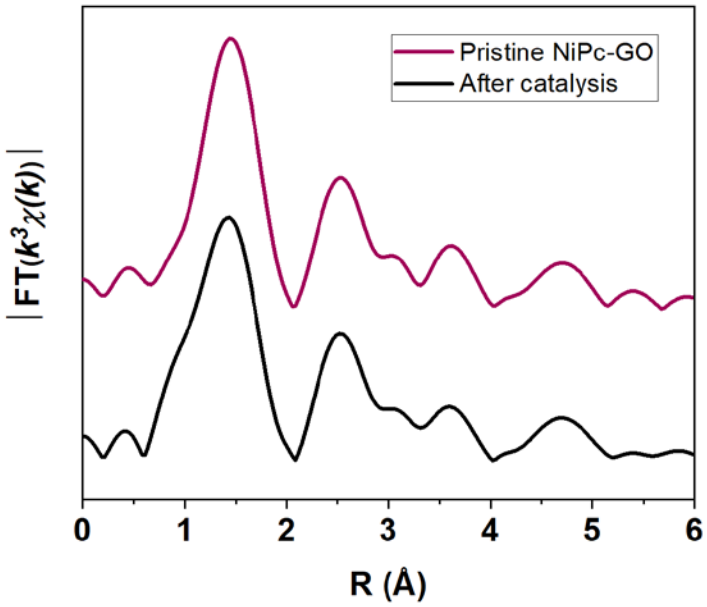

Figure S26. Fourier-transform of the *K*-edge EXAFS spectra of NiPc-GO before and after OER.

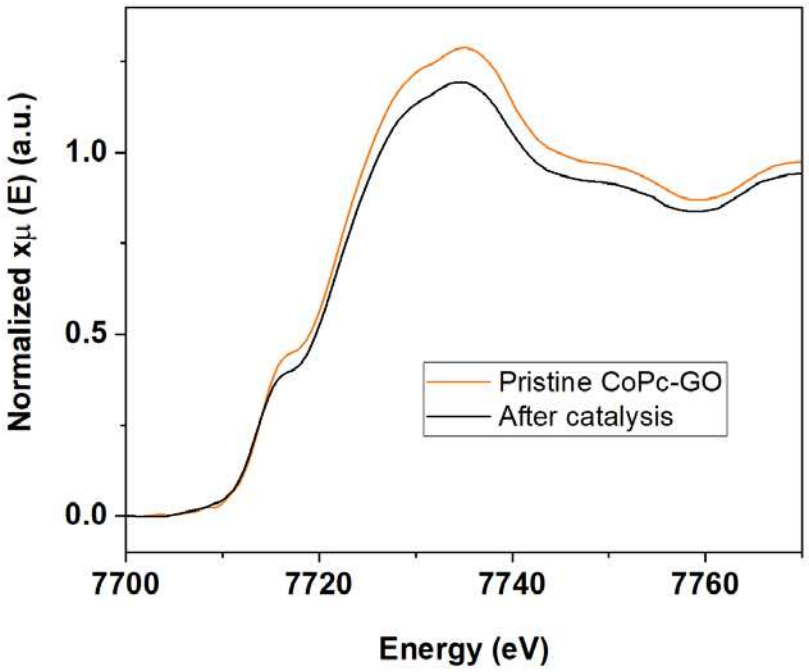

Figure S27. Co *K*-edges XANES spectra of CoPc-GO before and after OER.

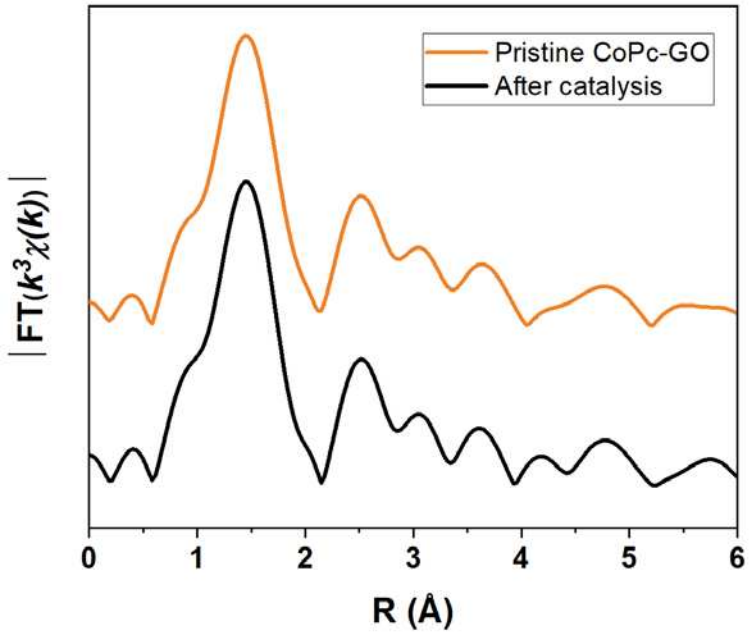

Figure S28. Fourier-transform of the Co *K*-edge EXAFS spectra of CoPc-GO before and after OER.

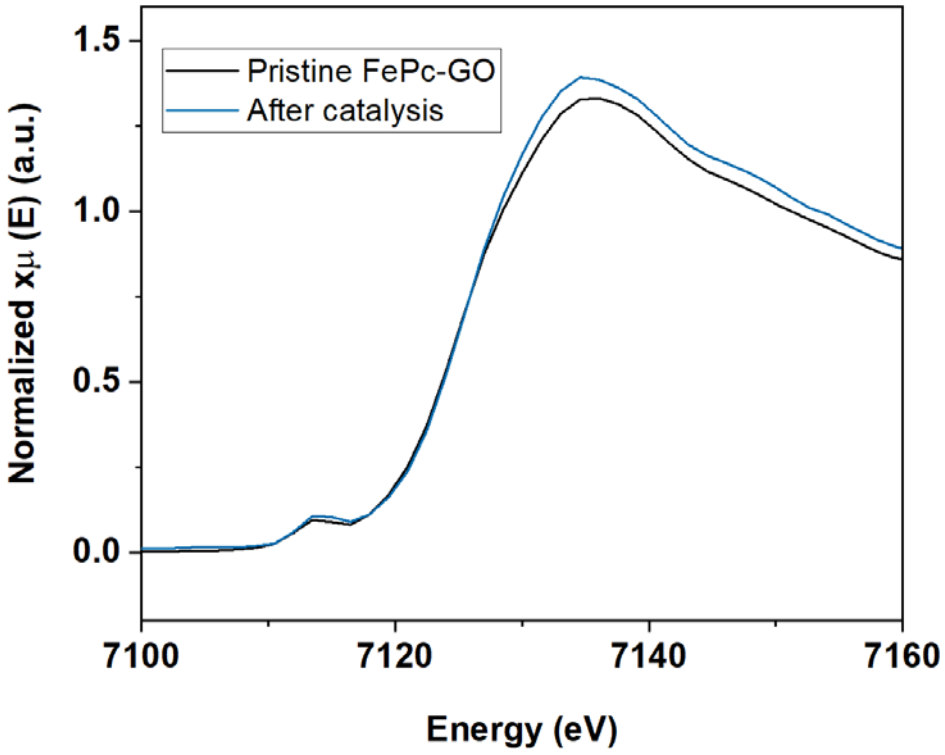

Figure S29. Fe *K*-edge XANES spectra of FePc-GO before and after OER.

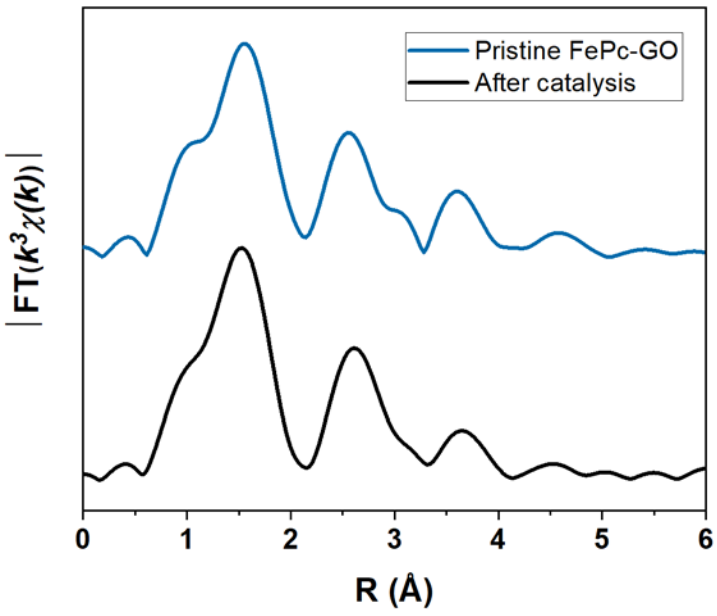

Figure S30. Fourier-transform of the Fe *K*-edge EXAFS spectra of FePc-GO before and after OER.

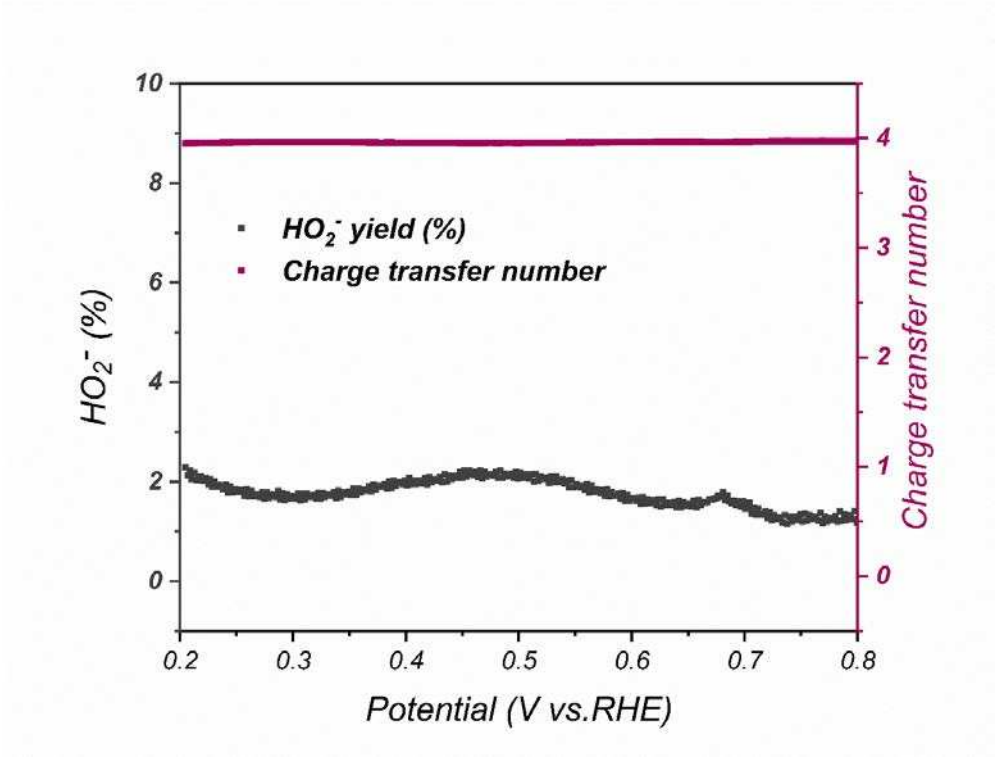

Figure 31. HO_2^- % yield for ORR and the number of transfer electrons measured by the RRDE method.

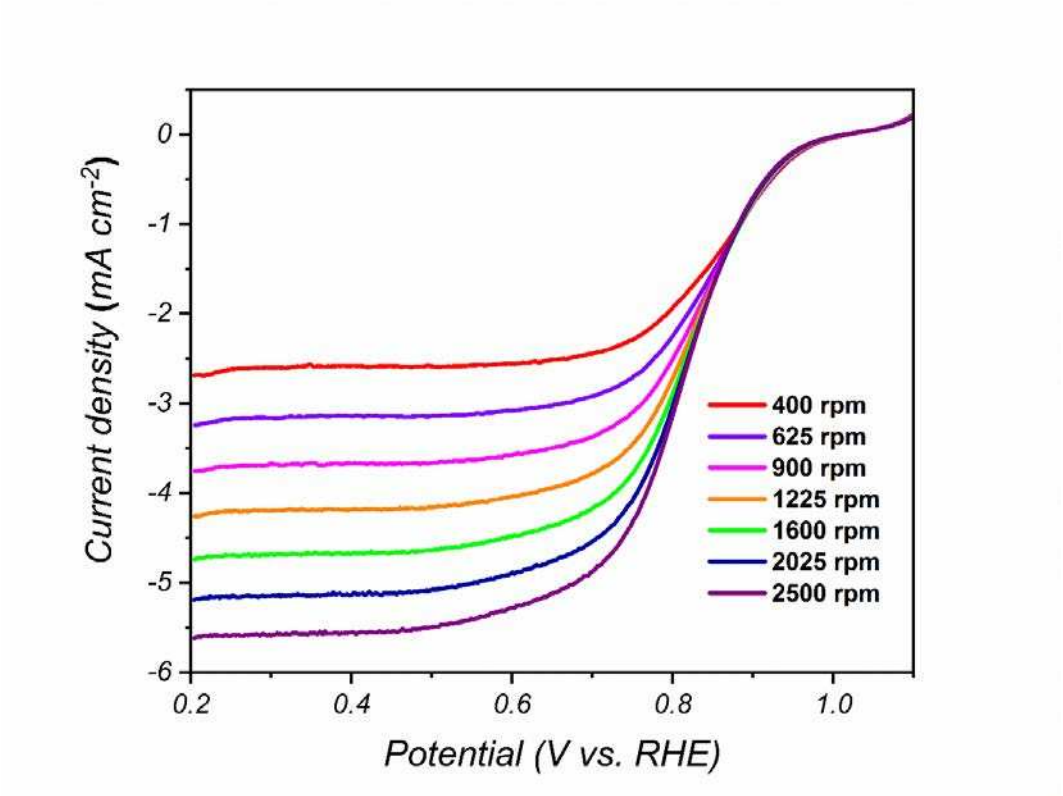

Figure S32. LSV curves of Pt/C with a scan rate of 10 mV s^{-1} at different rotation rates.

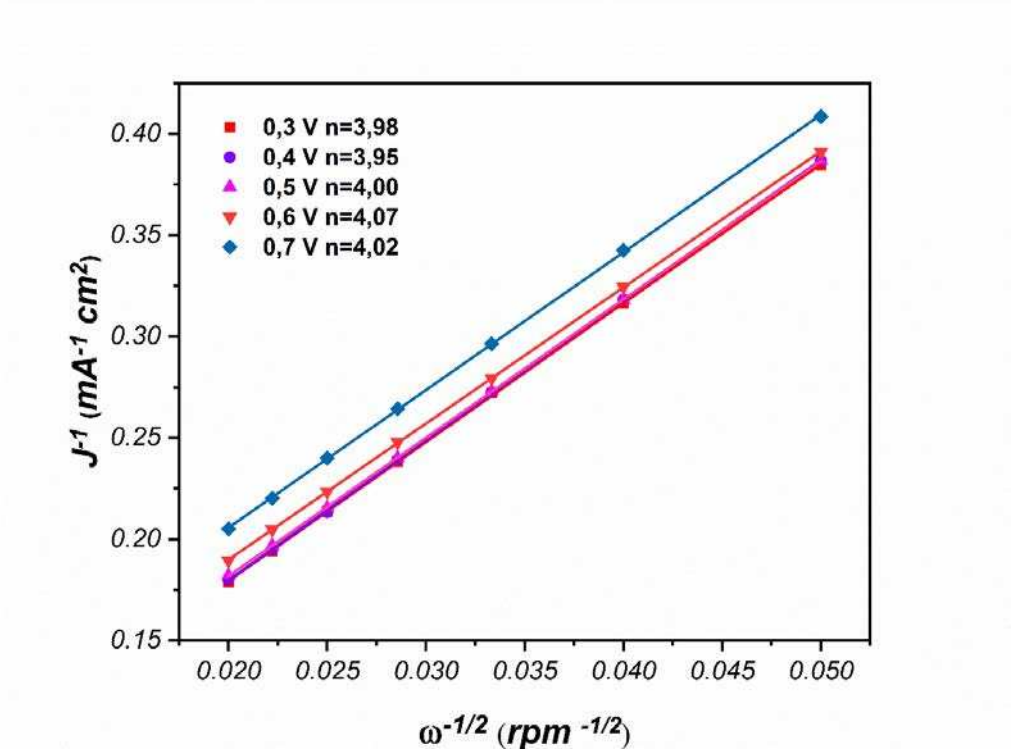

Figure 33. Koutecky–Levich (K–L) plots of Pt/C.

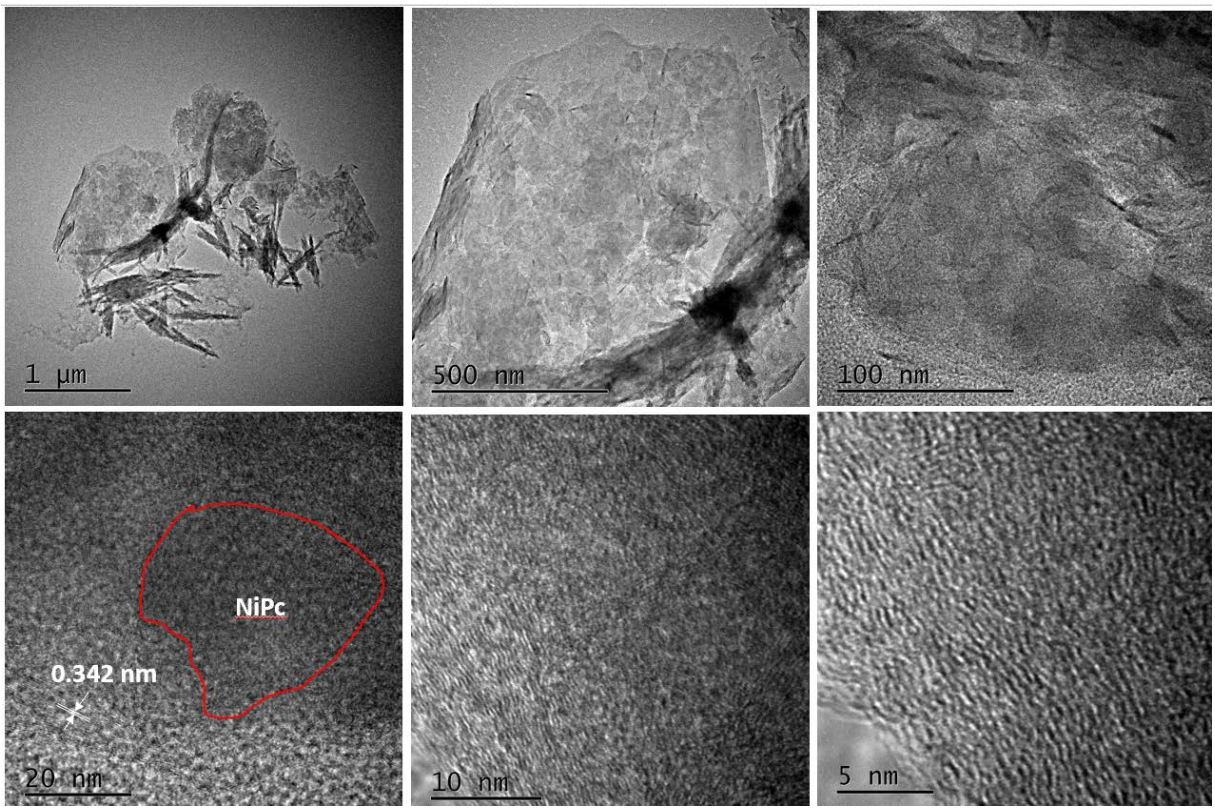

Figure S34. Position 1: HRTEM of NiPc-GO after OER with different magnifications.

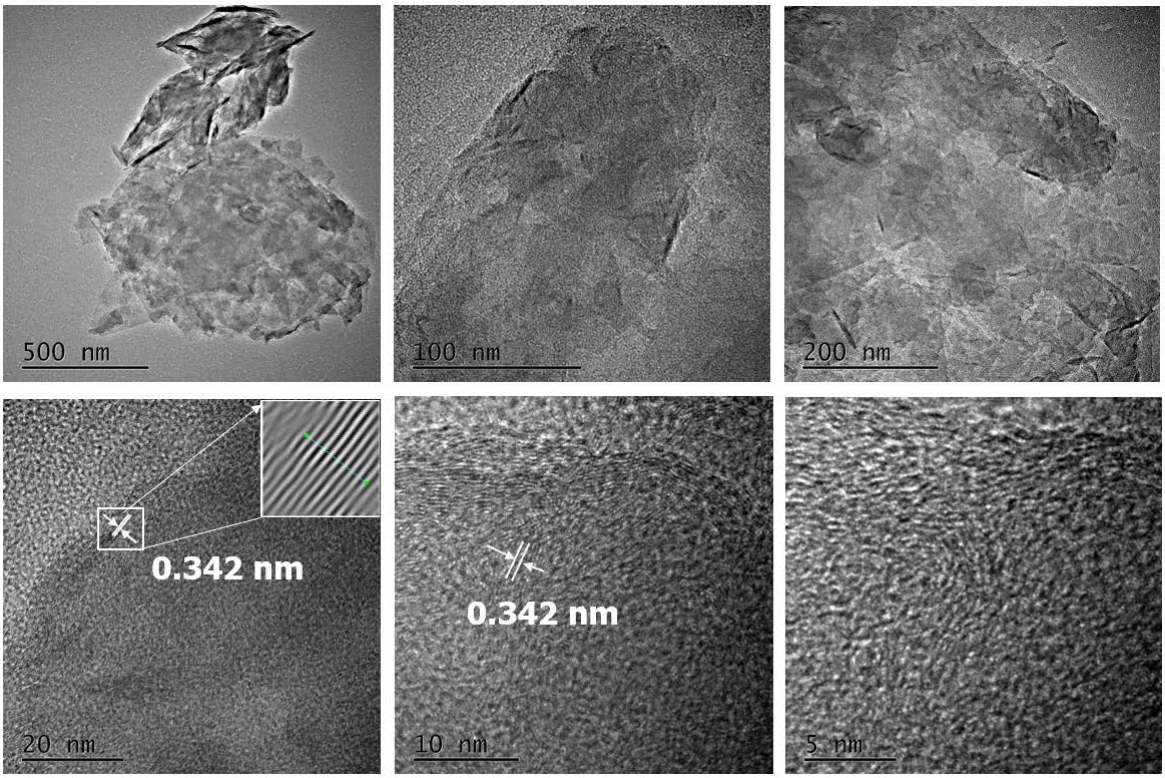

Figure S35. Position 2: HRTEM of NiPc-GO after OER with different magnifications.

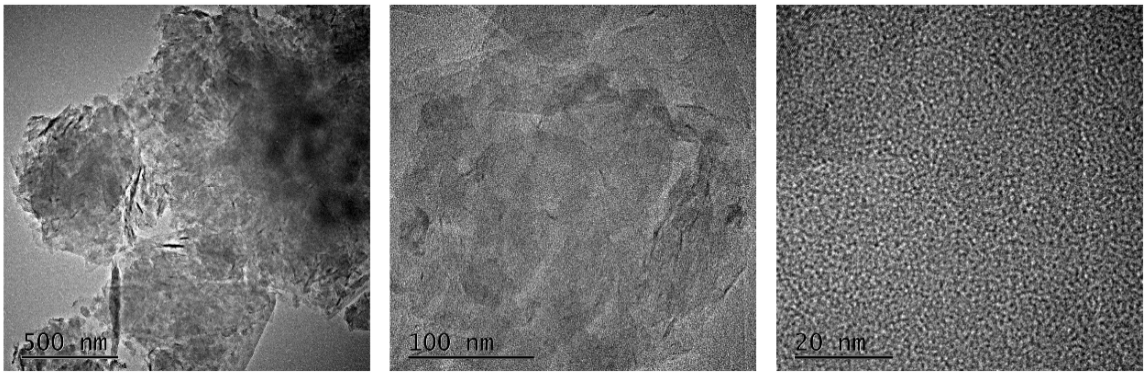

Figure S36. Position 3: HRTEM of NiPc-GO after OER with different magnifications.

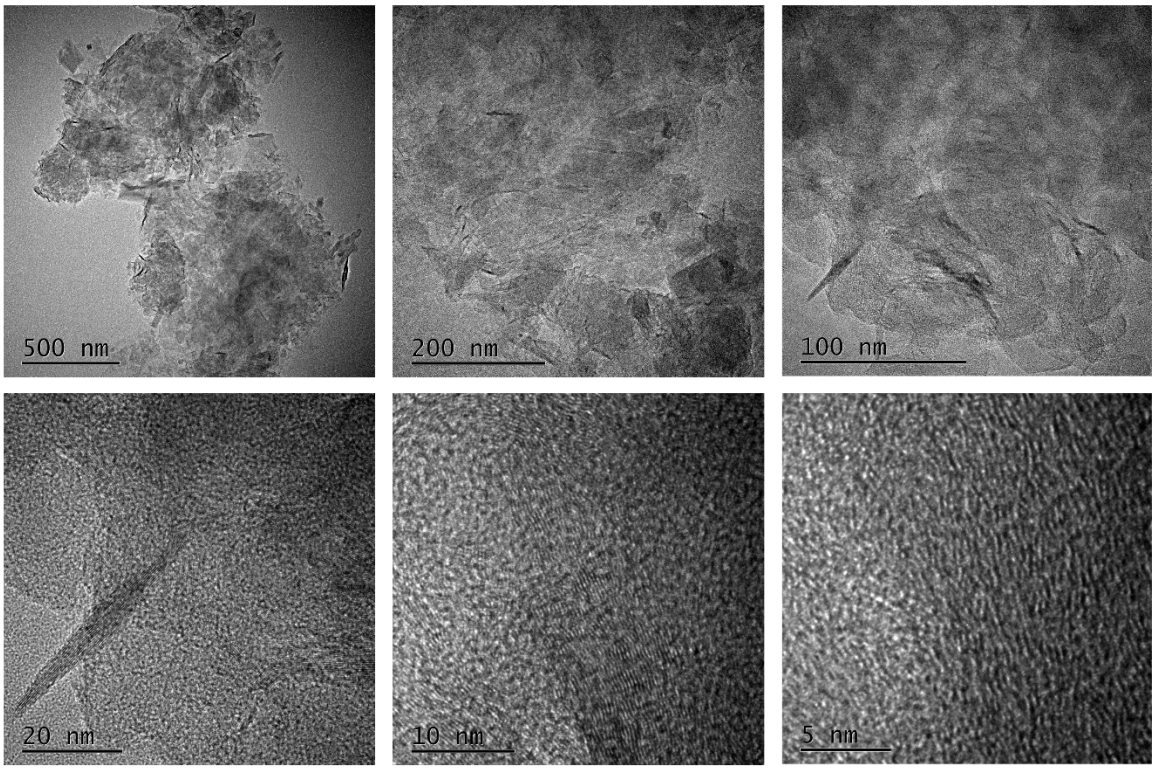

Figure S37. Position 1: HRTEM of CoPc-GO after OER with different magnifications.

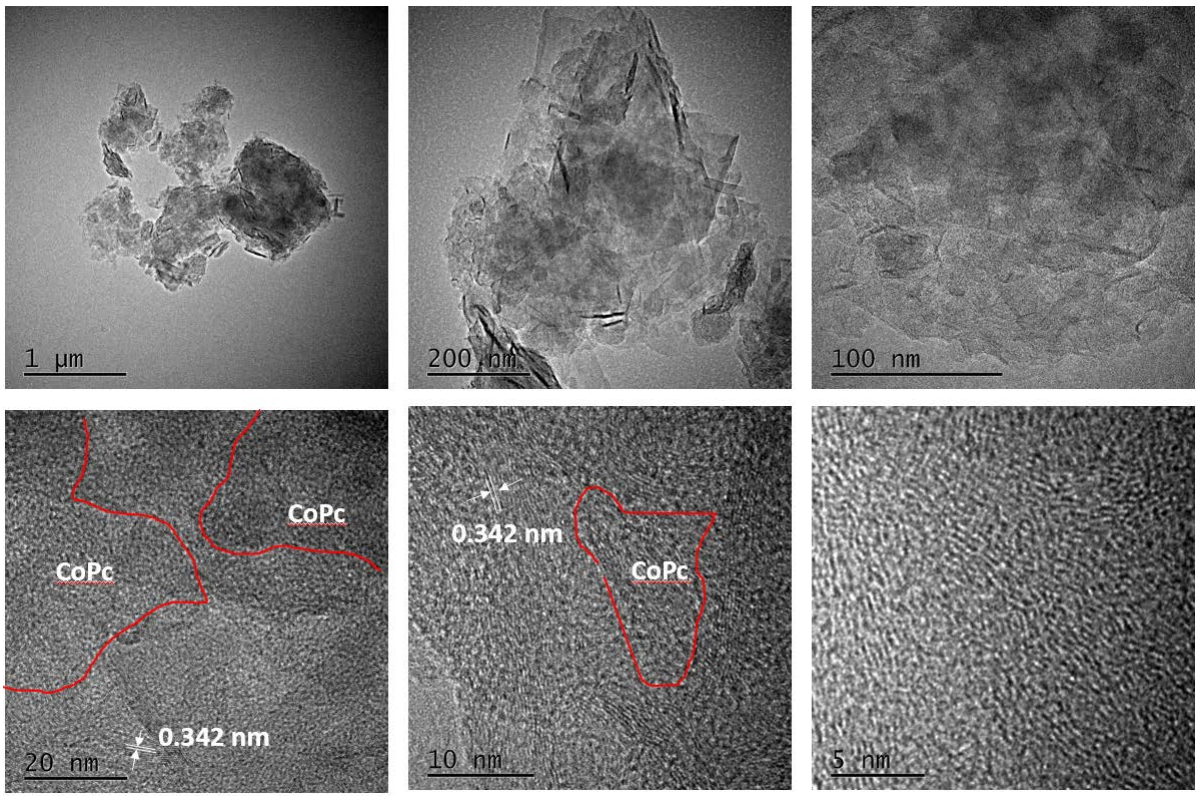

Figure S38. Position 2: HRTEM of CoPc-GO after OER with different magnifications.

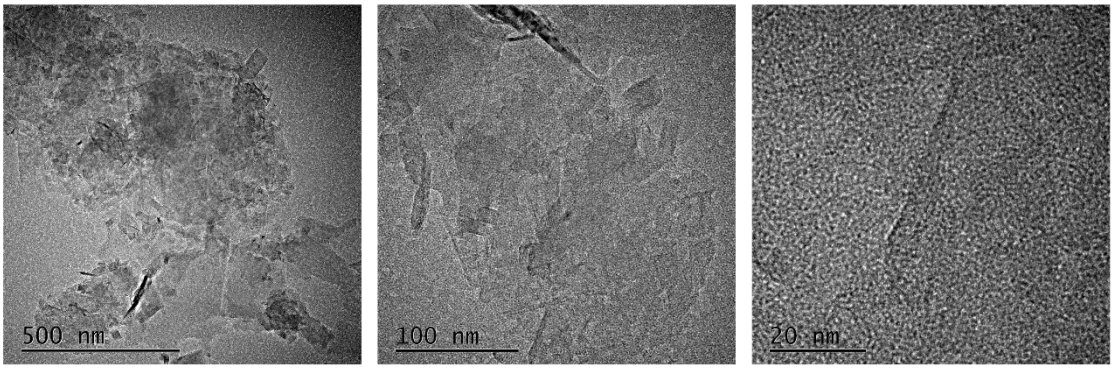

Figure S39. Position 3: HRTEM of CoPc-GO after OER with different magnifications.

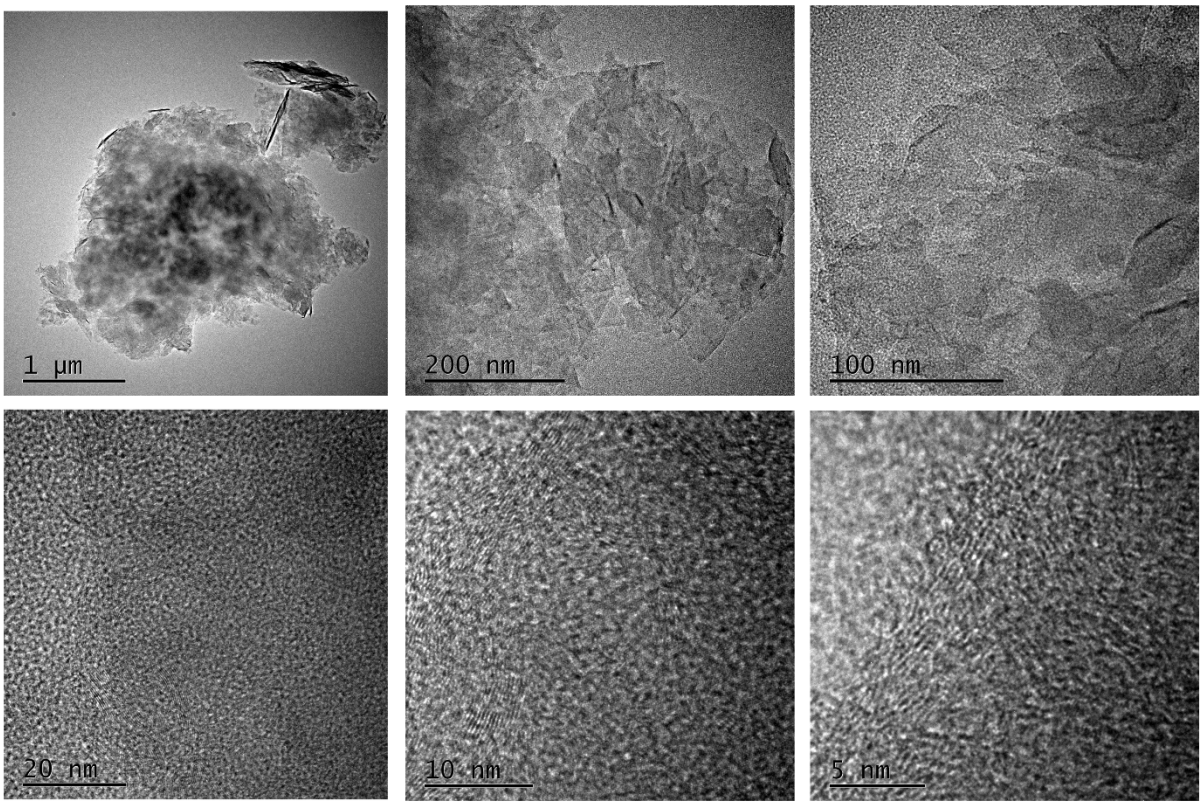

Figure S40. Position 1: HRTEM of FePc-GO after OER with different magnifications.

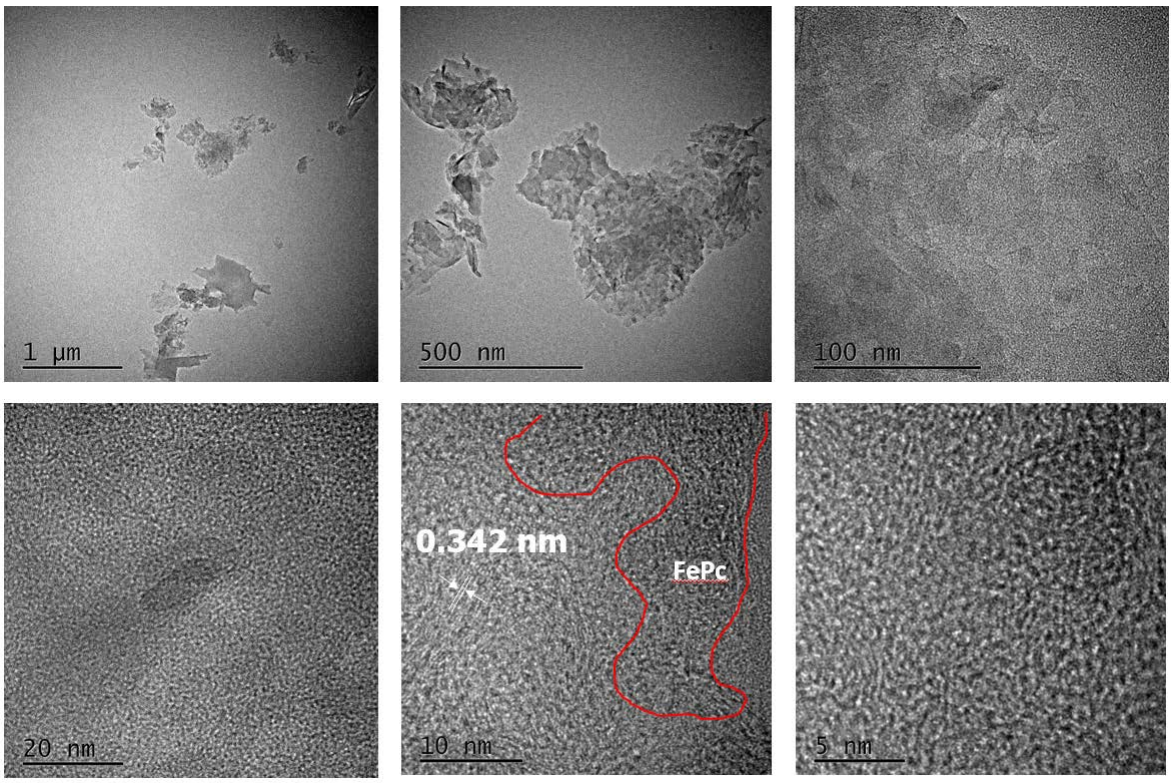

Figure S41. Position 2: HRTEM of FePc-GO after OER with different magnifications.

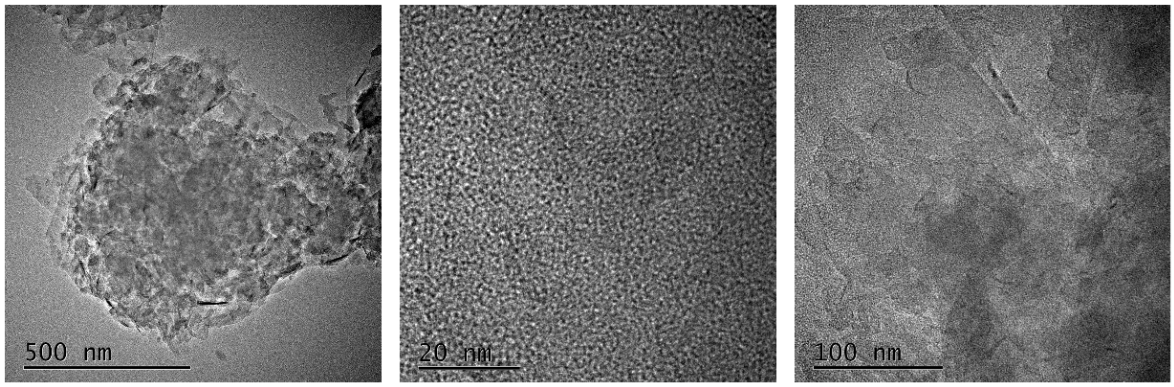

Figure S42. Position 3: HRTEM of FePc-GO after OER with different magnifications.

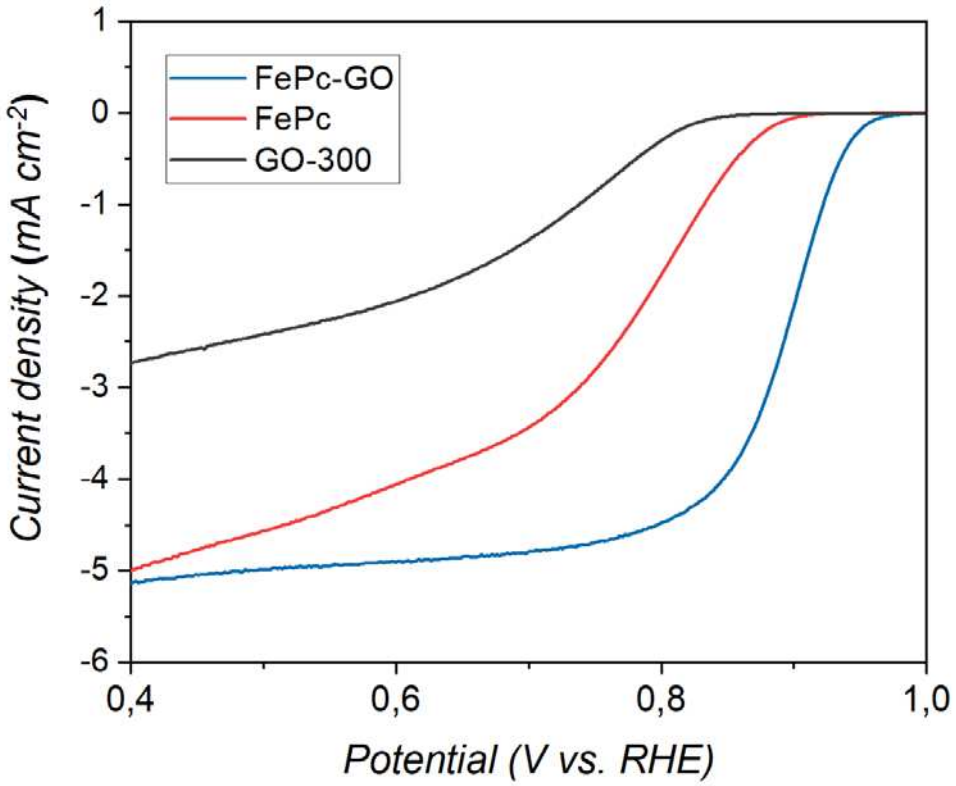

Figure S43. ORR LSV curves in 0.1 M oxygen-saturated KOH solution for FePc-GO, FePc and GO-300.

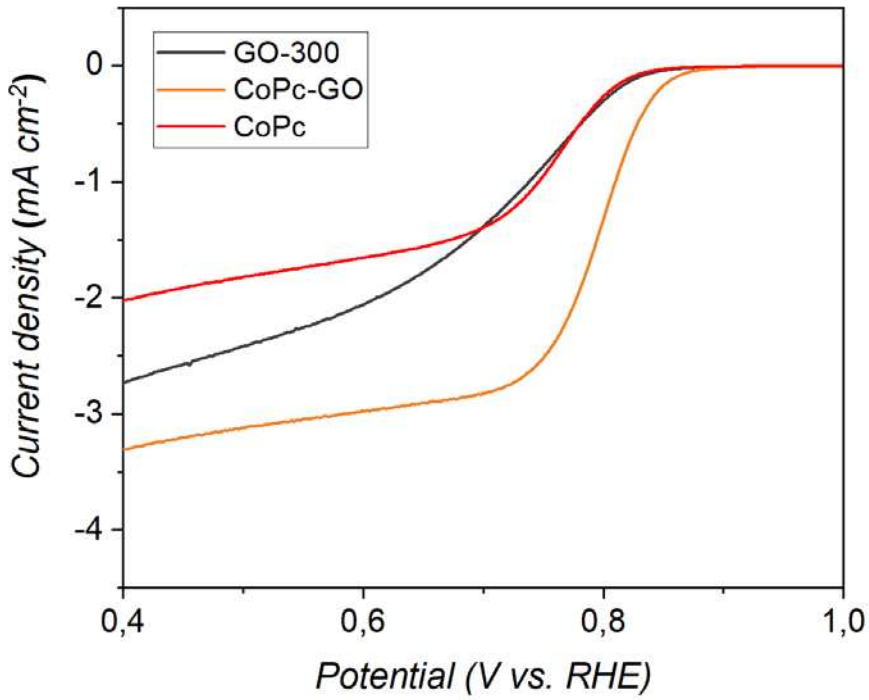

Figure S44. ORR LSV curves in 0.1 M oxygen-saturated KOH solution for CoPc-GO, CoPc and GO-300.

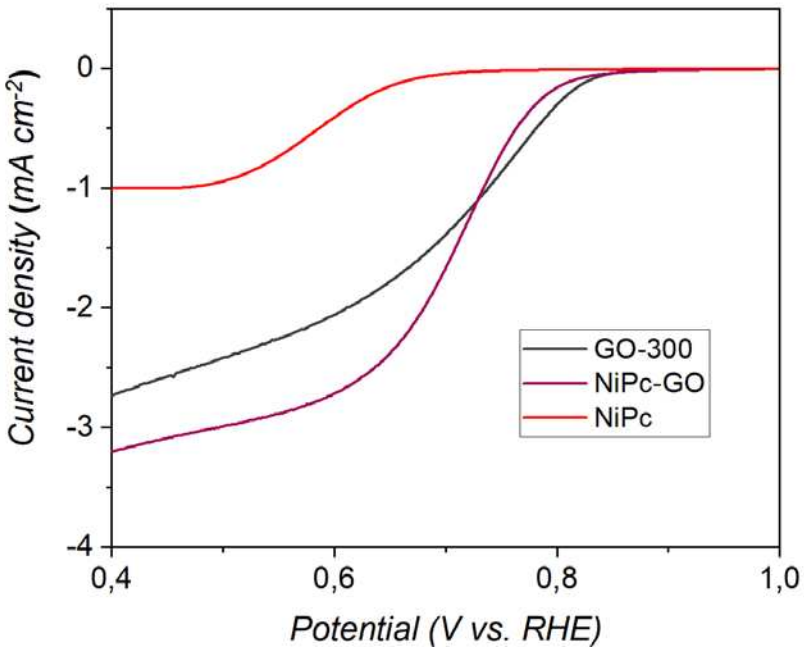

Figure S45. ORR LSV curves in 0.1 M oxygen-saturated KOH solution for NiPc-GO, NiPc and GO-300.

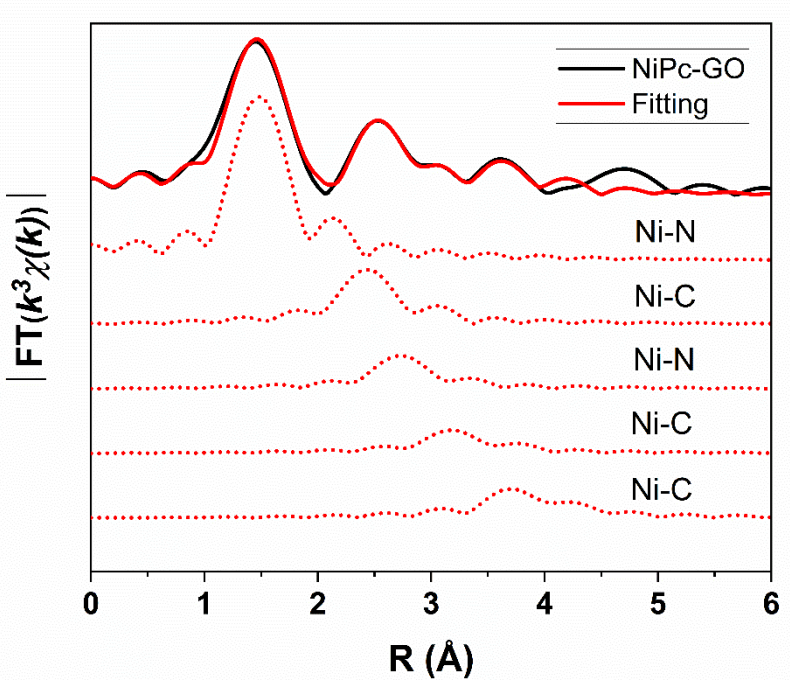

Figure S46. Fitting of the experimental Ni *K*-edge EXAFS spectrum $|\mathrm{FT}(k^3\chi(k))|$ of NiPc-GO and the corresponding fitted single scattering paths.

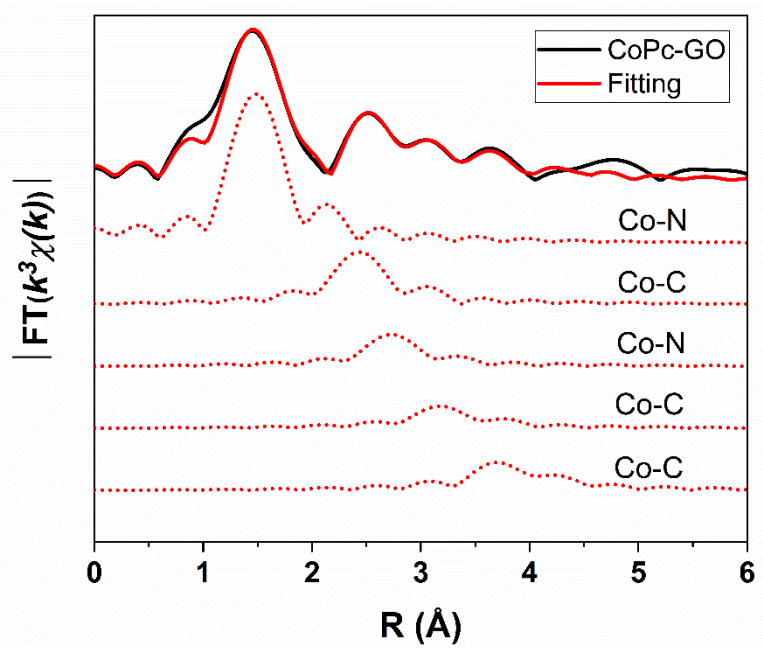

Figure S47. Fitting of the experimental Co *K*-edge EXAFS spectrum $|\mathrm{FT}(k^3\chi(k))|$ of CoPc-GO and the corresponding fitted single scattering paths.

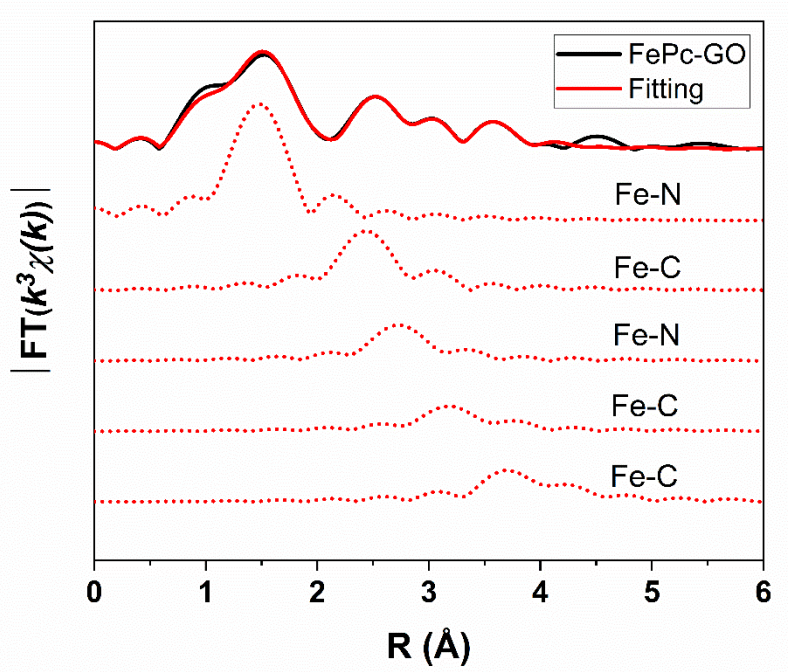

Figure S48. Fitting of the experimental Fe *K*-edge EXAFS spectrum $|\mathrm{FT}(k^3\chi(k))|$ of FePc-GO and the corresponding fitted single scattering paths.

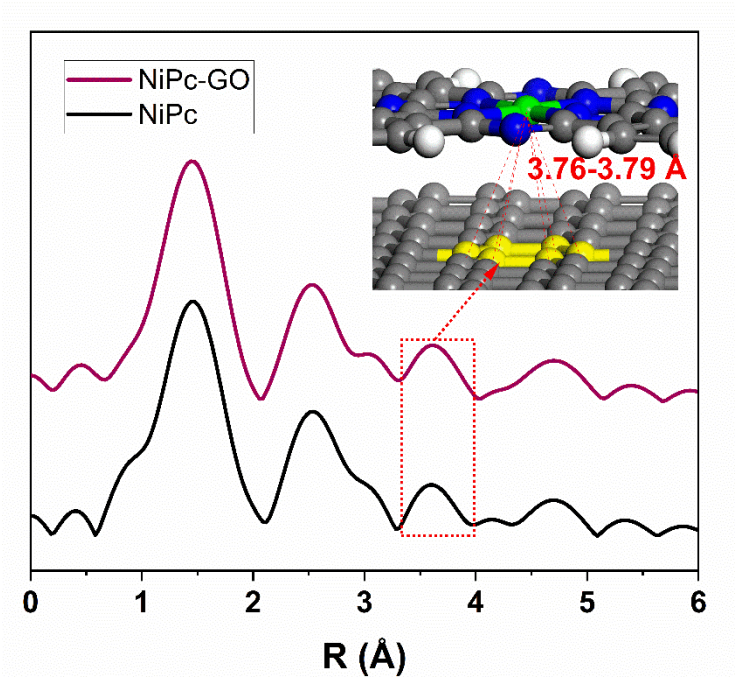

Figure S49. Fourier-transform magnitudes of the Ni *K*-edge EXAFS spectra of NiPc-GO, NiPc and DFT optimized structure (inset).

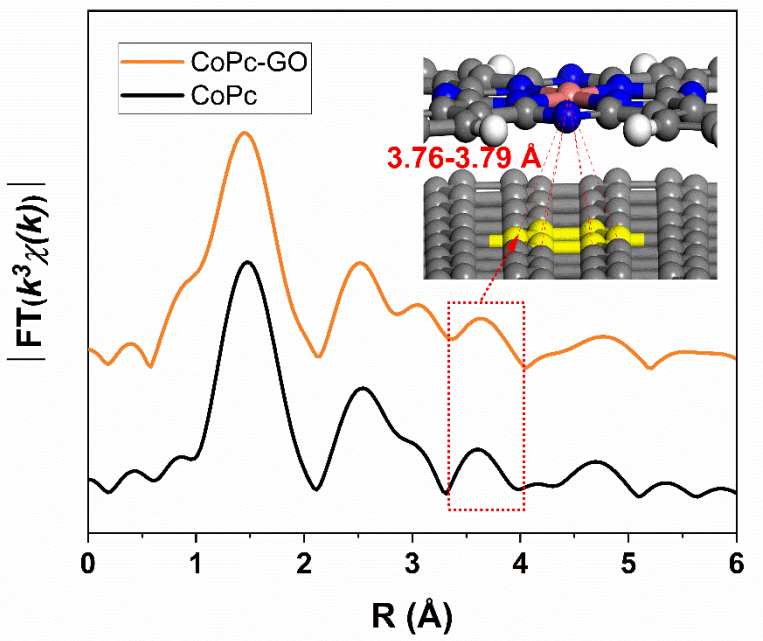

Figure S50. Fourier-transform magnitudes of the Co *K*-edge EXAFS spectra of CoPc-GO, CoPc and DFT optimized structure (inset).

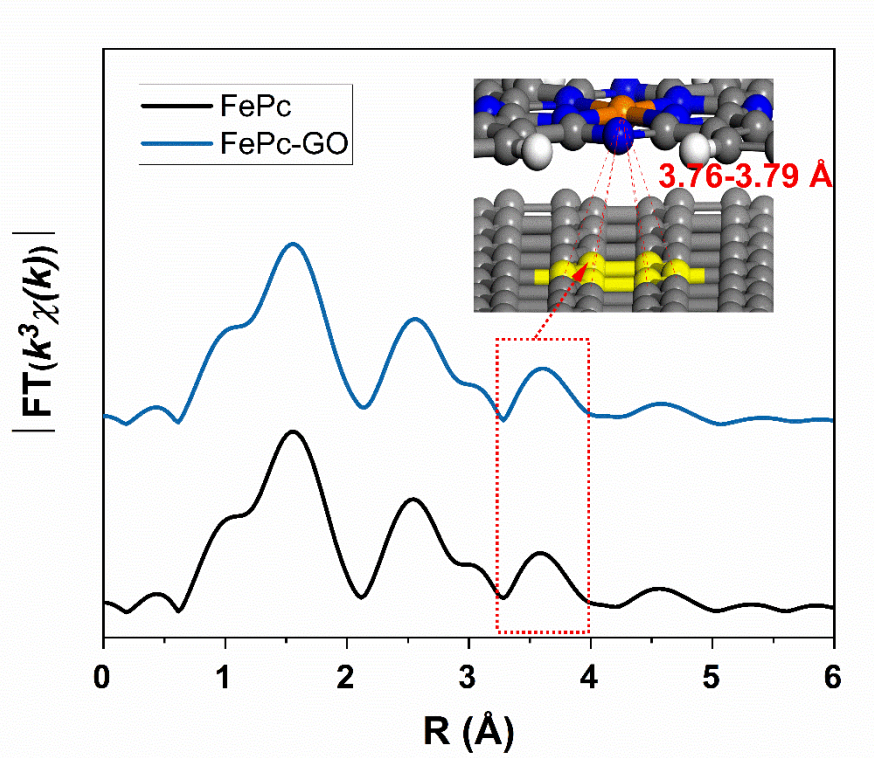

Figure S51. Fourier-transform magnitudes of the Fe *K*-edge EXAFS spectra of FePc-GO, FePc and DFT optimized structure (inset).

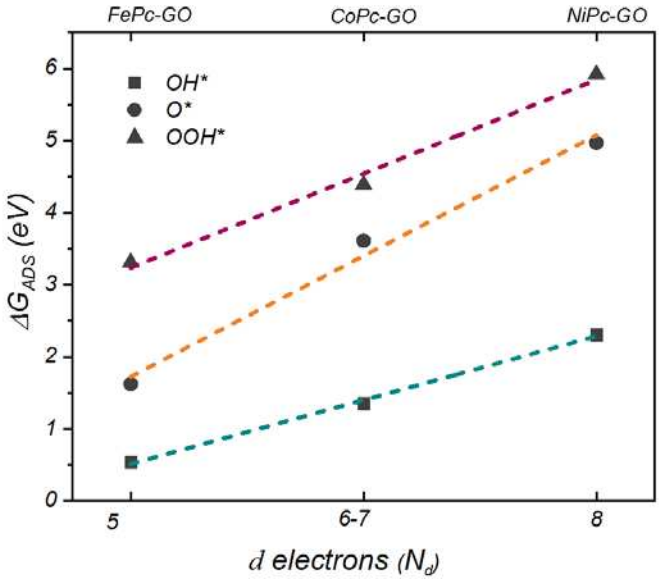

Figure S52. Relationship between the number of N_d and adsorption energies for the intermediates *OH, *O and *OOH. Due to the Fe^{3+} and slight Co^{3+} present in our samples, N_d (Fe) and N_d (Co) here are 5 and 6-7, respectively.

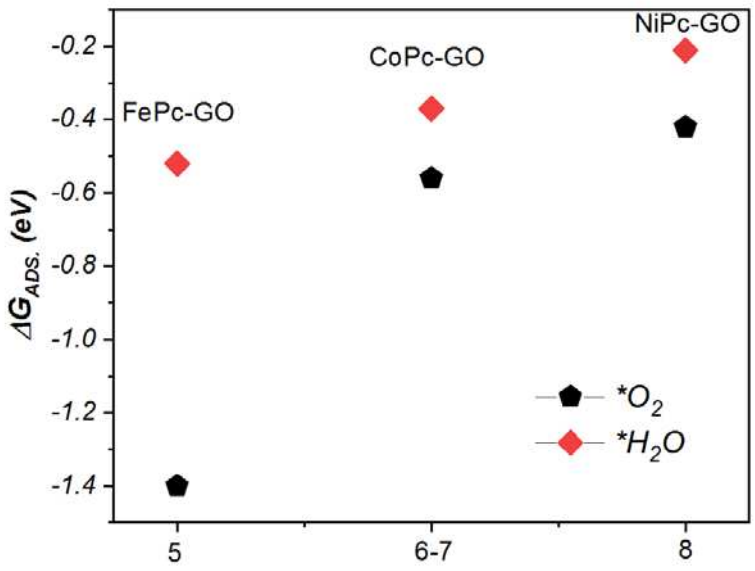

Figure S53. Relationship between the number of N_d and adsorption energies for the intermediates $*O_2$ and $*H_2O$.

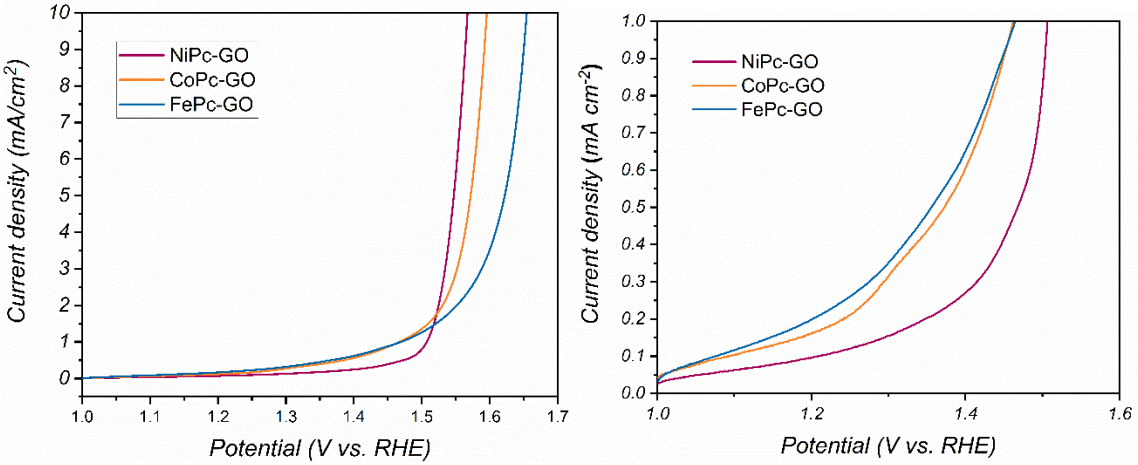

Figure S54. LSV curves of NiPc-GO, CoPc-GO and FePc-GO at current densities from 0-10 mA cm^{-2} (left) and 0-1 mA cm^{-2} (right).

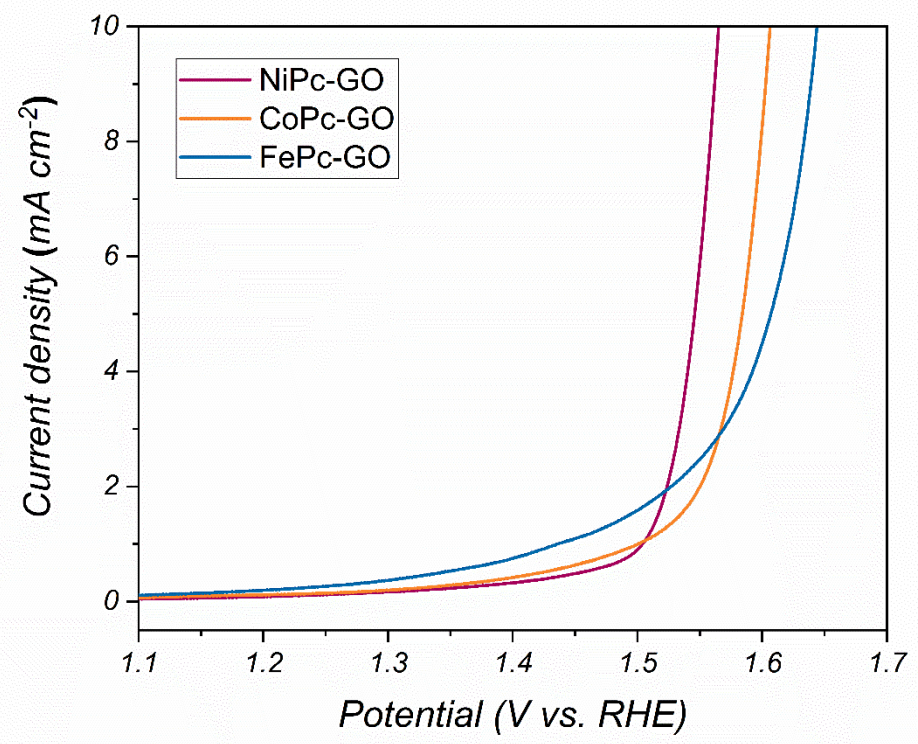

Figure S55. Electrode 1: LSV curves of NiPc-GO, CoPc-GO and FePc-GO at current densities from 0-10 mA cm^{-2}.

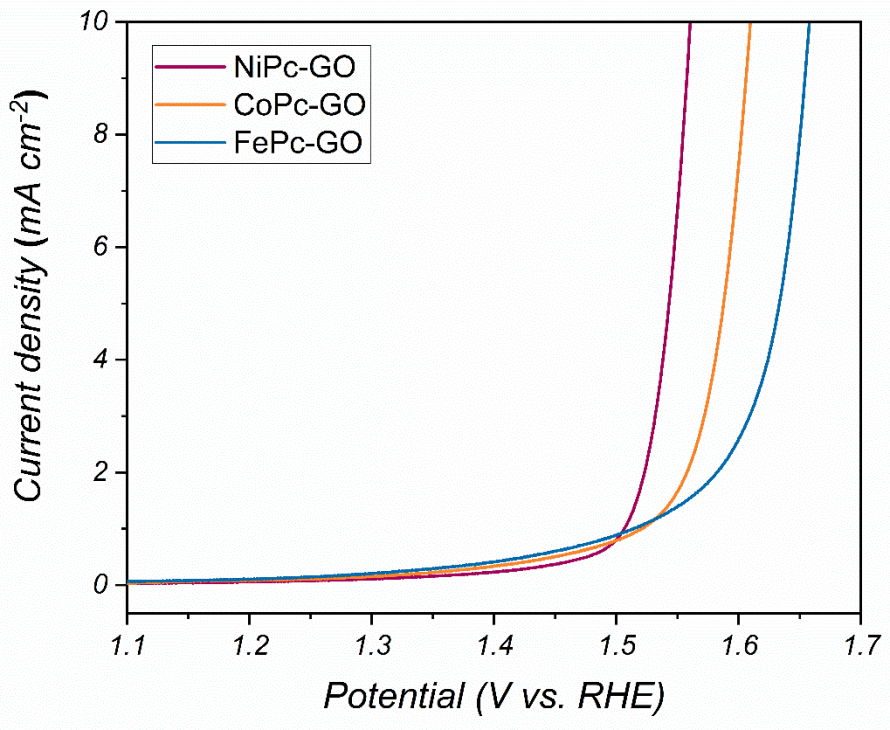

Figure S56. Electrode 2: LSV curves of NiPc-GO, CoPc-GO and FePc-GO at current densities from 0-10 mA cm^{-2}.

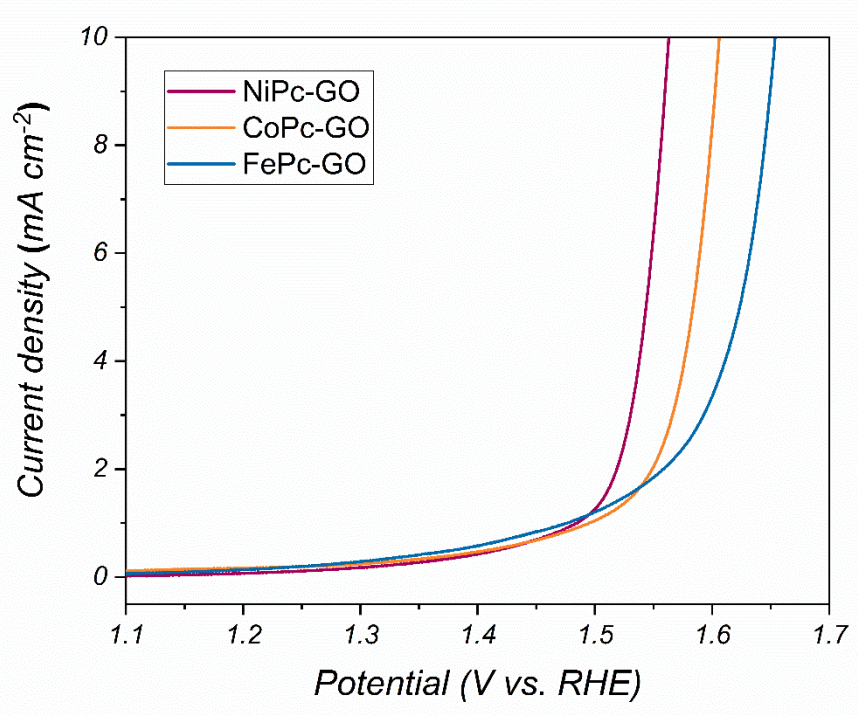

Figure S57. Electrode 3: LSV curves of NiPc-GO, CoPc-GO and FePc-GO at current densities from 0-10 mA cm^{-2}.

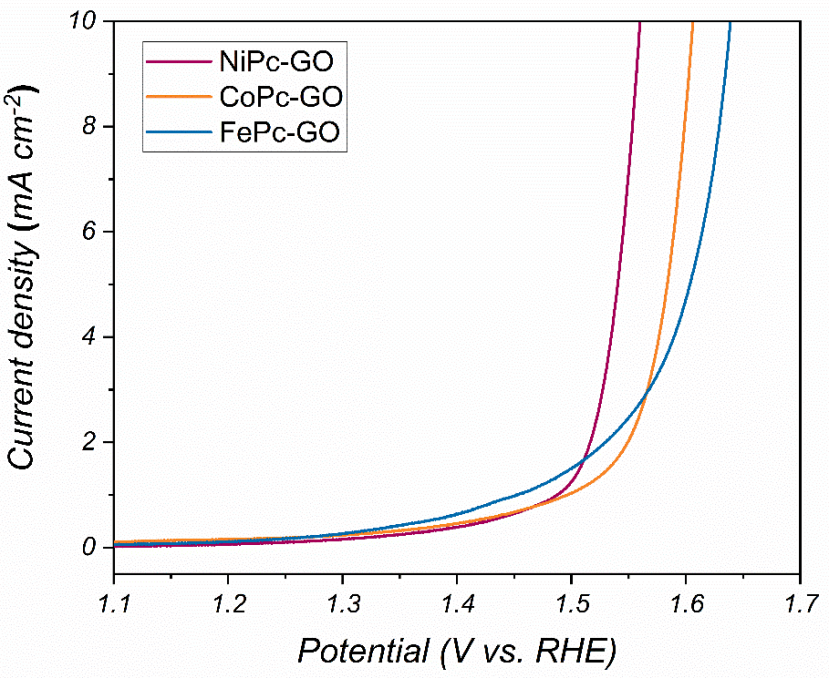

Figure S58. Electrode 4: LSV curves of NiPc-GO, CoPc-GO and FePc-GO at current densities from 0-10 mA cm^{-2}.

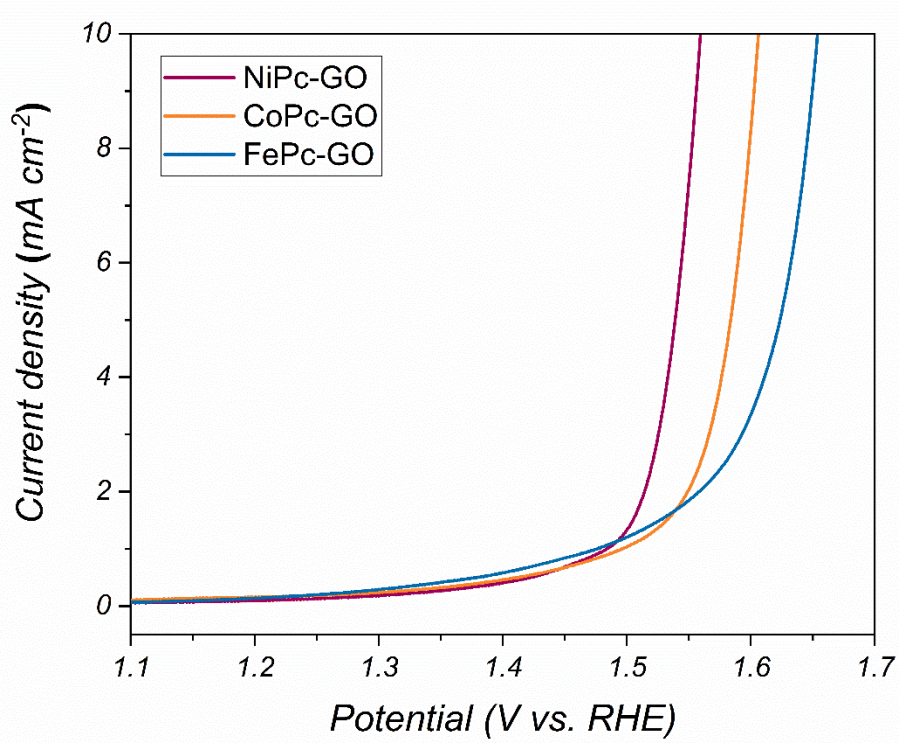

Figure S59. Electrode 5: LSV curves of NiPc-GO, CoPc-GO and FePc-GO at current densities from 0-10 mA cm^{-2}.

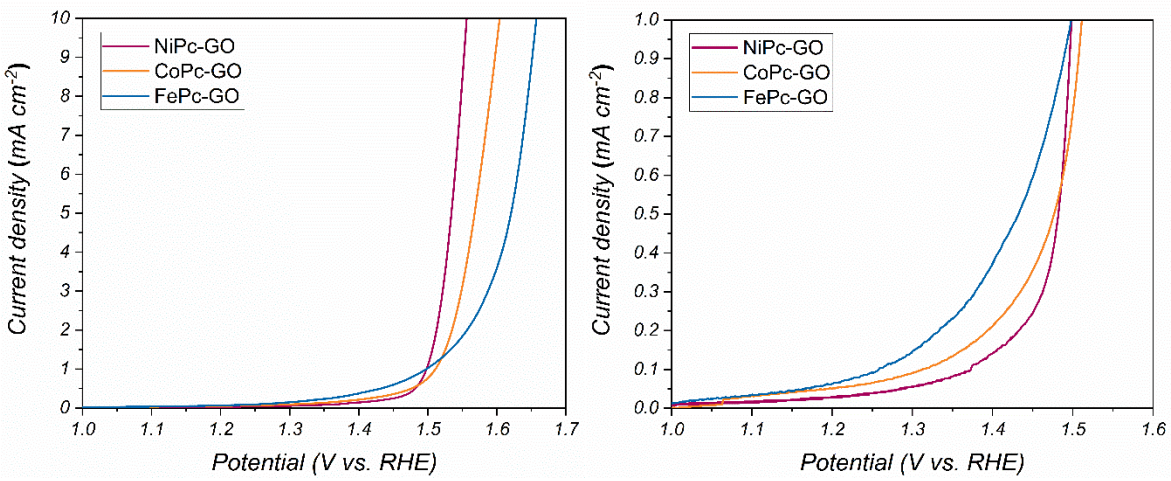

Figure S60. LSV curves of NiPc-GO, CoPc-GO and FePc-GO at current densities from 0-10 mA cm^{-2} (left) and 0-1 mA cm^{-2} (right) on a PGSTAT302N, Metrohm electrochemical station.

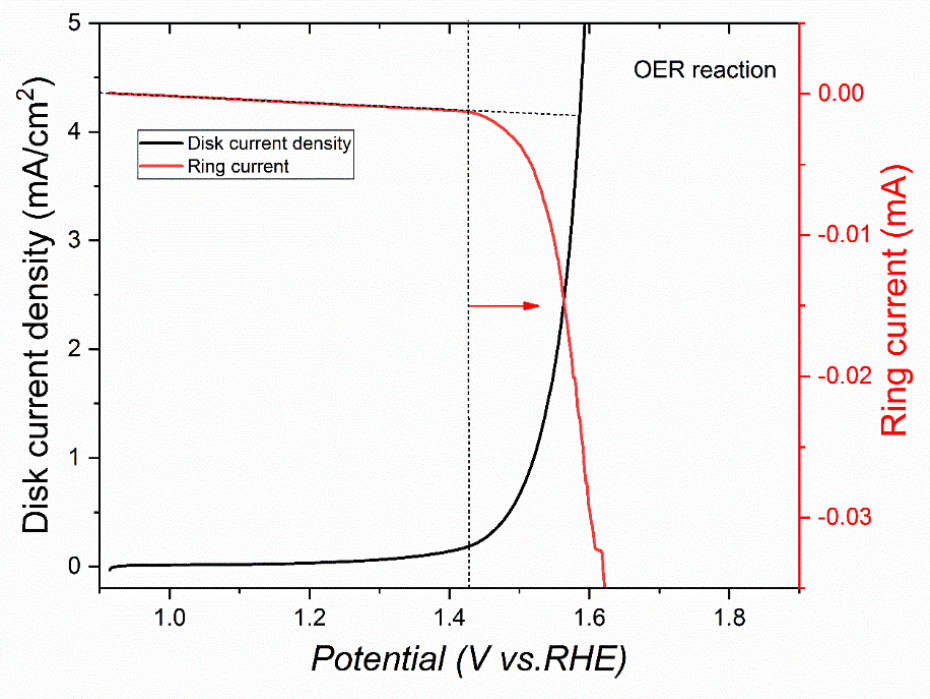

Figure S61. Rotation ring disk measurement of FePc-GO to confirm the production of O_2 at low potential range (1.4 V-1.5 V).

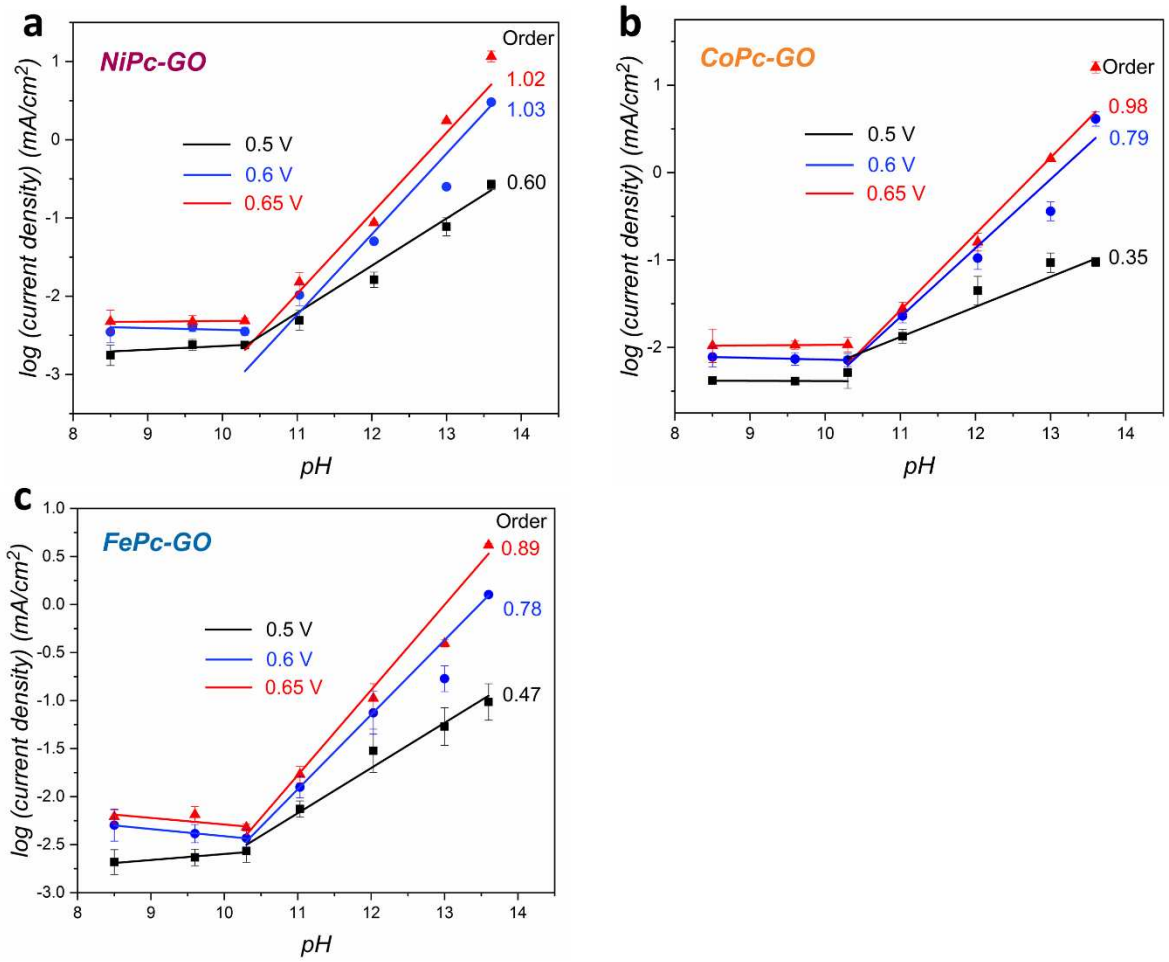

Figure S62. Dependence of current density at fixed potentials *vs.* Ag/AgCl of (a) NiPc-GO, and (b) CoPc-GO and (c) FePc-GO on pH value of electrolyte. For the pH dependent experiments, 1 M KOH and 0.5 M $NaClO_4$ solutions were used to prepare the electrolyte.

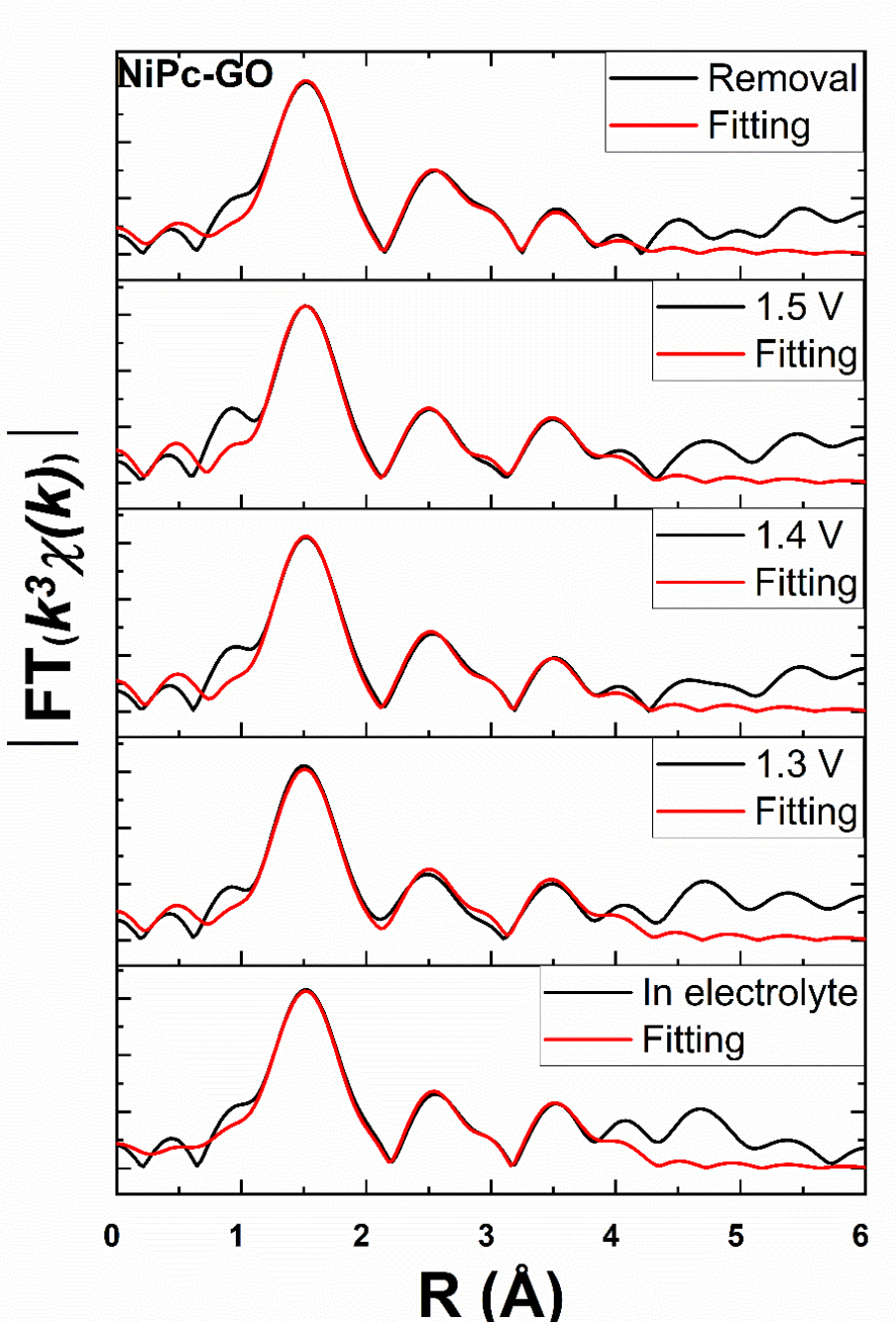

Figure S63. Fitting (red) of the experimental (black) Ni *K*-edge EXAFS spectra $|\mathrm{FT}(k^3\chi(k))|$ of NiPc-GO at different potentials (phase uncorrected).

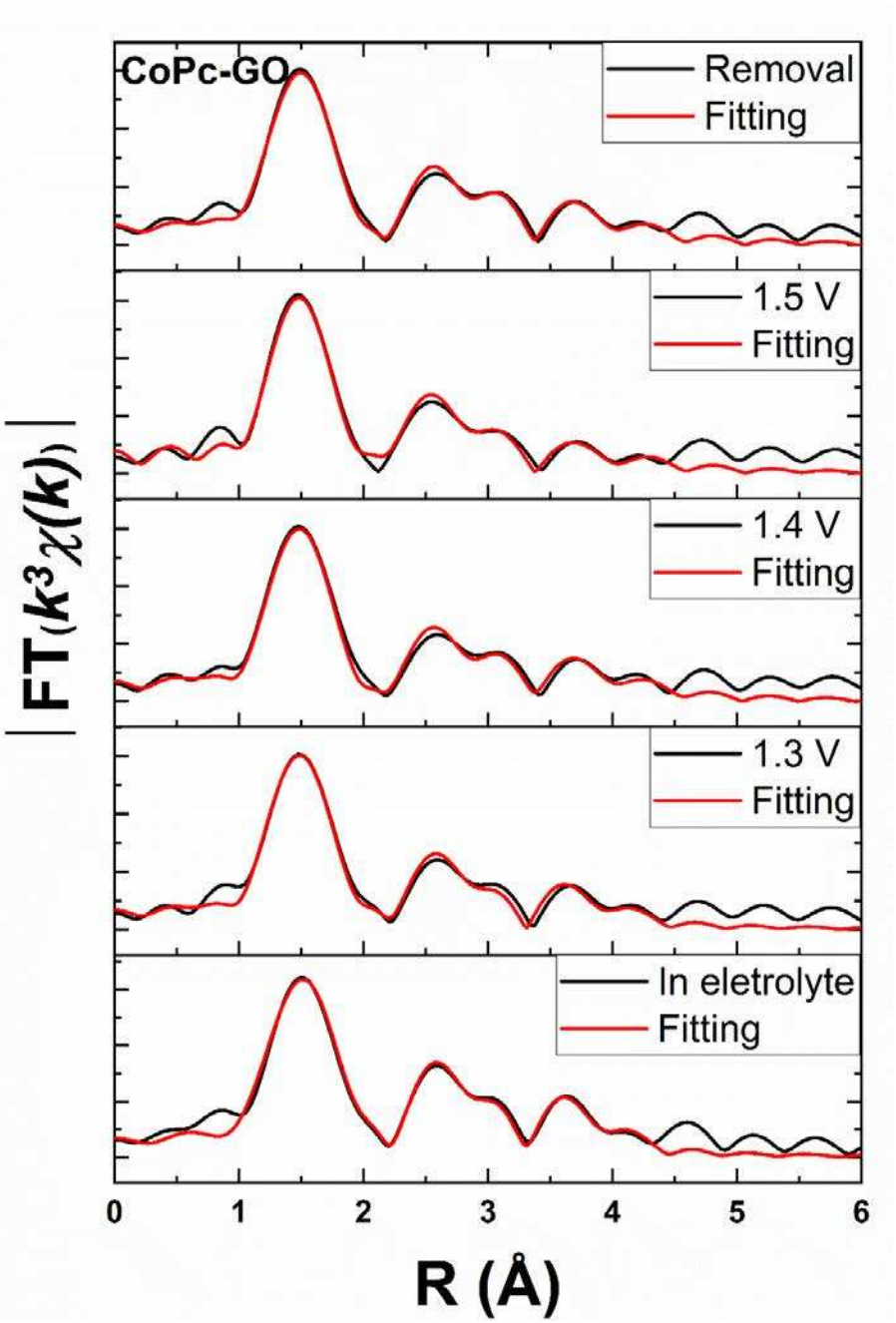

Figure S64. Fitting (red) of the experimental (black) Co *K*-edge EXAFS spectra $|\mathrm{FT}(k^3\chi(k))|$ of CoPc-GO at different potentials (phase uncorrected).

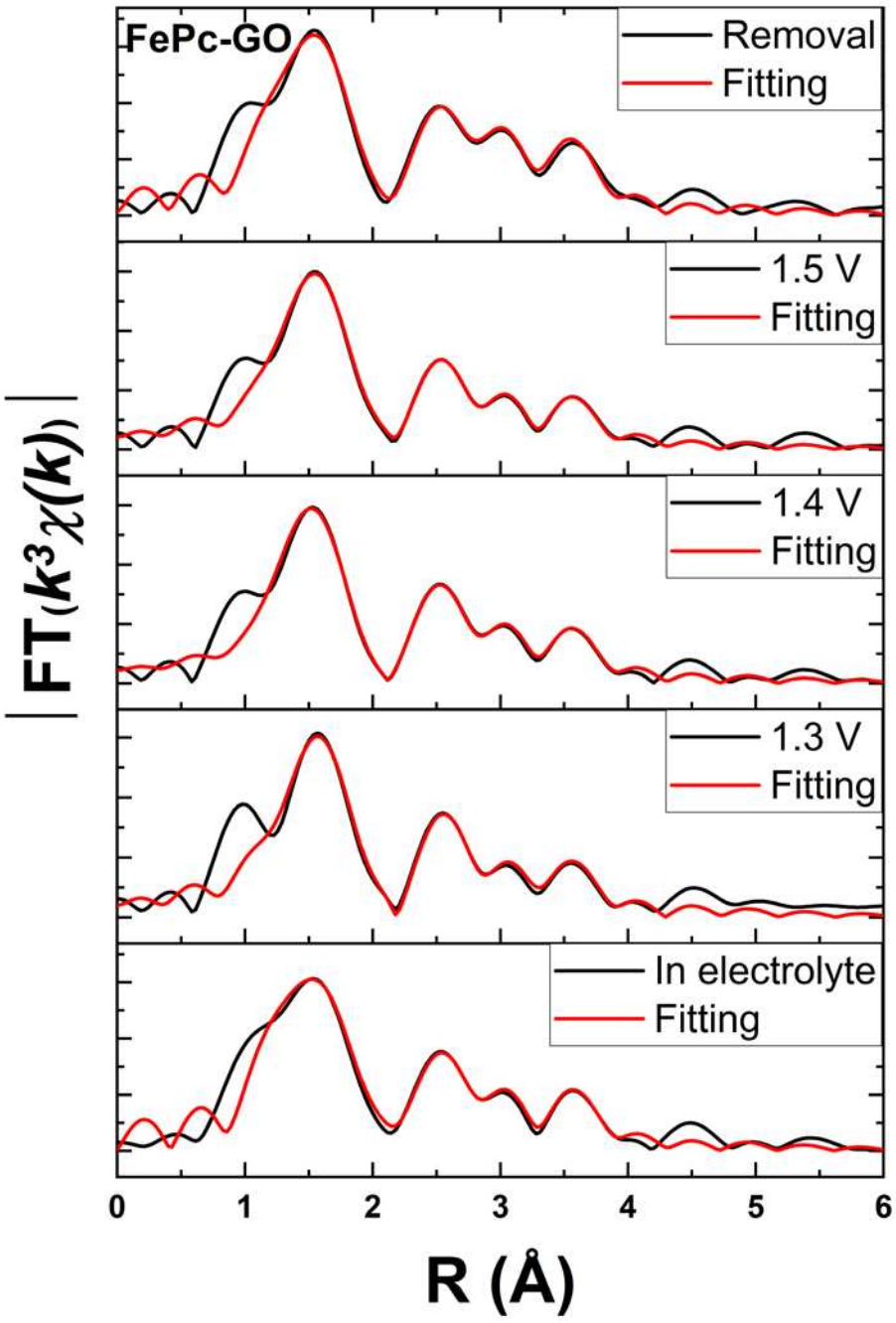

Figure S65. Fitting (red) of the experimental (black) Fe *K*-edge EXAFS spectra $|\mathrm{FT}(k^3\chi(k))|$ of FePc-GO at different potentials (phase uncorrected).

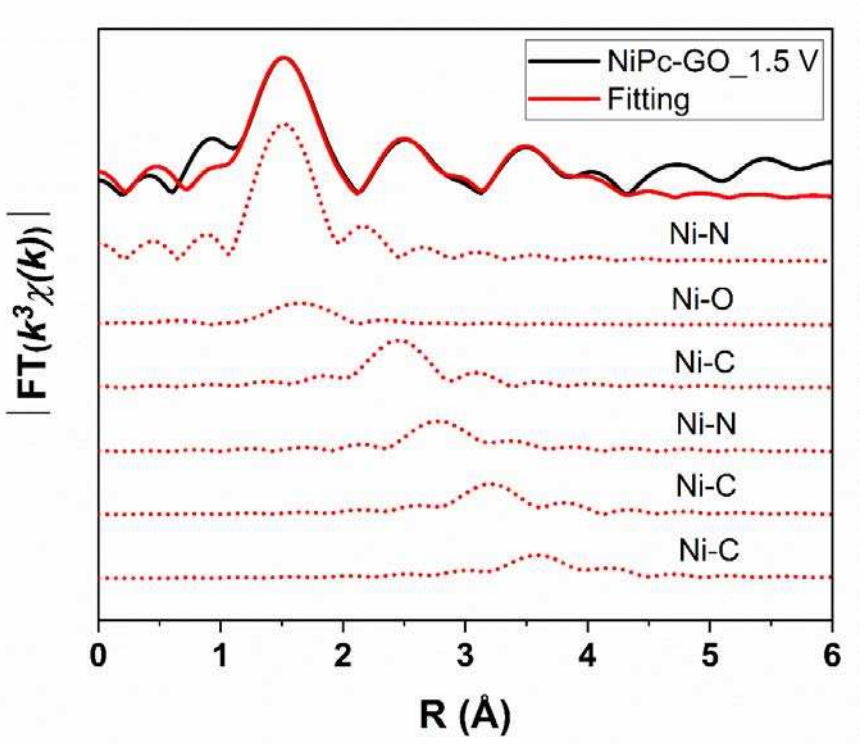

Figure S66. Fitting (red) of the experimental (black) Ni *K*-edge EXAFS spectrum $|\mathrm{FT}(k^3\chi(k))|$ of NiPc-GO at the applied potential of 1.5 V and the corresponding fitted single scattering paths.

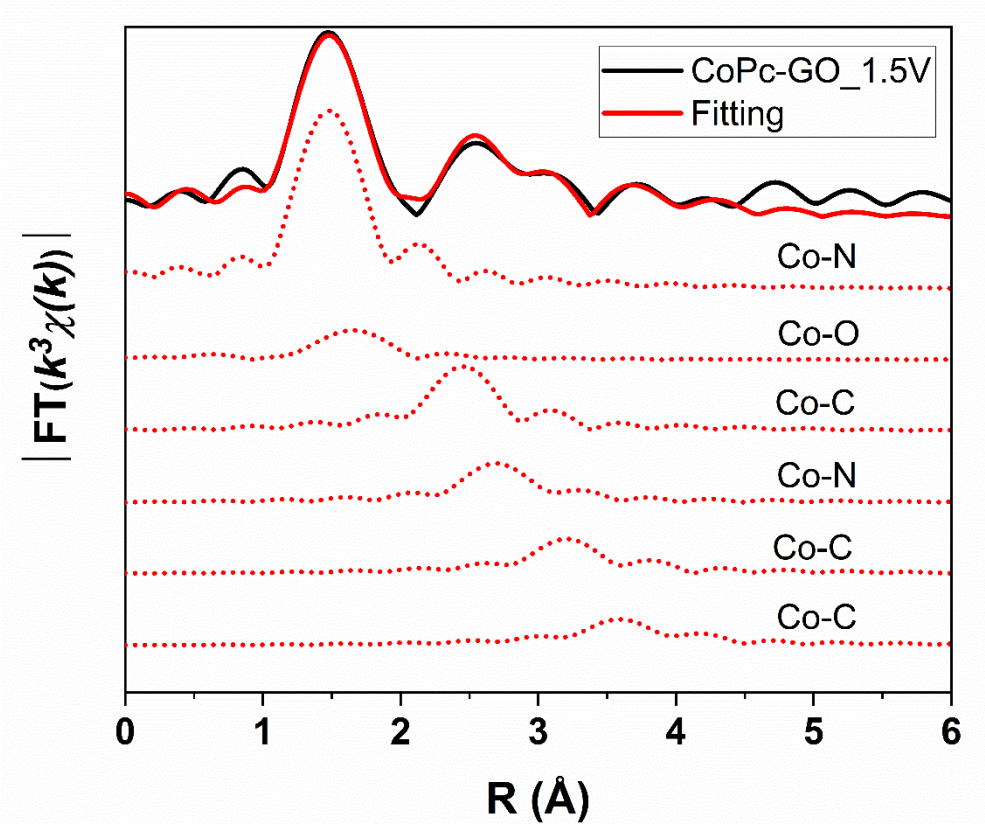

Figure S67. Fitting (red) of the experimental (black) Co *K*-edge EXAFS spectrum $|\mathrm{FT}(k^3\chi(k))|$ of CoPc-GO at the applied potential of 1.5 V and the corresponding fitted single scattering paths.

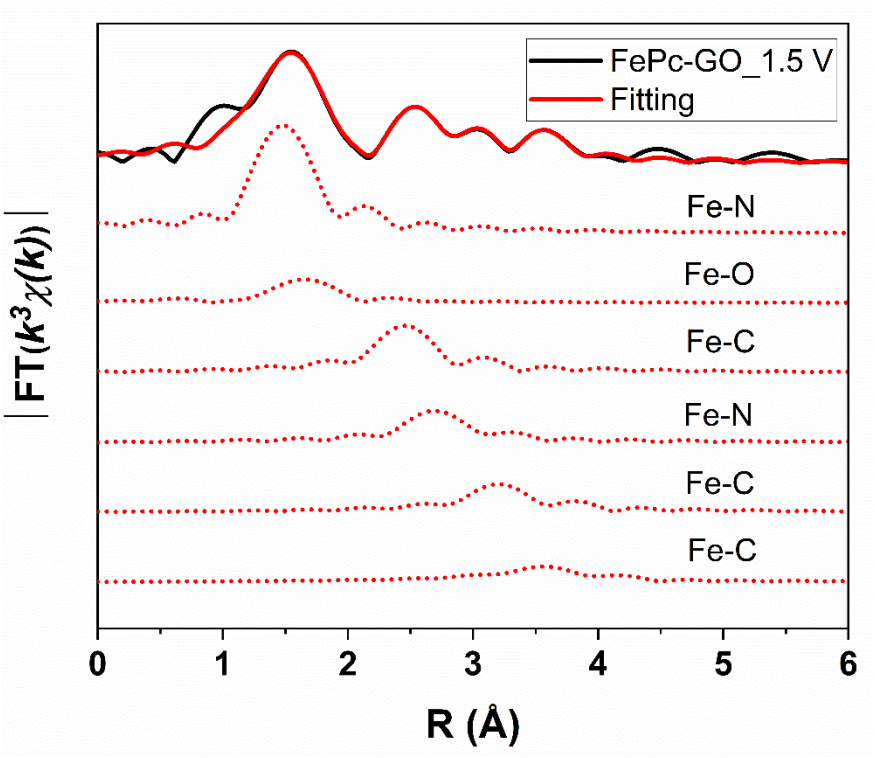

Figure S68. Fitting (red) of the experimental (black) Fe *K*-edge EXAFS spectrum $|\mathrm{FT}(k^3\chi(k))|$ of FePc-GO at the applied potential of 1.5 V and the corresponding fitted single scattering paths.

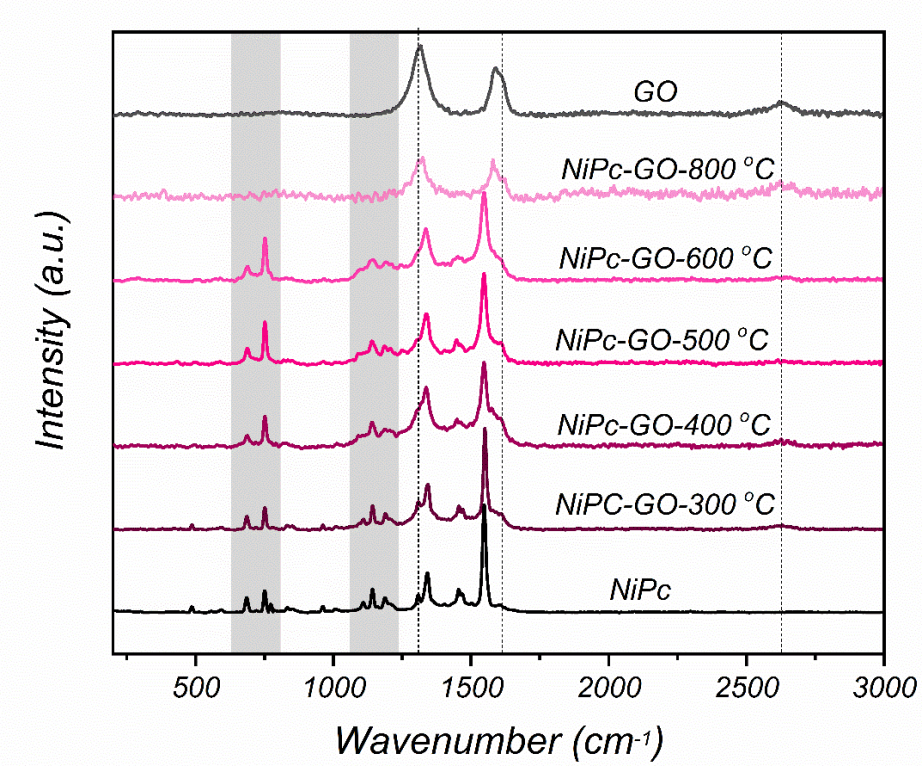

Figure S69. Raman spectra of NiPc-GO samples obtained at different synthesis temperatures.

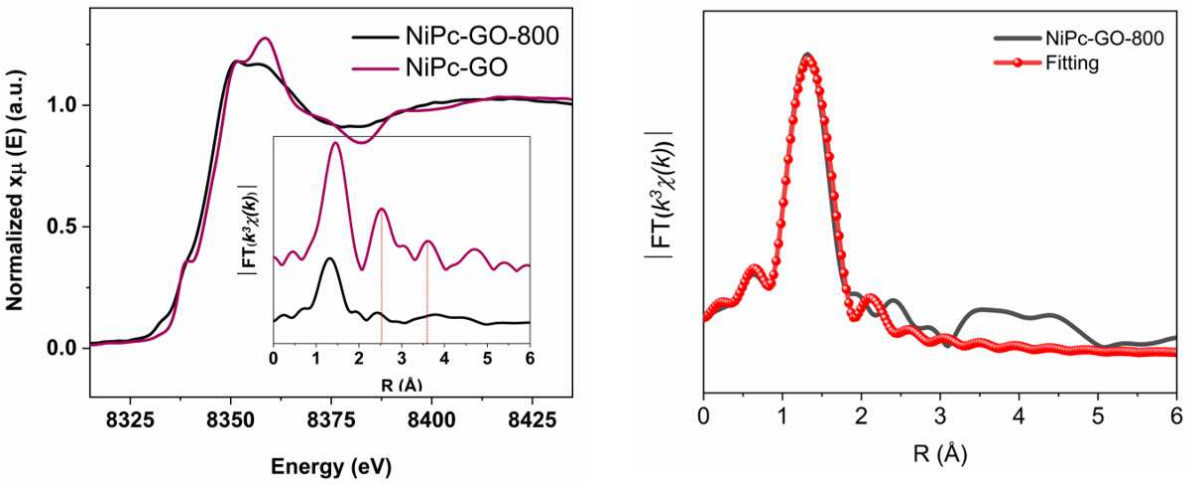

Figure S70. Ni *K*-edge XANES and EXAFS spectra of NiPc-GO obtained at 300 ºC and 800 ºC (left). Fitting (red) of Ni *K*-edge EXAFS spectrum of NiPc-GO at 800 ºC (right).

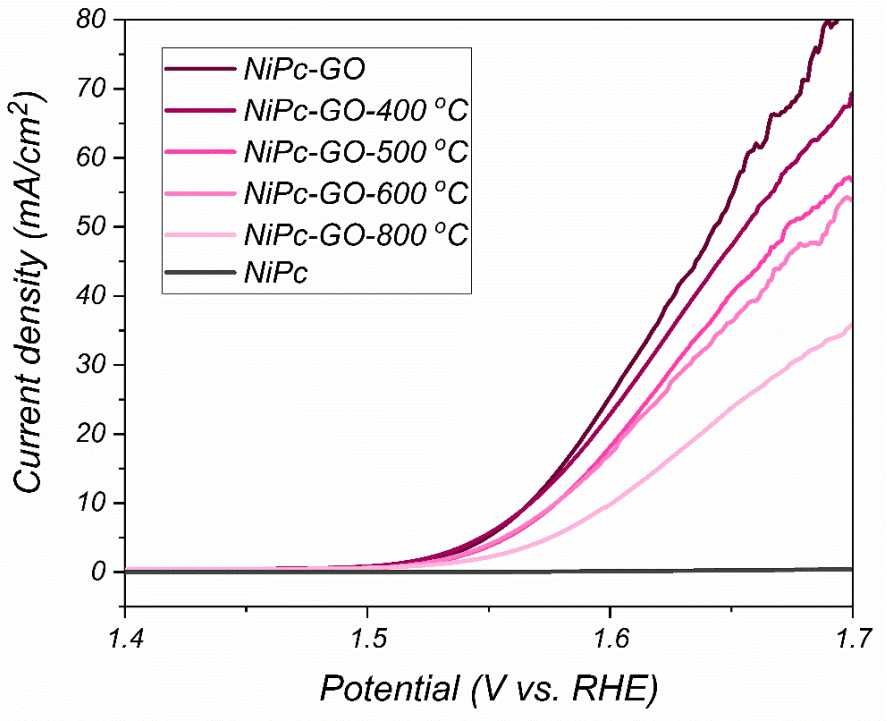

Figure S71. OER performances of NiPc-GO obtained at different synthesis temperatures.

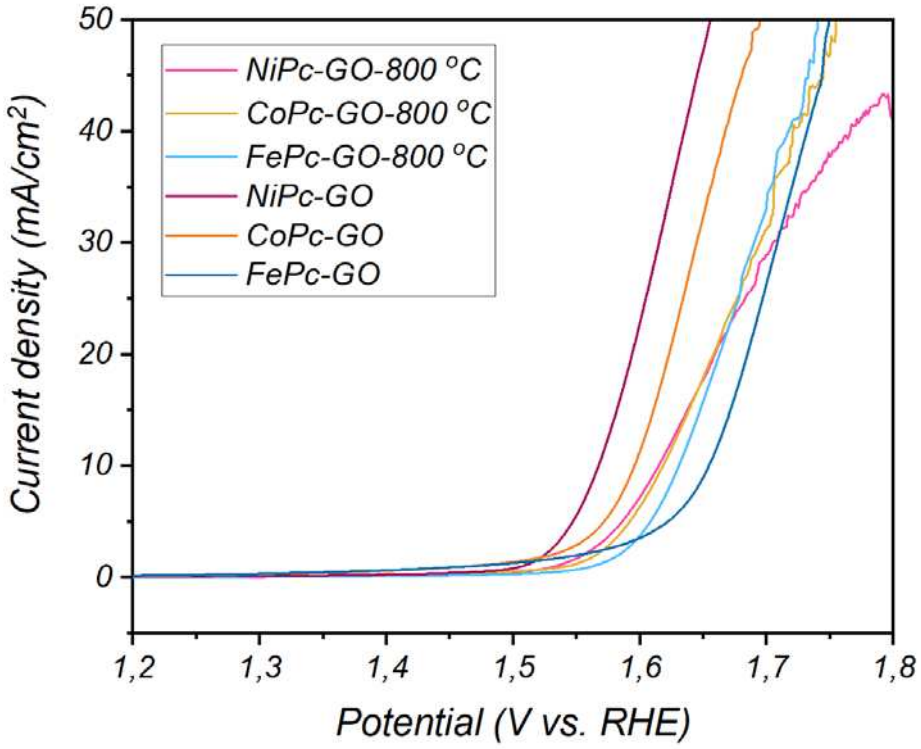

Figure S72. OER performances of NiPc-GO, CoPc-GO and FePc-GO before and after 800 °C.

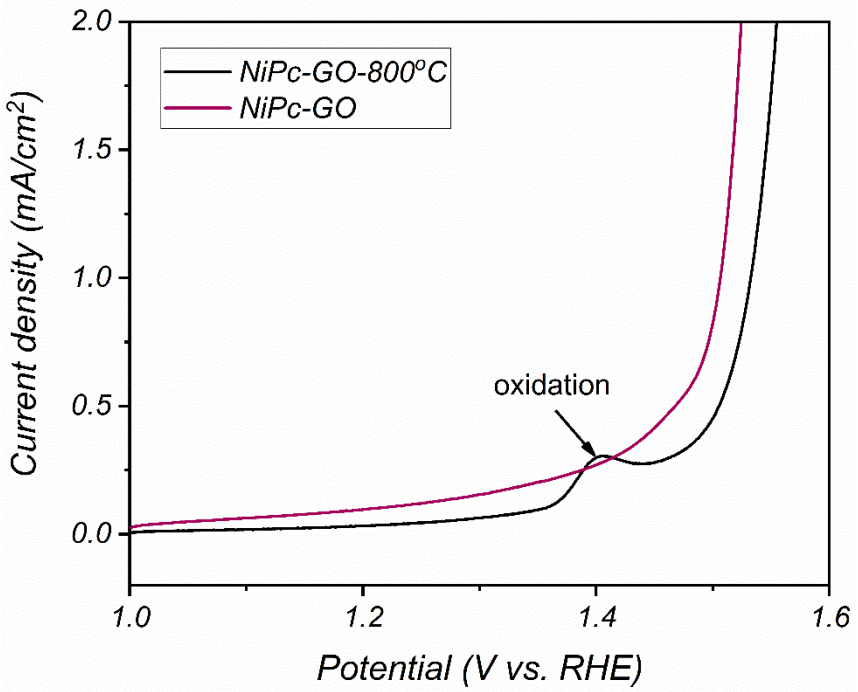

Figure S73. LSV curves of sample NiPc-GO and after pyrolysis at 800 °C.

Table S1 Mass content of the metallic elements in NiPc-GO, CoPc-GO and FePc-GO.

	NiPc-GO	CoPc-GO	FePc-GO
ICP content	1.65 wt%	1.70 wt%	1.60 wt%
Theoretical content	1.96 wt%	1.89 wt%	1.83 wt%

Table S2. Elemental analysis of GO before and after 300 °C pyrolysis.

Name (wt %)	N	C	H	S	O
GO-300	0.82	90.79	0.21	0.01	3.16
GO	0.67	91.37	0.31	0.03	4.31

Table S3 ICP-MS measurements of the electrolytes before and after OER and ORR tests.

	Ni [ng/mL]	Co [ng/mL]	Fe [ng/mL]	Pt [ng/mL]
Fresh KOH	55	1.5	42	0.10
OER	50	2.0	45	0.12
ORR	52	1.1	43	0.10

Table S4a. Main interatomic distances, atomic coordination numbers (*N*) and Debye-Waller factors (σ^2) calculated from Artemis fitting of the experimental *operando* Ni *K*-edge FT$|k^3\chi(k)|$ spectra of NiPc-GO. S_0^2 denotes the amplitude reduction factor and ΔE_0 the energy shift.

Sample	Bond	*N*	σ^2	**r** (A)
NiPc-GO	Ni-N	4.0	0.00072	1.9023
$S_0^2 \approx 0.72$	Ni-C	8.0	0.00578	2.9419
$\Delta E_0 \approx 7.43$ eV	Ni-N	4.0	0.00189	3.3801
No. of independent points:	Ni-C	6.0	0.00764	3.7894
No. of Variables: 10	Ni-C	8.0	0.00049	4.2684
R-factor: 0.0075				
NiPc-GO Open Circuit	Ni-N	4.0	0.00206	1.9120
$S_0^2 \approx 0.72$	Ni-O	0.2	0.00982	1.9739
$\Delta E_0 \approx 7.11$ eV	Ni-C	8.0	0.00438	2.9513
No. of independent points:	Ni-N	4.0	0.00992	3.3832
No. of Variables: 12	Ni-C	6.0	0.00216	3.8544
R-factor: 0.0102	Ni-C	8.0	0.00242	4.2698
NiPc-GO at 1.3 V	Ni-N	4.0	0.00200	1.9081
$S_0^2 \approx 0.72$	Ni-O	0.5	0.00882	1.9746
$\Delta E_0 \approx 7.06$ eV	Ni-C	8.0	0.00340	2.9600
No. of independent points:	Ni-N	4.0	0.00985	3.3801
No. of Variables: 12	Ni-C	6.0	0.00044	3.8501
R-factor: 0.0101	Ni-C	8.0	0.00389	4.2584
NiPc-GO at 1.4 V	Ni-N	4.0	0.00102	1.9011
$S_0^2 \approx 0.72$	Ni-O	0.7	0.00879	1.9713
$\Delta E_0 \approx 7.02$ eV	Ni-C	8.0	0.00215	2.9505
No. of independent points:	Ni-N	4.0	0.00996	3.3745
No. of Variables: 12	Ni-C	6.0	0.00197	3.8406
R-factor: 0.0093	Ni-C	8.0	0.00439	4.2687
NiPc-GO at 1.5 V	Ni-N	4.0	0.00316	1.9024
$S_0^2 \approx 0.72$	Ni-O	0.7	0.00682	1.9603
$\Delta E_0 \approx 7.04$ eV	Ni-C	8.0	0.00383	2.9424
No. of independent points:	Ni-N	4.0	0.00986	3.3872
No. of Variables: 12	Ni-C	6.0	0.00011	3.8602
R-factor: 0.0098	Ni-C	8.0	0.00282	4.2603
NiPc-GO Remove Potential	Ni-N	4.0	0.00291	1.9103
$S_0^2 \approx 0.72$	Ni-O	0.3	0.00970	1.9681
$\Delta E_0 \approx 7.12$ eV	Ni-C	8.0	0.00472	2.9009
No. of independent points:	Ni-N	4.0	0.00990	3.3798
No. of Variables: 12	Ni-C	6.0	0.00206	3.8581
R-factor: 0.0102	Ni-C	8.0	0.00229	4.2666
NiPc-GO-800	Ni-N	4.2	0.01124	1.8642
$S_0^2 \approx 0.72$				
$\Delta E_0 \approx 7.12$ eV				
No. of independent points:				
No. of Variables: 12				
R-factor: 0.0102				

Table S4b. Main interatomic distances, atomic coordination numbers (*N*) and Debye-Waller factors (σ^2) calculated from Artemis fitting of the experimental *operando* Co *K*-edge FT$|k^3\chi(k)|$ spectra of CoPc-GO. S_0^2 denotes the amplitude reduction factor and ΔE_0 the energy shift.

Sample	**Bond**	***N***	$\boldsymbol{\sigma^2}$	**r** (A)
CoPc-GO	Co-N	4.0	0.00096	1.9090
$S_0^2 \approx 0.65$	Co-C	8.0	0.00472	2.9543
$\Delta E_0 \approx 7.46$ eV	Co-N	4.0	0.00160	3.3703
No. of independent points:	Co-C	6.0	0.00343	3.7625
No. of Variables: 10	Co-C	8.0	0.00107	4.2935
R-factor: 0.0076				
CoPc-GO Open Circuit	Co-N	4.0	0.00139	1.9014
$S_0^2 \approx 0.65$	Co-O	0.2	0.00992	1.9743
$\Delta E_0 \approx 7.64$ eV	Co-C	8.0	0.00376	2.9229
No. of independent points:	Co-N	4.0	0.00050	3.2692
No. of Variables: 12	Co-C	6.0	0.00654	3.8210
R-factor: 0.0072	Co-C	8.0	0.00286	4.2857
CoPc-GO at 1.3 V	Co-N	4.0	0.00051	1.9010
$S_0^2 \approx 0.65$	Co-O	0.6	0.00924	1.9747
$\Delta E_0 \approx 7.18$ eV	Co-C	8.0	0.00586	2.9279
No. of independent points:	Co-N	4.0	0.00106	3.2795
No. of Variables: 12	Co-C	6.0	0.01329	3.8824
R-factor: 0.0082	Co-C	8.0	0.00163	4.2878
CoPc-GO at 1.4 V	Co-N	4.0	0.00104	1.9002
$S_0^2 \approx 0.65$	Co-O	0.8	0.00880	1.9738
$\Delta E_0 \approx 7.24$ eV	Co-C	8.0	0.00336	2.9386
No. of independent points:	Co-N	4.0	0.00232	3.2814
No. of Variables: 12	Co-C	6.0	0.00143	3.9412
R-factor: 0.0087	Co-C	8.0	0.00489	4.3001
CoPc-GO at 1.5 V	Co-N	4.0	0.00110	1.9008
$S_0^2 \approx 0.65$	Co-O	0.8	0.00544	1.9512
$\Delta E_0 \approx 6.95$ eV	Co-C	8.0	0.00348	2.9243
No. of independent points:	Co-N	4.0	0.00114	3.2543
No. of Variables: 12	Co-C	6.0	0.00s24	3.8964
R-factor: 0.0092	Co-C	8.0	0.00364	4.2908
CoPc-GO Removed	Co-N	4.0	0.00031	1.9030
$S_0^2 \approx 0.65$	Co-O	0.4	0.00992	1.9786
$\Delta E_0 \approx 7.46$ eV	Co-C	8.0	0.00342	2.9296
No. of independent points:	Co-N	4.0	0.00233	3.2491
No. of Variables: 12	Co-C	6.0	0.00082	3.9588
R-factor: 0.0099	Co-C	8.0	0.00460	4.3148

Table S4c. Main interatomic distances, atomic coordination numbers (*N*) and Debye-Waller factors (σ^2) calculated from Artemis fitting of the experimental *operando* Fe *K*-edge FT$|k^3\chi(k)|$ spectra of FePc-GO. S_0^2 denotes the amplitude reduction factor and ΔE_0 the energy shift.

Sample	Bond	*N*	σ^2	**r** (A)
FePc-GO	Fe-N	4.0	0.00494	1.9199
$S_0^2 \approx 0.81$	Fe-C	8.0	0.00965	2.9814
$\Delta E_0 \approx 2.28$ eV	Fe-N	4.0	0.00068	3.3895
No. of independent points:	Fe-C	6.0	0.00605	3.7967
No. of Variables: 10	Fe-C	8.0	0.00692	4.2964
R-factor: 0.0066				
FePc-GO Open Circuit	Fe-N	4.0	0.00345	1.9293
$S_0^2 \approx 0.81$	Fe-O	0.2	0.00827	2.0463
$\Delta E_0 \approx 1.92$ eV	Fe-C	8.0	0.00624	2.9850
No. of independent points:	Fe-N	4.0	0.00123	3.3902
No. of Variables: 12	Fe-C	6.0	0.00551	3.7488
R-factor: 0.0078	Fe-C	8.0	0.00637	4.2997
FePc-GO at 1.3 V	Fe-N	4.0	0.00617	1.9236
$S_0^2 \approx 0.81$	Fe-O	0.6	0.00651	2.0181
$\Delta E_0 \approx 2.11$ eV	Fe-C	8.0	0.00930	2.9992
No. of independent points:	Fe-N	4.0	0.00178	3.3943
No. of Variables: 12	Fe-C	6.0	0.00391	3.6984
R-factor: 0.0098	Fe-C	8.0	0.00931	4.3140
FePc-GO at 1.4 V	Fe-N	4.0	0.00453	1.9196
$S_0^2 \approx 0.81$	Fe-O	0.7	0.00489	2.0275
$\Delta E_0 \approx 2.05$ eV	Fe-C	8.0	0.00751	2.9865
No. of independent points:	Fe-N	4.0	0.00320	3.3705
No. of Variables: 12	Fe-C	6.0	0.00298	3.7692
R-factor: 0.0099	Fe-C	8.0	0.00738	4.3164
FePc-GO at 1.5 V	Fe-N	4.0	0.00465	1.9165
$S_0^2 \approx 0.81$	Fe-O	0.7	0.00630	2.0216
$\Delta E_0 \approx 2.08$ eV	Fe-C	8.0	0.00768	2.9780
No. of independent points:	Fe-N	4.0	0.00344	3.3901
No. of Variables: 12	Fe-C	6.0	0.00467	3.7503
R-factor: 0.0071	Fe-C	8.0	0.00705	4.3398
FePc-GO Remove Potential	Fe-N	4.0	0.00360	1.9233
$S_0^2 \approx 0.81$	Fe-O	0.4	0.00997	2.0423
$\Delta E_0 \approx 2.09$ eV	Fe-C	8.0	0.00687	2.9844
No. of independent points:	Fe-N	4.0	0.00382	3.3743
No. of Variables: 12	Fe-C	6.0	0.00344	3.7367
R-factor: 0.0083	Fe-C	8.0	0.00543	4.3144

Figure S74. Potential active sites among coordinating atoms (C, N1, N2).

Table S5. Free energies of *OH, *O and *OOH on the selected active sites and energy barriers over four steps of the OER.

				OER				***ORR***			
	$\Delta G_{(*OH)}$	$\Delta G_{(*O)}$	$\Delta G_{(*OOH)}$	ΔG_A	ΔG_B	ΔG_C	ΔG_D	ΔG_E	ΔG_F	ΔG_G	ΔG_H
NiPc-GO-C	2.31	4.70	5.64	2.31	2.39	0.94	-0.72	0.72	-0.94	-2.39	-2.31
NiPc-GO-Ni	2.31	4.97	5.92	2.31	2.66	0.95	-0.93	0.93	-0.95	-2.66	-2.31
NiPc-GO-N$_1$	3.13	5.24	5.38	3.13	2.11	0.14	-0.46	0.46	-0.14	-2.11	-3.13
NiPc-GO-N$_2$	5.30	5.51	6.19	5.30	0.20	0.68	-1.27	1.27	-0.68	-0.20	-5.30
CoPc-GO-C	2.45	6.33	5.21	2.45	3.88	-1.12	-0.29	0.29	1.12	-3.88	-2.45
CoPc-GO-Co	1.35	3.61	4.39	1.35	2.26	0.78	0.53	-0.53	-0.78	-2.26	-1.35
CoPc-GO-N$_1$	2.45	3.84	4.39	2.45	1.39	0.55	0.53	-0.53	-0.55	-1.43	-2.45
CoPc-GO-N$_2$	4.35	5.51	6.57	4.35	1.16	1.06	-1.65	1.65	-1.06	-1.16	-4.35
FePc-GO-C	1.75	3.25	6.03	1.75	1.50	2.78	-1.11	1.11	-2.78	-1.50	-1.75
FePc-GO-Fe	0.54	1.62	3.31	0.54	1.08	1.69	1.61	-1.61	-1.69	-1.08	-0.54
FePc-GO-N$_1$	1.92	3.52	5.76	1.92	1.6	2.24	-0.84	0.84	-2.24	-1.6	-1.92
FePc-GO-N$_2$	3.82	5.97	6.30	3.82	2.15	0.33	-1.38	1.38	-0.33	-2.15	-3.82

Table S6. Zero-point energy corrections and entropic contributions to free energies.

Species	TS (eV)	ZPE (eV)
***H**	0	0.17
***O**	0	0.007
***OH**	0	0.33
***OOH**	0	0.43
H_2	0.41	0.27
H_2O	0.58	0.57
O_2	0.64	0.1

Table S7. Free energies of $*O_2$ and $*H_2O$ on the selected Ni, Co and Fe centers in NiPc-GO, CoPc-GO and FePc-GO.

	O_2	***H_2O***
NiPc-GO	-0.56	-0.21
CoPc-GO	-0.42	-0.37
FePc-GO	-1.40	-0.52

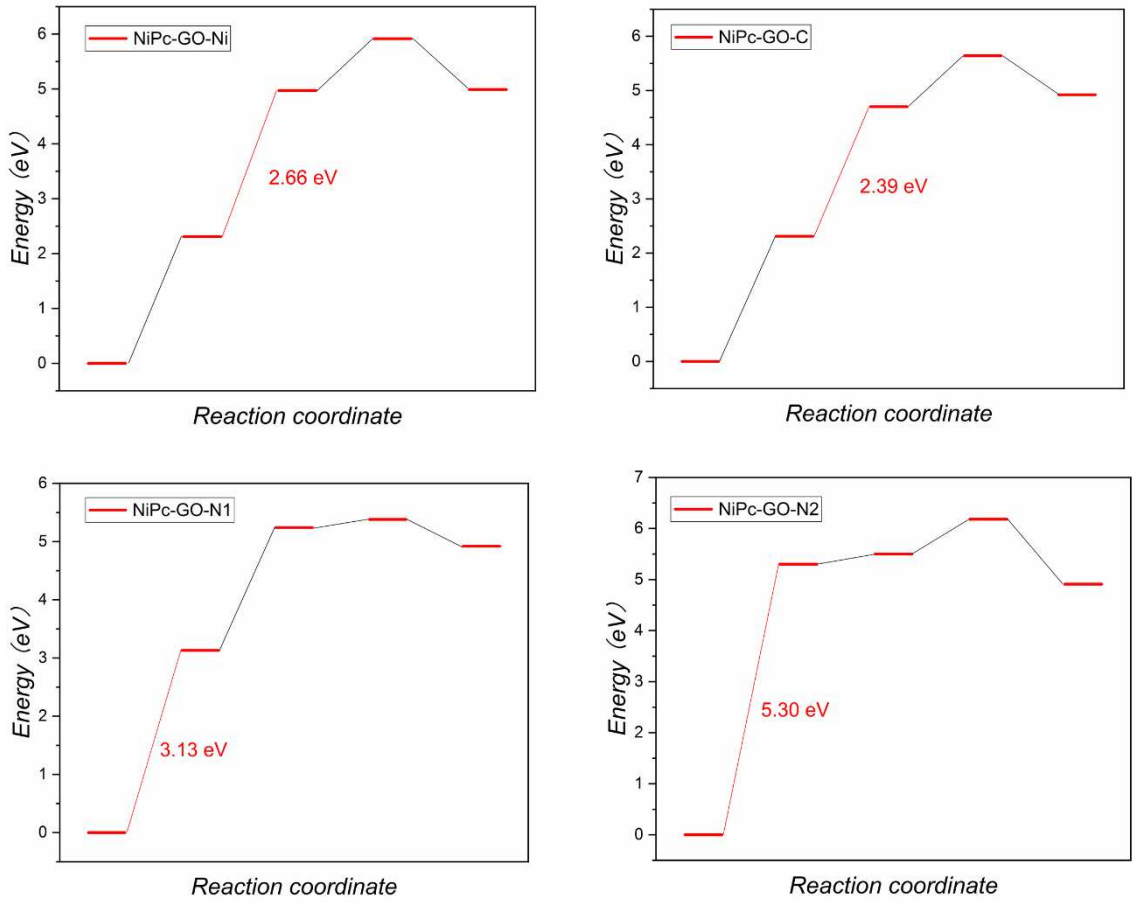

Figure S75. DFT simulations for the analysis of the energy diagram for OER over NiPc-GO on all possible active sites.

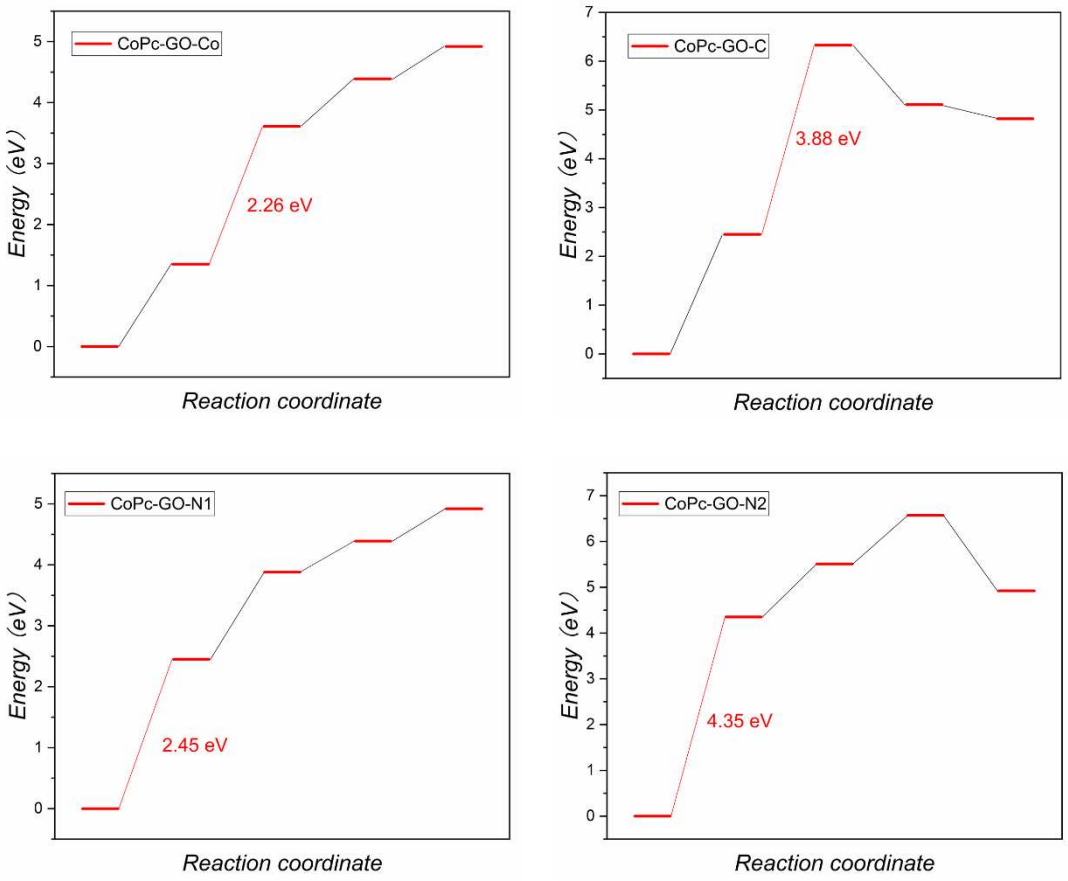

Figure S76. DFT simulations for analysis of the energy diagram for OER over CoPc-GO on all possible active sites.

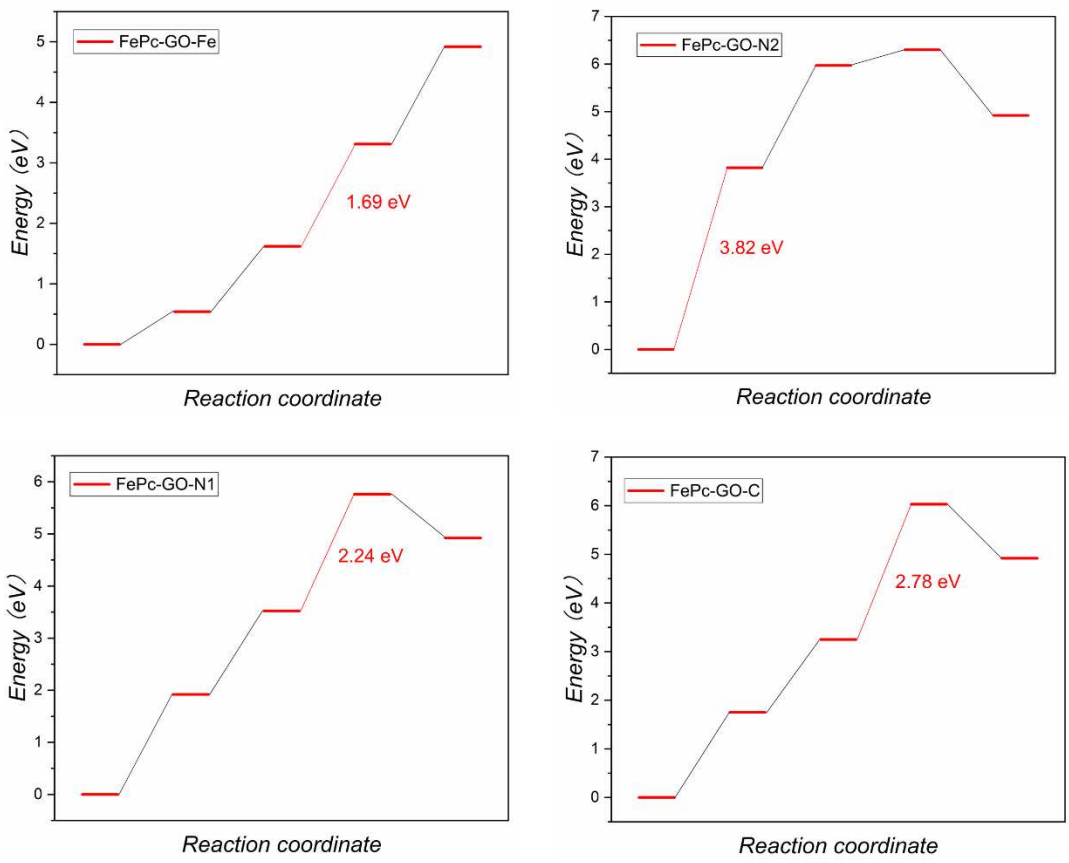

Figure S77. DFT simulations for analysis of energy diagram for OER over FePc-GO on all possible active sites.

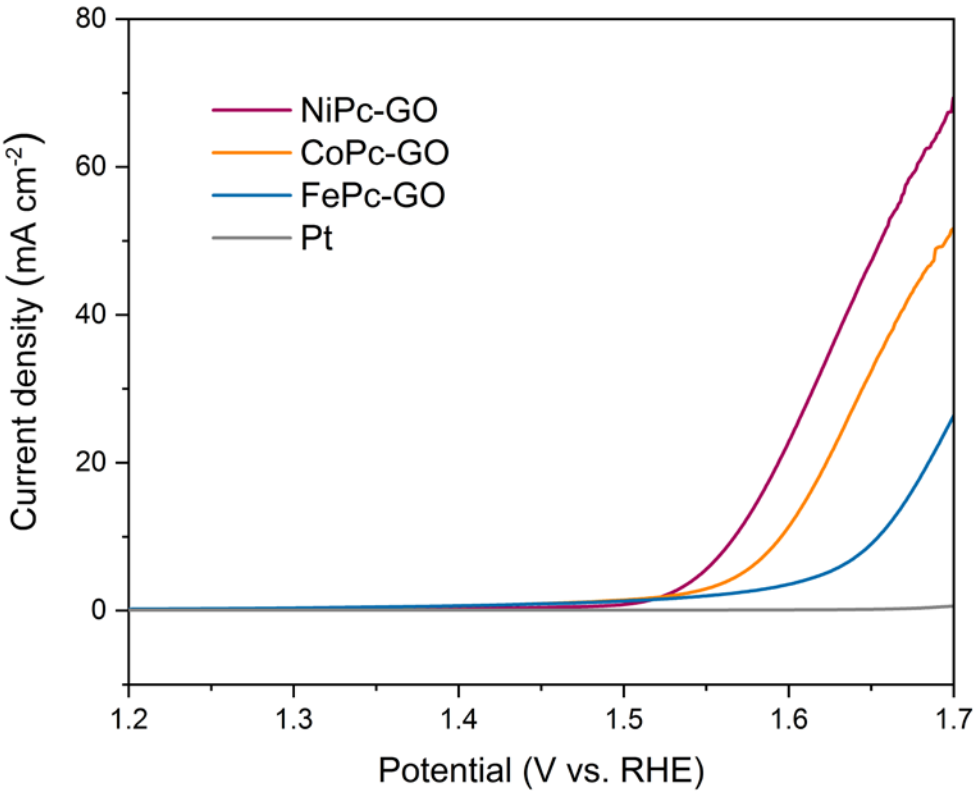

Figure S78. LSV measurements of Pt, NiPc-GO, CoPc-GO and FePc-GO as working electrodes in a three electrode setup using Pt rod as counter and Ag/AgCl as reference electrode in 1 M KOH.

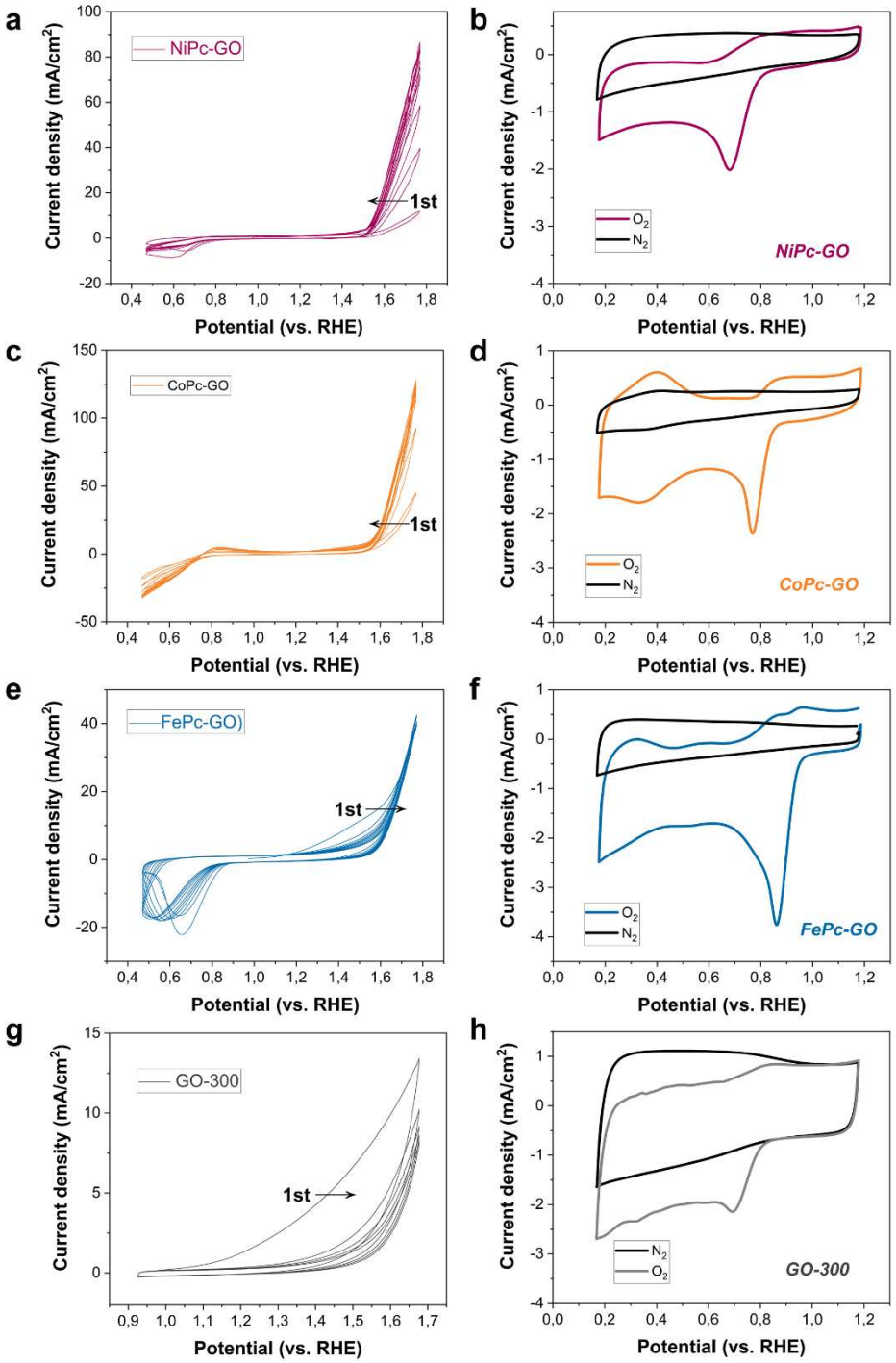

Figure S79. All CV curves of GO-300, NiPc-GO, CoPc-GO and FePc-GO for OER and ORR (in O_2 and N_2).

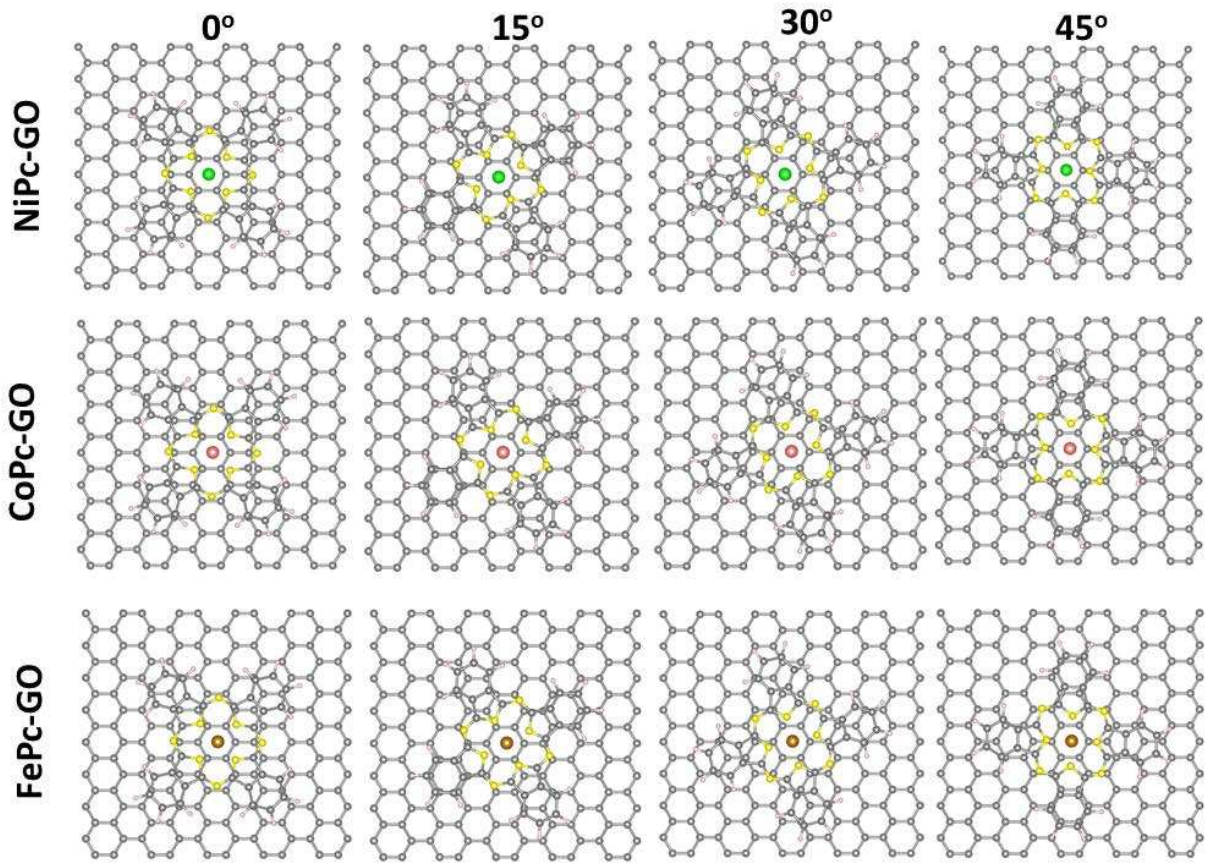

Figure S80. Orientation of the NiPc, CoPc, FePc molecules on graphene with different angles.

Table S8. Relative energies of the configurations with different orientation respect to the most stable one.

	NiPc-GO (eV)	CoPc-GO (eV)	FePc-GO (eV)
0°	0	0	0
15°	0.046	0.166	0.072
30°	0.016	0.138	0.040
45°	0.066	0.187	0.091

Table S9. Comparison of the OER performances with representative non-noble-metal electrocatalysts.

Catalysts	**Loading mass (mg cm^{-2})**	**Overpotential at 10 mA cm $^{-2}$**	**Electrolyte**	**References**
MPc-GO	***0.2 mg cm^{-2}***	***1.55 V for NiPc-GO*** ***1.60 V for CoPc-GO*** ***1.65 V for FePc-GO***	***1.0 M KOH***	*This work*
M–NHGF	0.275 mg cm^{-2}	1.56 V for Ni-NHGF 1.632 V for Co-NHGF 1.718 V for Fe-NHGF	1.0 M KOH	1
S|NiNx−PC/EG	0.15 mg cm^{-2}	1.51 V	1.0 M KOH	2
Co–Nx|P-GC/FEG	0.12 mg cm^{-2}	1.55 V	1.0 M KOH	3
FeCo-Nx-CN	0.1 mg cm^{-2}	1.60 V	1.0 M KOH	4
S,N-Fe/N/C-CNT	0.6 mg cm^{-2}	1.60 V	0.1 M KOH	5
NGM-Co	0.5 mg cm^{-2}	1.75 V	0.1 M KOH	6
Co−C_3N_4/CNT	2.0 mg cm^{-2}	1.61 V	1.0 M KOH	7
N/Co-doped PCP//NRGO	0.714 mg cm^{-2}	1.66 V	0.1 M KOH	8
Ni@NC	0.4 mg cm^{-2}	1.62 V	0.1 M KOH	9
Mn-NG	—	1.567 V	1.0 M KOH	10

Table S10. Comparison of the ORR performances with representative non-noble-metal electrocatalysts.

Catalysts	**Loading mass (mg cm^{-2})**	**$E_{1/2}$ (V *vs.* RHE)**	**Electrolyte**	**References**
FePc-GO	***0.2 mg cm^{-2}***	***0.89 V***	***0.1 M KOH***	***This work***
Ni–NHGF	0.275 mg cm^{-2}	0.86 V	0.1 M KOH	1
Co-SAS/HOPNC	0.6 mg cm^{-2}	0.892 V	0.1 M KOH	11
Co-ISAS/p-CN	_	0.838 V	0.1 M KOH	12
NPMC-1000	0.15 mg cm^{-2}	0.85 V	0.1 M KOH	13
S,N-Fe/N/CCNT	0.6 mg cm^{-2}	0.85 V	0.1 M KOH	5
Co@N-C	_	0.82 V	0.1 M KOH	14
Co−N/CNFs	0.1 mg cm^{-2}	0.82 V	0.1 M KOH	15
Fe_3C@N-CNT	0.25 mg cm^{-2}	0.85 V	0.1 M KOH	16
Fe@Aza-PON	_	0.839 V	0.1 M KOH	17
Fe-N-C	0.4 mg cm^{-2}	0.78 V	0.1 M $HClO_4$	18
SA-Fe-HPC	0.1 mg cm^{-2}	0.89 V	0.1 M KOH	19
SA-Fe/NG	0.24 mg cm^{-2}	0.88 V	0.1 M KOH	20
FeCoNx/C	_	0.86 V	0.1 M $HClO_4$	21

References

(1) Fei, H.; Dong, J.; Feng, Y.; Allen, C. S.; Wan, C.; Volosskiy, B.; Li, M.; Zhao, Z.; Wang, Y.; Sun, H.; An, P.; Chen, W.; Guo, Z.; Lee, C.; Chen, D.; Shakir, I.; Liu, M.; Hu, T.; Li, Y.; Kirkland, A.; Duan, X.; Huang, Y. General Synthesis and Definitive Structural Identification of MN_4C_4 Single-Atom Catalysts with Tunable Electrocatalytic Activities. *Nat. Catal.* **2018**, *1*, 63–72.

(2) Hou, Y.; Qiu, M.; Kim, M. G.; Liu, P.; Nam, G.; Zhang, T.; Zhuang, X.; Yang, B.; Cho, J.; Chen, M.; Yuan, C.; Lei, L.; Feng, X. Atomically Dispersed Nickel-Nitrogen-Sulfur Species Anchored on Porous Carbon Nanosheets for Efficient Water Oxidation. *Nat.Commun.* **2019**, *10*, 1392.

(3) Hou, Y.; Qiu, M.; Zhang, T.; Ma, J.; Liu, S.; Zhuang, X.; Yuan, C.; Feng, X. Efficient Electrochemical and Photoelectrochemical Water Splitting by a 3D Nanostructured Carbon Supported on Flexible Exfoliated Graphene Foil. *Adv. Mater.* **2017**, *29*, 1604480.

(4) Li, S.; Cheng, C.; Zhao, X.; Schmidt, J.; Thomas, A. Active Salt/Silica-Templated 2D Mesoporous FeCo-Nx -Carbon as Bifunctional Oxygen Electrodes for Zinc-Air Batteries. *Angew. Chem. Int. Ed.* **2018**, *57*, 1856–1862.

(5) Chen, P.; Zhou, T.; Xing, L.; Xu, K.; Tong, Y.; Xie, H.; Zhang, L.; Yan, W.; Chu, W.; Wu, C.; Xie, Y. Atomically Dispersed Iron-Nitrogen Species as Electrocatalysts for Bifunctional Oxygen Evolution and Reduction Reactions. *Angew. Chem. Int. Ed.* **2017**, *56*, 610–614.
(6) Tang, C.; Wang, B.; Wang, H.-F.; Zhang, Q. Defect Engineering Toward Atomic Co-Nx-C in Hierarchical Graphene for Rechargeable Flexible Solid Zn-Air Batteries. *Adv. Mater.* **2017**, *29*, 1703185.
(7) Zheng, Y.; Jiao, Y.; Zhu, Y.; Cai, Q.; Vasileff, A.; Li, L. H.; Han, Y.; Chen, Y.; Qiao, S. Z. Molecule-Level g-C_3N_4 Coordinated Transition Metals as a New Class of Electrocatalysts for Oxygen Electrode Reactions. *J. Am. Chem. Soc.* **2017**, *139*, 3336–3339.
(8) Hou, Y.; Wen, Z.; Cui, S.; Ci, S.; Mao, S.; Chen, J. An Advanced Nitrogen-Doped Graphene/Cobalt-Embedded Porous Carbon Polyhedron Hybrid for Efficient Catalysis of Oxygen Reduction and Water Splitting. *Adv. Funct. Mater.* **2015**, *25*, 872–882.
(9) Ren, J.; Antonietti, M.; Fellinger, T.-P. Efficient Water Splitting Using a Simple Ni/N/C Paper Electrocatalyst. *Adv. Energy Mater.* **2015**, *5*, 1401660.
(10) Guan, J.; Duan, Z.; Zhang, F.; Kelly, S. D.; Si, R.; Dupuis, M.; Huang, Q.; Chen, J. Q.; Tang, C.; Li, C. Water Oxidation on a Mononuclear Manganese Heterogeneous Catalyst. *Nat. Catal.* **2018**, *1*, 870–877.
(11) Sun, T.; Zhao, S.; Chen, W.; Zhai, D.; Dong, J.; Wang, Y.; Zhang, S.; Han, A.; Gu, L.; Yu, R.; Wen, X.; Ren, H.; Xu, L.; Chen, C.; Peng, Q.; Wang, D.; Li, Y. Single-Atomic Cobalt Sites Embedded in Hierarchically Ordered Porous Nitrogen-Doped Carbon as a Superior Bifunctional Electrocatalyst. *Proc Natl Acad Sci U S A.* **2018**, *115*, 12692–12697.
(12) Han, A.; Chen, W.; Zhang, S.; Zhang, M.; Han, Y.; Zhang, J.; Ji, S.; Zheng, L.; Wang, Y.; Gu, L.; Chen, C.; Peng, Q.; Wang, D.; Li, Y. A Polymer Encapsulation Strategy to Synthesize Porous Nitrogen-Doped Carbon-Nanosphere-Supported Metal Isolated-Single-Atomic-Site Catalysts. *Adv. Mater.* **2018**, *30*, 1706508.
(13) Zhang, J.; Zhao, Z.; Xia, Z.; Dai, L. A Metal-Free Bifunctional Electrocatalyst for Oxygen Reduction and Oxygen Evolution Reactions. *Nature Nanotech.* **2015**, *10*, 444–452.
(14) Zhang, M.; Dai, Q.; Zheng, H.; Chen, M.; Dai, L. Novel MOF-derived Co@N-C Bifunctional Catalysts for Highly Efficient Zn-Air Batteries and Water Splitting. *Adv. Mater.* **2018**, *30*.
(15) Cheng, Q.; Yang, L.; Zou, L.; Zou, Z.; Chen, C.; Hu, Z.; Yang, H. Single Cobalt Atom and N Codoped Carbon Nanofibers as Highly Durable Electrocatalyst for Oxygen Reduction Reaction. *ACS Catal.* **2017**, *7*, 6864–6871.
(16) Guan, B. Y.; Le Yu; Lou, X. W. A Dual-Metal–Organic-Framework Derived Electrocatalyst for Oxygen Reduction. *Energy Environ. Sci.* **2016**, *9*, 3092–3096.
(17) Kim, S.-J.; Mahmood, J.; Kim, C.; Han, G.-F.; Kim, S.-W.; Jung, S.-M.; Zhu, G.; Yoreo, J. J. de; Kim, G.; Baek, J.-B. Defect-Free Encapsulation of Fe^0 in 2D Fused Organic Networks as a Durable Oxygen Reduction Electrocatalyst. *J. Am. Chem. Soc.* **2018**, *140*, 1737–1742.
(18) Xiao, M.; Zhu, J.; Ma, L.; Jin, Z.; Ge, J.; Deng, X.; Hou, Y.; He, Q.; Li, J.; Jia, Q.; Mukerjee, S.; Yang, R.; Jiang, Z.; Su, D.; Liu, C.; Xing, W. Microporous Framework Induced Synthesis of Single-Atom Dispersed Fe-N-C Acidic ORR Catalyst and Its *in Situ* Reduced Fe-N_4 Active Site Identification Revealed by X-ray Absorption Spectroscopy. *ACS Catal.* **2018**, *8*, 2824–2832.
(19) Zhang, Z.; Sun, J.; Wang, F.; Dai, L. Efficient Oxygen Reduction Reaction (ORR) Catalysts Based on Single Iron Atoms Dispersed on a Hierarchically Structured Porous Carbon Framework. *Angew. Chem. Int. Ed.* **2018**, *57*, 9038–9043.
(20) Yang, L.; Cheng, D.; Xu, H.; Zeng, X.; Wan, X.; Shui, J.; Xiang, Z.; Cao, D. Unveiling the High-Activity Origin of Single-Atom Iron Catalysts for Oxygen Reduction Reaction. *Proc Natl Acad Sci U S A.* **2018**, *115*, 6626–6631.
(21) Xiao, M.; Chen, Y.; Zhu, J.; Zhang, H.; Zhao, X.; Gao, L.; Wang, X.; Zhao, J.; Ge, J.; Jiang, Z.; Chen, S.; Liu, C.; Xing, W. Climbing the Apex of the ORR Volcano Plot *via* Binuclear Site Construction: Electronic and Geometric Engineering. *J. Am. Chem. Soc.* **2019**, *141*, 17763–17770.